Library and Archives Canada

Published Heritage Branch

395 Wellington Street
Ottawa ON K1A 0N4
Canada

Bibliothèque et Archives Canada

Direction du Patrimoine de l'édition

395, rue Wellington
Ottawa ON K1A 0N4
Canada

Your file Votre référence
ISBN: 978-0-494-33345-7
Our file Notre référence
ISBN: 978-0-494-33345-7

NOTICE:
The author has granted a non-exclusive license allowing Library and Archives Canada to reproduce, publish, archive, preserve, conserve, communicate to the public by telecommunication or on the Internet, loan, distribute and sell theses worldwide, for commercial or non-commercial purposes, in microform, paper, electronic and/or any other formats.

The author retains copyright ownership and moral rights in this thesis. Neither the thesis nor substantial extracts from it may be printed or otherwise reproduced without the author's permission.

AVIS:
L'auteur a accordé une licence non exclusive permettant à la Bibliothèque et Archives Canada de reproduire, publier, archiver, sauvegarder, conserver, transmettre au public par télécommunication ou par l'Internet, prêter, distribuer et vendre des thèses partout dans le monde, à des fins commerciales ou autres, sur support microforme, papier, électronique et/ou autres formats.

L'auteur conserve la propriété du droit d'auteur et des droits moraux qui protège cette thèse. Ni la thèse ni des extraits substantiels de celle-ci ne doivent être imprimés ou autrement reproduits sans son autorisation.

In compliance with the Canadian Privacy Act some supporting forms may have been removed from this thesis.

While these forms may be included in the document page count, their removal does not represent any loss of content from the thesis.

Conformément à la loi canadienne sur la protection de la vie privée, quelques formulaires secondaires ont été enlevés de cette thèse.

Bien que ces formulaires aient inclus dans la pagination, il n'y aura aucun contenu manquant.

Canada

Abstract

The use of Quantum Dot Saturable Absorber Mirror (QD-SAM) for ultrashort laser pulses generation via the passive mode-locking mechanism was investigated.

The QD-SAM device is based on InAs/GaAs QD absorbers grown on an AlAs/GaAs Distributed Bragg Reflector. Molecular beam epitaxy was used to grow this monolithic structure.

Different absorption wavelengths from 984 nm to 1080 nm were successfully realized on one wafer growth by not rotating the sample during the growth. The 22% to 31% dip in the reflectivity spectrum attributed to quantum dot absorption, indicates the potential for a large modulation depth and hence generation of ultrashort laser pulses through mode-locking of laser systems.

The QD-SAM was used to mode-lock a grazing incidence slab $Nd:YVO_4$ laser at the operation wavelength of 1064.6 nm. 1.94 W average power was obtained during stable self-starting CW mode-locking with pulses as short as 24 ps, and with a repetition rate of 65 MHz.

Acknowledgements

I would like to thank the many people that have helped me over the years, contributing to my education and my development in the field of science.

I would especially like to thank my supervisor, Dr. Ying Tsui for all the help he has given to me to realize this project and for the valuable pieces of advice he has offered me throughout my research.

Thanks to Dr. Robert Fedosejevs and Dr. Ziyang Zhang for their continuous support and guidance.

Thanks to Dr. John Alcock from the National Research Council for sharing with me his great lasers science passion.

Thanks to Dr. Harry Ruda for offering us the possibility to fabricate our daring design at the Centre for Advanced Nanotechnology from the University of Toronto.

I owe my biggest gratitude to my first Physics teacher, my mother, Florentina Scurtescu, who not only inspired me within my first steps in Physics, but she also provided me the love and support I needed to go further on.

I would like to gratefully acknowledge financial support from MPB Technologies Inc., the Natural Sciences and Engineering Research Council of Canada (NSERC) and the Canadian Institute for Photonic Innovations (CIPI).

Contents

Overview 1

1 Introduction 5

2 Theory Background 9

2.1 Mode-locking theory 9

2.1.1 General description of mode-locking 10

2.1.2 Active / Passive mode-locking 16

2.2 Saturable absorbers 19

2.2.1 Saturation absorption 19

2.2.2 Types of saturable absorber materials 24

2.3 Quantum dot materials 29

2.3.1 Low dimensional materials 30

2.3.2 Molecular Beam Epitaxy growth technique 35

2.3.3 InAs/GaAs material system 41

3 Quantum Dot Saturable Absorber Mirror design, fabrication and characterization 45

3.1 Device design 46

3.1.1 DBR design 49

3.1.2 QD absorber design 51

3.2 Device fabrication 54

3.2.1 Fabrication facility 54
3.2.2 DBR test sample fabrication 60
3.2.3 QD test samples fabrication 64
3.2.4 QD-SAM device fabrication 75
3.3 Device characterization 77
3.3.1 Scanning Electron Microscope analysis 78
3.3.2 QD-SAM low intensity reflectivity 81
3.3.3 QD photoluminescence spectra 86

4 Quantum Dot Saturable Absorber Mirror mode-locked operation **95**

4.1 Experimental setup of the laser system 95
4.2 Experimental results 99

5 Conclusions and Future Work **109**

References **111**

Appendix A **125**

Appendix B **127**

Appendix C **131**

List of Tables

1 Example of laser mediums and their minimum theoretical pulse width (FWHM of Gaussian pulses). 16

2 Examples of QD based saturable absorbers used for pulsed laser operation. 28

3 Averaged effective masses of electrons and holes in Si, GaAs and InAs; $m_0 = 9.1 \times 10^{-31} Kg$ is the mass of a free space electron. 34

4 Growth sequence of AlAs/GaAs multiple layers test sample. . 61

List of Figures

1 Amplitude and intensity of the sum of three sinusoidal waves at frequencies ω, $2\,\omega$ and $3\,\omega$ added out of phase (a), and in-phase (b) [25]. 10

2 Parameters associated with mode-locked pulses in frequency domain and time domain [25]. 15

3 Schematic of the temporal evolution of optical power and losses in an actively mode-locked laser [26]. 17

4 Schematic of the temporal evolution of optical power and losses in a passively mode-locked laser with a saturable absorber [26]. 18

5 Intensity transmittance as a function of incident intensity [31]. 22

6 Density of states (DOS) as a function of confinement configuration: (a) bulk, (b) Quantum Well, (c) Quantum Wire, (d) Quantum Dot [32]. 31

7 Schematic of MBE system. 37

8 Surface processes in MBE. 39

9 Schematic of the three possible growth modes: (a) FvdM, (b) VW, (c) SK. 40

10 Lattice constants for nine III-IV binary compounds [32]. . . . 42

11 Quantum Dot Saturable Absorber Mirror design and bandgap diagram. 48

12 Calculated reflectivity and epitaxial growth time as function of the number of $\lambda/4$ AlAs/GaAs pairs of DBR. 50

13 Calculated reflectivity spectrum of a 25 pair $\lambda/4$ AlAs/GaAs DBR. 51

14 Schematic diagram of the QD absorbers within the resonant micro-cavity. 52

15 Molecular Beam Epitaxy machine from the Centre for Advanced Nanotechnology at the University of Toronto. 56

16 Schematic diagram of the Molecular Beam Epitaxy machine. 57

17 Infrared image of the GaAs substrate in the MBE growth chamber. 58

18 SEM cross-section image (a), and grey-scale profile (b) of the AlAs/GaAs multiple layer test structure. 63

19 Growth sequence of a single InAs/GaAs QD layer structure. . 65

20 PL spectrum at 4K of the test sample including one QD layer. 67

21 Growth sequence of a three stacked InAs/GaAs QD layer structure. 69

22 PL spectrum at 4K of the three QD layer test sample. 70

23 Growth sequence of a three by three stacked InAs/GaAs QD layers. 73

24 PL spectrum at 4K of the three by three QD layer test sample. 74

25 Growth sequence of the QD-SAM device. 76

26 SEM cross-section of the QD-SAM device. 79

27 Photo (a), and schematic diagram (b) of the setup used to measure the QD-SAM low intensity reflectivity. 82

28 (a)-(d) Low-intensity reflectivity spectrum at position A to D on the QD-SAM; (e) Schematic figure of MBE sources and wafer position during QD-SAM growth. 84

29 Photo (a), and schematic diagram (b) of the setup used to measure the room temperature photoluminescence from the QDs. . 88

30 QD-SAM PL correlated with the low-intensity reflectivity spectrum at the same position B, and the PL of a QD test sample; all spectra are measured at room temperature. 90

31 Schematic diagram of the mode-locked laser setup (L1-L5: lenses, M1-M4: dielectric mirrors, PD: photodiode, DBS: diffractive beam splitter, OC: output coupler). 96

32 Analogue oscilloscope trace of the CW mode-locked pulse sequence: (a) $\sim$ 43 ns/div time scale, (b) $\sim$ 4.3 ns/div time scale. 101

33 Measured pulse shape when the $Nd:YVO_4$ laser was operated with the 53% output coupler and the QD saturable absorber. . 102

34 Optical spectrum of the pulses from the $Nd:YVO_4$ laser with the 53% output coupler, when passively mode-locked by using the QD-SAM. 102

35 Measured pulse shape when the $Nd:YVO_4$ laser was operated with the 15% output coupler and the QD saturable absorber. . 103

36 Optical spectrum of the pulses from the $Nd:YVO_4$ laser with the 15% output coupler, when passively mode-locked by using the QD-SAM. 104

37 The laser output transverse mode.. 106

38 Schematic diagram of the laser setup used to calculate the laser operation fluence on the QD-SAM 131

Overview

This report represents the Master of Science research thesis of the student Cristian Scurtescu and was carried out in the Laser and Plasma Laboratory at the University of Alberta, Electrical and Computer Engineering Department (Edmonton, Canada) during a thirty-one-month period.

Some of the results presented in this thesis have been reported in the following articles:

1) C. Scurtescu, Z. Y. Zhang, J. Alcock, R. Fedosejevs, M. Blumin, I. Saveliev, S. Yang, H. E. Ruda, Y. Y. Tsui, "Quantum Dot Saturable Absorber for passive mode-locking of $Nd:YVO_4$ lasers at 1064 nm." Applied Physics B (19 manuscript pages, accepted with minor revisions on February 16, 2007).

2) C. Scurtescu, Z. Y. Zhang, J. Alcock, R. Fedosejevs, M. Blumin, I. Saveliev, S. Yang, H. E. Ruda, Y. Y. Tsui, "Quantum Dot Based Saturable Absorber for Passive Mode-Locking of Solid State Lasers at 1064 nm," Photons Technical Review, vol. 4, 25-27 (2007).

3) C. Scurtescu, Z. Y. Zhang, A. J. Alcock, R. Fedosejevs, M. Blumin, I. Saveliev, S. Yang, H. E. Ruda, and Y.Y. Tsui, "InAs/GaAs Quantum Dot Saturable Absorber Mirror for Passive Mode-Locking of $Nd:YVO_4$ Lasers at 1064 nm", Paper accepted for oral presentation at CLEO 2007, to be presented in May 2007 at Baltimore, USA.

4) Z. Y. Zhang, C. Scurtescu, M. T. Taschuk, Y. Y. Tsui, R. Fedosejevs,

M. Blumin, I. Saveliev, S. Yang, H. E. Ruda, "GaAs based semiconductor quantum dot saturable absorber mirror grown by molecular beam epitaxy", Proc. SPIE 6343, 6343N, 1-11 (2006).

Moreover, the proposal of a second generation design of an improved but similar device has been granted for fabrication by CMC Microsystems.

The report presents the complete research and development cycle of a Quantum Dot Saturable Absorber Mirror (QD-SAM). It starts with the Introduction (Chapter 1), where the current state of development of saturable absorbers and our motivation on developing this device are introduced. The thesis continues with an introduction to theory of mode-locking, saturable absorbers and quantum dot materials (Chapter 2), and then with the design, fabrication and characterization of our QD-SAM (Chapter 3). The results and analysis of the experiments using the QD-SAM for mode-locking operation in a $Nd:YVO_4$ laser system is described in Chapter 4. Finally, the conclusions and future work for the thesis project are presented in Chapter 5.

Parts of this project have been accomplished in collaboration with researchers from our Department (Professor Robert Fedosejevs and Post Doctoral Fellow Ziyang Zhang), from the National Research Council of Canada (Dr. John Alcock), and from the Centre for Advanced Nanotechnology at the University of Toronto (Professor Harry Ruda, Senior Research Scientist Igor Savaliev, Post Doctoral Fellows Marina Blumin and Suxia Yang). The design and fabrication of the QD-SAM have been realized with the guidance from

Dr. Ziyang Zhang. The fabrication of the QD-SAM device as well as the preliminary test samples have been realized in collaboration with the research team from the Centre for Advanced Nanotechnology in Toronto. The testing of the QD-SAM device on the $Nd:YVO_4$ laser system has been done in collaboration with Dr. John Alcock at the National Research Council of Canada in Ottawa.

This page was intentionally left empty.

1 Introduction

The generation of ultra short laser pulses is a rapidly growing area of Photonics. The existence of ultra short laser pulses opened a range of new applications from high bit-rate optical telecommunications to material processing (cutting, micro-machining) and biomedical diagnostics.

Short pulses can be generated from continuous wave (CW) laser light by introducing a saturable absorber into the laser cavity. Saturable absorbers (SA) are commonly used in laser cavities for passive Q-switching and mode-locking.

Many types of saturable absorber material have been used: dyes [1, 2, 3], bulk semiconductor [4, 5] or semiconductor nanostructures (quantum wells-QW [6, 7, 8, 9, 10, 11] or quantum dots-QD [12, 13, 14, 15, 16, 17, 18, 19, 20]). QW and QD saturable absorbers have advantages over the other saturable absorbers because of the abilities to precisely control the non-linearities and to vary the band-gap over a large spectral range.

In recent years, self-assembled quantum dots (QDs) have been investigated both in terms of fundamental studies and potential device application. Good quality semiconductor self-assembled QDs have been fabricated by the use of Molecular Beam Epitaxy (MBE) or Metal Organic Chemical Vapor Deposition (MOCVD) techniques. The efforts have been mainly concentrated in the development of CW QD laser diodes, and good quality operational devices

have been reported [21, 22]. However, the further development of these diode lasers has been hindered by the large dot size distribution (typically larger than 10%) that unavoidably results from the MBE or MOCVD fabrication techniques. However this dot size distribution can be used as an advantage in the generation of ultrashort lasers pulses, where a broad gain/absorption spectrum associated with the dot size distribution is needed to sustain such pulses. One particular application is that of the QD-based saturable absorber used for passive mode-locking of solid state lasers or fiber lasers.

In addition to QD materials, QW materials can also be used as saturable absorbers for ultrashort laser pulses generation. However, when a QW structure is used as a saturable absorber material [6, 7], it is necessary to grow it at lower temperature or perform post growth ion implantation in order to obtain a fast recovery time. Although this would shorten the absorption recovery time, it would also increase the nonsaturable losses. In addition, the use of ion implantation as an additional fabrication step will unavoidably introduce one more process step, and thus may reduce the overall device yield. This is disadvantageous for any potential commercial device. On the other hand, it has been reported that QD materials have ultrafast dynamic response naturally without any additional constraints on fabrication [17, 23]. Recent development of (self-assembled) Quantum Dot Saturable Absorber Mirror (QD-SAM) [12, 13, 14, 16, 17] shows the significant potential of these structures for ultrashort laser pulse generation through passive mode-locking. A QD-SAM is

composed from a QD-based absorption section grown monolithically on top of a distributed Bragg reflector and can be used as an end mirror of a laser cavity for passive mode-locking. The laser light enters into the QD-SAM, is selectively absorbed by the QD absorption section, then reaches the DBR and is reflected back in the laser cavity passing again through the absorption section. The operation bandwidth of a saturable absorber mirror (SAM) is defined by the spectra of the absorption material, the high reflectivity plateau of the distributed Bragg reflector, and by the Fabry Perot cavity formed between the Bragg reflector and exit surface of the device. Due to the intensity dependent saturation of absorption, the QD based absorber will preferentially transmit high intensity pulses in the laser cavity. Thus, it causes the laser to operate in a mode-locked fashion. In(Ga)As/GaAs QD-based saturable absorbers have been used for passive mode-locking in the wavelength range $1.03 - 1.34\mu m$ [12, 13, 14, 16, 17]. Moreover, the use of QD-based saturable absorbers in the communication window of $1.55\mu m$ has been proposed [44]. As the substrate used is GaAs, these saturable absorber devices also benefit from the large index-contrast of lattice-matched Al(Ga)As/GaAs DBRs, which give a broad, high reflectivity plateau with a reduced number of layers.

Currently, no experiments on mode-locking a $Nd : YVO_4$ laser at $\lambda = 1064$ nm by using self-assembled QD saturable absorbers have been reported until this work. Previous work on mode-locking of a $Nd : YVO_4$ laser using QD saturable absorbers was reported at $\lambda = 1342$ nm, using a 0.3% Nd doped

crystal, and a 26 ps pulse width was obtained [14]. In this thesis project we will describe the use of an InAs/GaAs QD saturable absorber to mode-lock a $Nd:YVO_4$ laser at 1064.6 nm.

2 Theory Background

The present research and development of a quantum dot saturable absorber mirror device for passive laser mode-locking depend on the understanding of three main theoretical concepts:

- the process of mode-locking a laser cavity to generate short pulses.
- the operation of saturable absorbers.
- the behavior and fabrication of Quantum Dot materials to be used as saturable absorbers for passive mode-locking.

2.1 Mode-locking theory

Mode-locking is a technique which is used to produce very short duration light pulses, typically from a few tens of picoseconds ($10^{-12}s$) to a few femtoseconds ($10^{-15}s$).

Some lasers may spontaneously produce pulse trains through the relaxation oscillation process, but much shorter pulses can be obtained by forcing all, or a large number, of the longitudinal modes of a laser cavity to oscillate in phase. When this is realized, then the laser is said to be phase-locked or mode-locked. Depending on the available wavelengths and the overall laser setup, pulses as short as 5 fs [8] can be obtained.

The detailed analytical description of mode-locking is presented in many textbooks [24, 25]. The theoretical concepts summarized in this chapter mainly

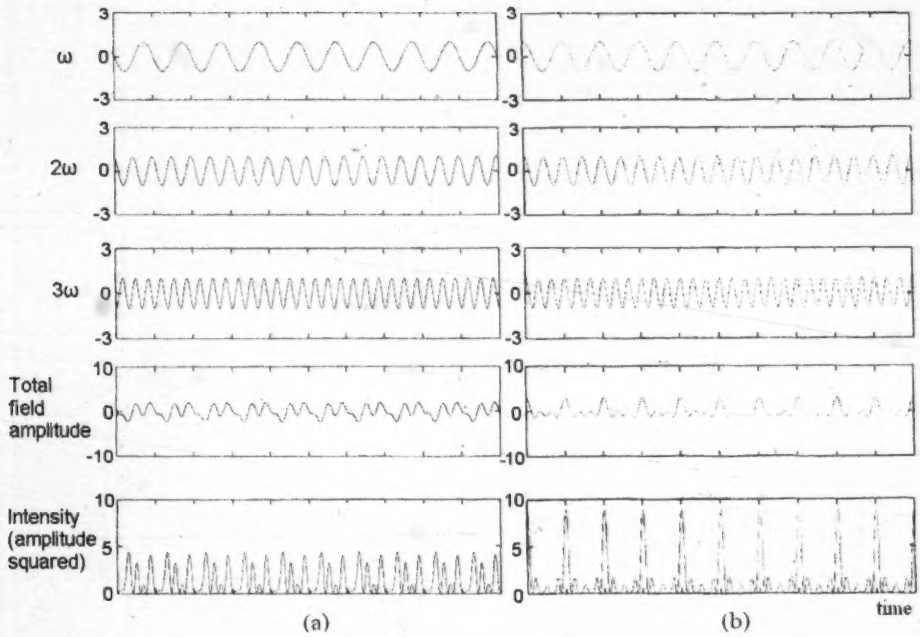

Figure 1: Amplitude and intensity of the sum of three sinusoidal waves at frequencies ω, 2 ω and 3 ω added out of phase (a), and in-phase (b) [25].

follow these two sources.

2.1.1 General description of mode-locking

Mode-locked laser operation regime is achieved by setting in phase a number of distinct longitudinal modes. When these modes with slightly different frequency and random phases are added, they produce a resultant intensity with noise-like random time distribution (see figure 1 a). When the same waves are added in-phase (see figure 1 b), the resultant field amplitude and intensity become repetitive pulses.

A simple explanation of the mode-locked laser operation is as follow. When the laser gain exceeds the losses, the closest longitudinal mode (also called axial or cavity mode) to the gain medium peak will start to oscillate. If the laser is internally modulated with a frequency corresponding to the longitudinal-mode spacing, harmonics will be generated on both sides of the central longitudinal mode exactly at the frequencies of the adjacent longitudinal modes. As the two harmonics and the central longitudinal mode oscillate in phase, the adjacent longitudinal modes will be determined to oscillate in phase with the central longitudinal mode, when the gain of the adjacent modes also exceeds the losses. This process is repeated with each longitudinal mode, and in this way all the modes will oscillate in phase (they are phase-locked).

The longitudinal-mode spacing of a laser cavity is $\Delta\nu = c/2nd$, where c/n is the speed of light in a medium with a refractive index n, and d is laser cavity length (the distance between the laser cavity mirrors, considering a Fabry-Perot cavity). If the laser gain bandwidth is larger than the longitudinal-mode spacing, it is then possible that many longitudinal modes will simultaneously oscillate. In general, each of these modes oscillates independently from the others. In such a system, the electromagnetic field amplitude of the m^{th} mode is:

$$E_m(t) = E_{m0}e^{j(\omega_m t + \phi_m)}, \tag{1}$$

were ω_m is the angular frequency and ϕ_m is the mode phase.

Assuming there are N modes with equal amplitudes ($E_{m0} = E_0$) that

simultaneously oscillates in the laser cavity, then, at a given point inside the cavity, the electromagnetic field can be expressed as the sum of the fields of all the various longitudinal modes, thus the total field can be written as:

$$E(t) = E_0 \sum_{m=0}^{N-1} e^{j(\omega_m t + \phi_m)}. \tag{2}$$

In this case, the angular frequency spacing between two adjacent longitudinal modes, m^{th} and $(m+1)^{th}$, is:

$$\omega_{m+1} - \omega_m = \Delta\omega = 2\pi\Delta\nu = \frac{\pi c}{nd}. \tag{3}$$

As these modes oscillate with random relation between their phase, the total intensity $I(t)$ is given by the square modulus of the electromagnetic field total amplitude $E(t)$:

$$I(t) = \mid E(t) \mid^2 = E_0^2 \sum_{m=0}^{N-1} e^{j(\omega_m t + \phi_m)} e^{-j(\omega_m t + \phi_m)} = N E_0^2, \tag{4}$$

because $\mid e^{jx} \mid = \mid \cos x + j \sin x \mid = \sqrt{\cos^2 x + \sin^2 x} = 1$.

Equation (4) shows that the total intensity $I(t)$ of N modes oscillating simultaneously with random phases is N times the intensity of each individual mode. In the above assumptions that all the N modes are oscillating simultaneously and with random phases, thus what one would detect at the laser output is a constant intensity beam that is not varying in time, known as continuous wave (CW) laser operation.

Let's now analyze the hypothetical case when all the N modes oscillate simultaneously with the same initial phase: $\phi_m = \phi_0$ for every m^{th} mode. In

this case the total field inside the cavity is given by:

$$E(t) = E_0 \sum_{m=0}^{N-1} e^{j(\omega_m t + \phi_0)} = E_0 e^{j\phi_0} \sum_{m=0}^{N-1} e^{j\omega_m t}. \tag{5}$$

The angular frequency of the m^{th} mode , ω_m, can be written as:

$$\omega_m = \omega_{N-1} - m\Delta\omega, \tag{6}$$

where ω_{N-1} is the largest frequency oscillating mode.

Using relation (6), equation (5) can be written as:

$$E(t) = E_0 e^{j\phi_0} \sum_{m=0}^{N-1} e^{j(\omega_{N-1} - m\Delta\omega)t} = E_0 e^{j(\phi_0 + \omega_{N-1}t)} \sum_{m=0}^{N-1} e^{j(-m\Delta\omega)t}. \tag{7}$$

The term $\sum_{m=0}^{N-1} e^{j(-m\Delta\omega)t}$ is a series with a know solution for a finite sum, equation (7) takes the form:

$$E(t) = E_0 e^{j(\phi_0 + \omega_{N-1}t)} \left(\frac{1 - e^{-jN\Delta\omega t}}{1 - e^{-j\Delta\omega t}}\right). \tag{8}$$

The intensity of the laser is then given by:

$$I(t) = \mid E(t) \mid^2 = E_0^2 \mid \frac{1 - e^{-jN\Delta\omega t}}{1 - e^{-j\Delta\omega t}} \mid^2 = E_0^2 \frac{\sin^2(N\Delta\omega t/2)}{\sin^2(\Delta\omega t/2)}. \tag{9}$$

The relation (9) shows that the total intensity varies in time, and the maximum values appear when the denominator tends to become zero: $\Delta\omega/2 = 0, \pi, 2\pi, ..., m\pi$.

Solving for t, the time spacing between two successive maximums t_{m+1} and t_m is:

$$\Delta t = t_{m+1} - t_m = \frac{2(m+1)\pi}{\Delta\omega} - \frac{2m\pi}{\Delta\omega} = \frac{2\pi}{\Delta\omega} = \frac{1}{\Delta\nu} = \frac{2nd}{c}. \tag{10}$$

The relation (10) shows that two successive intensity maximum (called pulses) occur separated in time by $\Delta t = 2nd/c$, which can be seen as the time taken by a pulse to make one full laser cavity round trip; this time corresponds to the longitudinal-mode spacing $\Delta\nu$.

The maximum value of $I(t)$ can be calculated taking the limit of $I(t)$ when $\Delta\omega t/2 \rightarrow 0$:

$$I(t)_{max} = \lim_{\Delta\omega t/2 \rightarrow 0} E_0^2 \frac{\sin^2(N\Delta\omega t/2)}{\sin^2(\Delta\omega t/2)} = \lim_{\Delta\omega t/2 \rightarrow 0} E_0^2 \frac{(N\Delta\omega t/2)^2}{(\Delta\omega t/2)^2} = E_0^2 N^2. \quad (11)$$

Therefore:

$$I(t)_{max} = E_0^2 N^2. \quad (12)$$

Relation (12) shows that the peak pulse intensity for the case when the longitudinal modes are oscillating in phase is N times larger than the intensity when the modes are randomly phased.

The pulse width (FWHM) can be estimated by taking the time difference between the intensity maximum and adjacent minimum, and is given by the relation:

$$\Delta\tau_p = \frac{2\pi}{N\Delta\omega} = \frac{1}{N\Delta\nu} \approx \frac{1}{GainBandwidth}. \quad (13)$$

Relation (13) shows that the mode-locked pulse gets shorter when more longitudinal modes from the gain spectrum oscillate, and when the gain bandwidth is broader.

For a Gaussian pulse the minimum FWHM value is [24]:

$$\Delta\tau_{p_{min}} = 0.441/GainBandwidth_{FWHM}, \quad (14)$$

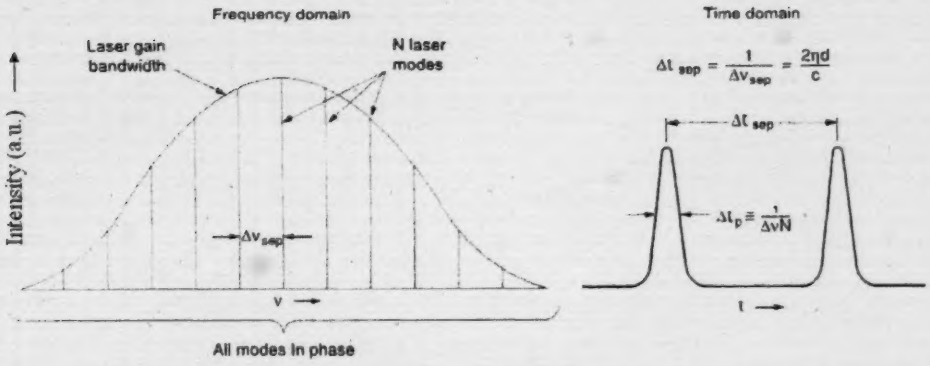

Figure 2: Parameters associated with mode-locked pulses in frequency domain and time domain [25].

which is referred to as band-limited or transform-limited pulse.

In the above assumptions that the N modes are oscillating simultaneously in phase, what one would detect at the laser output is a train of high intensity short pulses with the period of $\Delta t = 2nd/c$ (or repetion rate of $\Delta\nu = 1/\Delta t$), pulse width of $\Delta\tau_p \approx 1/\Delta\nu N$ and peak intensity of $E_0^2 N^2$. This type of laser operation is called continuous wave mode-locking (CW mode-locking). Figure 2 summarizes the parameters associated with the mode-locked operation, and the relation between the frequency domain and time domain.

In table 1, three examples of laser mediums and their minimum theoretical pulse width are shown. The table emphasize the fact that the laser gain bandwidth is an important parameter which determines how short a pulse one could get from a given laser system.

Gain medium	Gain bandwidth (FWHM)	Operation wavelength λ	Minimum pulsewidth $\Delta\tau_{p_{min}}$
HeNe	1.5 GHz (0.002 nm)	632.8 nm	294 ps
$Nd^{3+} : YVO_4$	257 GHz (0.97 nm)	1064.6 nm	1.7 ps
Ti : Sapphire	128 THz (273 nm)	800 nm	3.4 fs

Table 1: Example of laser mediums and their minimum theoretical pulse width (FWHM of Gaussian pulses).

2.1.2 Active / Passive mode-locking

In order to get these high intensity short pulses, one needs to force the laser to be mode-locked. This can be done in two ways, either active or passive. Active mode-locking usually uses an external signal that induces the cavity light modulation. Passive methods use no external signal, and is induced by a cavity element that determines a self-modulation of the cavity light. Each technique has its own advantage and disadvantage, as it will be discussed in this subsection.

Active mode-locking can be achieved with three methods: amplitude modulation (AM), frequency modulation (FM) and synchronous mode-locking. The external electric signal applied on the modulator induces a sinusoidal modulation of the cavity light synchronized to the $2nd/c$ round-trip time of the resonator, which forces the longitudinal modes to phase-lock and so a single pulse will travel in the laser cavity (see figure 3).

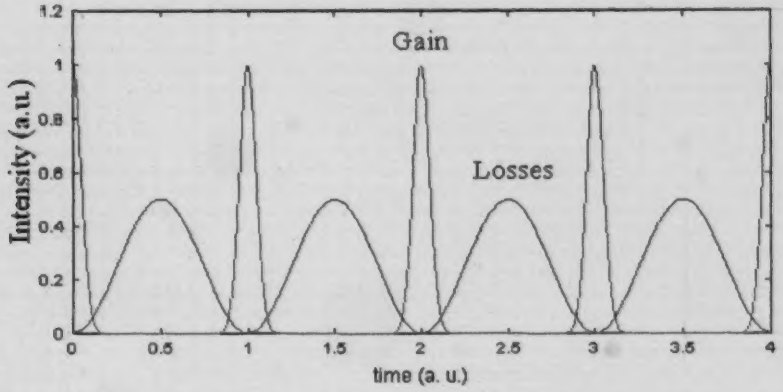

Figure 3: Schematic of the temporal evolution of optical power and losses in an actively mode-locked laser [26].

The AM mode-locking is normally induced by an acousto-optic modulator placed in the laser cavity which behaves as a shutter for the cavity light. The FM mode-locking is usually implemented with an electro-optic modulator, which under external control, induces a sinusoidal frequency shift of the cavity light and forces the cavity modes to be phase-locked. The synchronous mode-locking (also called synchronous pumping) uses no internal modulator, but the directly modulation of the gain medium itself. The laser is turned on and off with the frequency corresponding to the laser cavity round-trip time.

The main advantage of the active mode-locking is the fact that the mode-locked operation starts almost immediately when the external electrical signal is turned on. The disadvantage is the necessity to synchronize the electrical external control signal with the laser cavity-round trip time, and hence complex external electronic devices are needed.

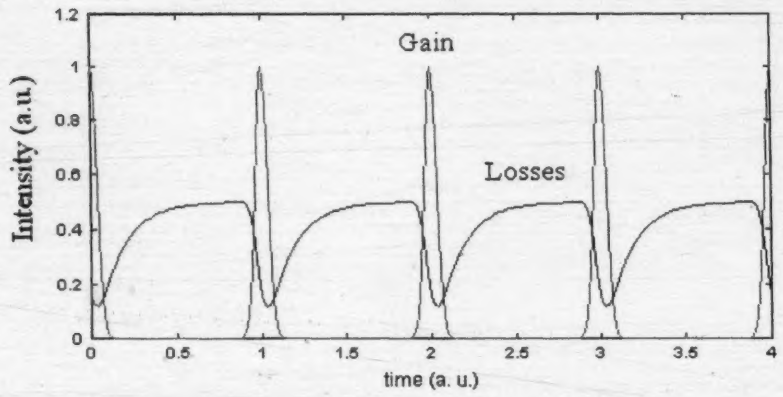

Figure 4: Schematic of the temporal evolution of optical power and losses in a passively mode-locked laser with a saturable absorber [26].

Passive mode-locking is easy to implement and does not require any complex external electronic devices. In this case a cavity element is used to determine the self-modulation of the cavity light. Typically a saturable absorber (SA) is used. At low intensities, a SA presents a high loss to the internal cavity radiation by linear absorption. At high intensity all the energy states are filled and the SA transmit the laser light. After many cavity round-trips, this intensity-dependent absorption process leads to a train of short pulses. Figure 4 shows that the losses from the SA decreases as the front part of the pulse is absorbed. When the losses are smaller then the gain, the pulse is amplified until the gain saturates and become smaller than the losses, and the rear part of the pulse is absorbed. As the tails of the pulse are repeatedly attenuated and the pulse peak is amplified, the overall pulse width becomes shortened.

For a particular laser medium, typically a SA allows the generation of

shorter pulses than the active methods. A SA is driven by the already shortened pulses from the cavity and can modulate the cavity losses faster than an active modulator. However, if a SA does not possess a given set of characteristics (which will be emphasized in the design section) it may cause difficulties in self-starting the mode-locking or Q-switching instabilities can occur.

2.2 Saturable absorbers

A number of sources have presented in detail about the operation principle of saturable absorbers and the process of saturable absorption [31, 25, 24, 34]. This section will mainly follow these sources.

A saturable absorber is a nonlinear optical material that absorbs less light as its intensity increases. It favors the oscillation of high peak intensity laser pulses, and hence pulsed laser operation like Q-switching and mode-locking.

Fast optical saturable absorbers based on semiconductor devices or nonlinear Kerr effect improved the operation of the pulsed lasers and opened a large spectrum of applications with ultrashort pulses (few fs range [8]) and high pulse repetion rates (in the 100 GHz range [50]).

2.2.1 Saturation absorption

At high intensity, photons from the incident light pump electrons into the upper energy level and the ground state becomes depleted so that the system absorbs a smaller fraction of the incident light than it does under low intensity

conditions. This process is called saturable absorption [31, 34].

Generally, a two-level system can be used to model the saturable absorption process when the incident laser pulse is shorter than the decay time of any energy relaxation channel available to the excited electron, and when the transition to any higher-lying state is not resonantly enhanced [31].

There are two types of saturable absorption in two-level systems: the homogeneously broadened system and inhomogeneously broadened system. In a homogeneously broadened system, all atoms or molecules of the system have the same resonant frequency, corresponding to the energy difference of the ground and excited levels. The two-level system absorption spectrum width under these conditions is called the natural line width. In an inhomogeneously broadened system, some internal property of the system causes atoms or molecules of the system to have different resonant frequencies. In a solid material, an inhomogeneous strain distribution (like the one present in the Stranski-Krastanow-mode grown quantum dots) can produce inhomogeneous broadening. The absorption spectrum width of an inhomogeneously broadened line is usually much greater than the natural line width of the system [31].

As this project involves the development of a Stranski-Krastanow grown quantum dot saturable absorber, we will focus our description on the inhomogeneously broadened case.

The intensity dependent absorption coefficient for an inhomogeneously

broadened transition is given by [31]:

$$\alpha(I) = \frac{\alpha_0}{\sqrt{1 + I/I_S^0}}, \tag{15}$$

where α_0 being the linear absorption coefficient, and I_s^0 the saturation intensity of the system. In the steady state, the attenuation of the incident light can be expressed as:

$$\frac{dI}{dz} = -\alpha(I)I = \frac{\alpha_0}{\sqrt{1 + I/I_S^0}}I. \tag{16}$$

Solving for the intensity transmitted through a material of thickness L, the intensity transmittance $T = I(L)/I_0$ is given by relation [31],

$$\frac{\sqrt{1 + TI_0/I_S^0} - 1}{\sqrt{1 + TI_0/I_S^0} + 1} = T_0[\frac{\sqrt{1 + I_0/I_S^0} - 1}{\sqrt{1 + I_0/I_S^0} + 1}]exp[2(\sqrt{1 + \frac{I_0}{I_S^0}} - \sqrt{1 + \frac{TI_0}{I_S^0}})], \tag{17}$$

where I_0 is the incident intensity, I_s^0 is the saturation intensity of the system, and $T_0 = exp(-\alpha_0 L)$ is the linear transmittance. The nonlinear transmittance as a function of I_0/I_s^0 is shown in fig. 5 for various values of T_0. Figure 5 shows that for small incident intensities, smaller than the saturation intensity of the system, the intensity transmittance, T, is approximately equal to the linear transmittance, T_0. For incident intensities larger than the saturation intensity of the system, the transmittance becomes the maximum possible value, 1.

We will now describe the case of a short pulse propagating in a two-level medium at exact resonance. This is an approximate situation of the mode-locked laser operation using a inhomogeneously broadened saturable absorber (in our particular case, quantum dot material). It is assumed that the laser

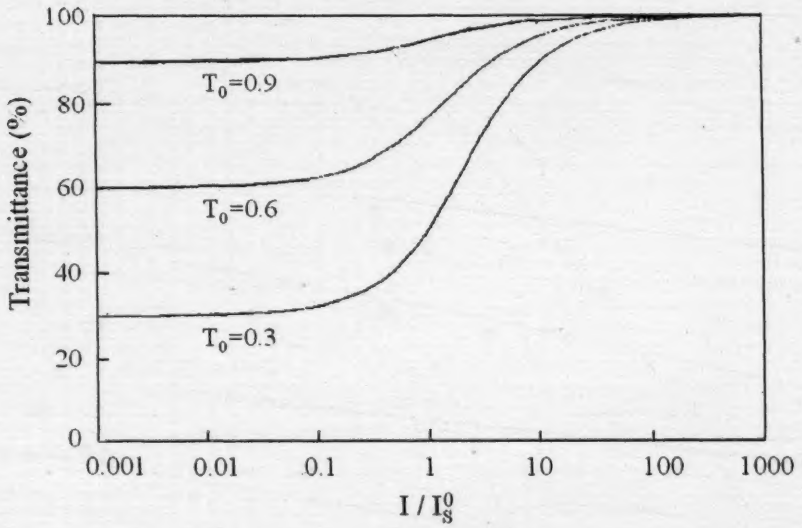

Figure 5: Intensity transmittance as a function of incident intensity [31].

pulse is much shorter than the decay time, τ_1, of the upper state population, i.e. $t_{FWHM} \ll \tau_1$.

The absorption of light in this situation is described by (for plane waves)[31]:

$$\frac{\partial I}{\partial z} + \frac{1}{c}\frac{\partial I}{\partial t} = -\sigma \Delta N(z,t) I(z,t) \tag{18}$$

where $\Delta N = N_g - N_e$ is the population density difference between the two levels, N_g is the population density of the ground level, N_e is the population density of the excited level, and $\sigma = \alpha_0/N$ is the absorption cross-section for the transition, with N being the total density of particles.

The population difference satisfies a simple rate equation :

$$\frac{\partial \Delta N}{\partial t} = -\frac{2\sigma}{\hbar\omega} I(z,t) N(z,t) \tag{19}$$

where $\hbar = h/2\pi$ with h being the Planck's constant. Eqs. (18) and (19)

must be solved simultaneously, with the initial boundary condition $\Delta N(z,t) = \Delta N(0,0) \simeq N_g \simeq N$, with N being the total density of particles. The solution for the intensity at the output of the material is given by the following relation [31]:

$$I(L,t) = \frac{I_0(t - L/c)}{1 + (T_0^{-1} - 1)exp[-\frac{1}{F_s}\int_{-\infty}^{t-L/c} I_0(t')dt']} \tag{20}$$

The quantity $I_0(t - L/c)$ is the intensity at the input to the medium evaluated at a time retarded by the transit time through the medium. $T_0 = exp(-\sigma NL)$ is the linear transmittance, and $F_s = \hbar\omega/2\sigma$ is called the saturation fluence. In the steady state case it was the saturation intensity $I_s = \hbar\omega/2\sigma\tau_1$ that played the key role, but in the pulsed case, with $t_{FWHM} \ll \tau_1$, the accumulated fluence is important. When the accumulated fluence is small compared to F_s, the transmitted intensity goes as $I(L,t) \longrightarrow T_0 I_0(t - L/c)$. However, when the accumulated fluence is large compared to the saturation fluence, $I(L,t) \longrightarrow I_0(t - L/c)$.

The population difference as a function of z and t is given by the following relation[31]:

$$\Delta N(z,t) = \frac{exp(\alpha_0 z)\Delta N_0}{exp[\frac{1}{F_s}\int_{-\infty}^{t-L/c} I_0(t')dt'] + exp(\alpha_0 z) - 1} \tag{21}$$

From this relation we can see that when the accumulated fluence $(\int_{-\infty}^{t-L/c} I_0(t')dt')$ is small compared to F_s, the population density is almost equal to its initial value $\Delta N \simeq N$. For large fluences, $\Delta N(z,t) \longrightarrow 0$ everywhere. The strong beam equalizes the population distribution between the

two levels everywhere so that there is no absorption, and the beam bleaches a transparent path through the material [31].

2.2.2 Types of saturable absorber materials

The current saturable absorber materials are: dyes, bulk semiconductor [4] or semiconductor nanostructures (quantum well QW or quantum dot QD)[6, 17, 16, 9, 10, 11].

The important parameters for a SA are: wavelength absorption range, its absorption recovery time, and its saturation fluence. In the past dyes were commonly used as saturable absorbers. Dyes have short absorption recovery times, but have high toxicity and require handling with care. Saturable absorbers crystals such as Cr:YAG were developed as an more convenient alternative. Unfortunately, Cr:YAG typically operate for only a limited range of wavelengths, recovery times and saturation levels.

On the other hand, semiconductor materials can be used as saturable absorbers over a large spectral range (from visible to mid-infrared). Their absorption recovery time and saturation fluence (typically 1 to 100 μ J/cm^2) can be controlled by changing the growth parameters and device design [35, 10, 6]. As the semiconductor saturable absorbers show saturation absorption at the intensities present in many solid-state lasers, they are ideally suited for the pulsed-operation of these lasers.

Semiconductor saturable absorbers typically are integrated on top of a mir-

ror structure, resulting in a device that reflects more light as the light intensity increases. This class of device is called semiconductor saturable absorber mirrors (SESAMs). SESAM designs have been reported to cover wavelengths from 800 nm to 1600 nm, pulse widths from few picoseconds to nanoseconds, and average power levels from mW to 100W [6, 17, 16, 9, 10]. Semiconductor saturable absorber mirrors basically consist of a high reflectivity mirror (distributed Bragg reflector, DBR) with at least one embedded saturable absorber layer. Currently they are grown by molecular beam epitaxy (MBE) or metal organic chemical vapor deposition (MOCVD) [6, 10]. SESAM design depends strongly on the laser parameters such as the operation wavelength or gain bandwidth. Moreover, the SESAM design has to be optimized for the desired operation regime such as Q-switching or mode-locking by using a slow or fast saturable absorber material.

In the case of quantum well saturable absorber mirrors (QW-SESAM), the absorption region consists of quantum wells, which for $\lambda \leq 1.1\mu m$ are typically made of GaInAs(P)/GaAs layers deposited onto a GaAs/AlAs DBR. For $\lambda \leq 1.3\mu m$ the quantum wells can be made of GaInAs(P), but they must be grown on InP-based DBRs lattice-matched to an InP substrate, which is difficult to fabricate. For a reflectivity of $R \approx 100\%$ a large number of $\lambda/4n$ layers must be used, which creates problems during the device growth [36]. For example in order to obtain high reflectivity DBR one needs to deposit ≥ 40 pairs of $\lambda/4n$ layers on an InP substrate (InGaAsP/InP [4, 27] or AlGaInAs/InP [28]

DBR material system), comparing with $\sim$ 25 pairs of $\lambda/4n$ layers on GaAs substrate (AlAs/GaAs [7, 29, 30] or AlGaAs/GaAs [16] material system).

One approach for the QW absorption material is to combine nitrogen with GaInAs to reduce the band-gap energy of GaInNAs/GaAs QWs on a GaAs/AlAs DBR. Such a heterostructure can be used in a wide operation range from 0.94 μm to 1.55 μm, and represents a significant extension of the GaAs based technology [6]. To shorten the absorption recovery time, τ_{rec}, the crystal must be modified, which can be done by ion implantation [6] or by low temperature growth [10]. The use of ion implantation as a post growth fabrication step not only shorten the τ_{rec} (which is advantageous for mode-locked operation), but also increases the nonsaturable loses (which are not desired) and could also reduce the overall device fabrication yield. Picoseconds laser pulses were reported using QW-SESAM for mode-locking (1.2ps [6], 9 ps [7]) or Q-switching (530ps [9], 180ps [11], 56ps [10]).

The significant progress in the fabrication of semiconductor quantum dot materials by chemical synthesis or epitaxial growth techniques (like MBE or MOCVD) has allowed the rapid development of QD optical devices, including QD based saturable absorbers. A QD SESAM exhibits strong absorption at the peak wavelength, its insertion loss is low when the absorber is bleached, and it has a naturally fast recovery time. QD based SESAMs have a broadband absorption spectrum due to the inhomogeneous broadening associated with the variation of dot size, and hence, have potential for the generation of

much shorter pulses comparing with the QW based absorbers. It is expected that using QD-SESAM, hundreds of fs pulse widths can be obtained directly from a suitable (broad gain spectrum) laser resonator [17, 16].

Several semiconductor quantum dot saturable absorbers for passive mode-locking of solid state lasers have been reported [20, 19, 18, 16, 15, 14, 13, 12]. Table 2 presents the recent results using different QD based absorber materials. The self-assembled In(Ga)As/GaAs QD is the most promising material system to be used in saturable absorbers for ultrashort pulses generation. As the substrate used is GaAs, these absorbers also benefit from the large index-difference lattice-matched Al(Ga)As/GaAs DBRs. This DBR material system gives broad ($\sim 70nm$ at $\lambda = 1064nm$) high reflectivity ($> 99.9\%$) with only 25 pairs of $\lambda/4n$ Al(Ga)As/GaAs layers.

Motivated by these advantages of the QD based saturable absorbers, this thesis will present the development of such a device. The semiconductor quantum dot saturable absorber (containing InAs/GaAs QDs on top of a AlAs/GaAs DBR) also has been used to mode-lock a $Nd:YVO_4$ laser system, and the characterization of the mode-locking will be reported in detail in later chapters.

QD material/ Host material	Fabrication method	Laser medium	Pulse width, λ, Pulsed operation	Reference, Year
PbS/silicate glass	thermal treatment of an oxide molten glass	Cr:forsterite	5 ps, 1.2 μm, mode-locking	[20], 2000
PbSe/phosphate glass		$Ho:YAG$	85 ns, 2.1 μm, Q-switching	[19], 2001
PbS/silicate glass		$Nd:YAG$	70 ps, 1.06 μm, mode-locking	[18], 2002
InGaAs/GaAs	MBE	$Yb:KYW$	4 ps, 1029 nm, mode-locking	[17], 2004
			6.8 ps, 1029 nm, mode-locking	[16], 2005
InAs/GaAs	MOCVD	$Nd:YVO_4$	90 ns, 1342 nm, Q-switching	[15], 2005
			26 ps, 1342 nm, mode-locking	[14], 2005
InGaAs/GaAs	MBE	Yb-doped fiber	2.8 ps, 1042 nm, mode-locking	[13], 2006
InAs/InGaAs		Cr:forsterite	158 fs, 1280 nm, mode-locking	[12], 2006

Table 2: Examples of QD based saturable absorbers used for pulsed laser operation.

2.3 Quantum dot materials

A Quantum Dot (QD) is an island of semiconductor material with dimensions of the order of the De Broglie wavelength of thermalized electrons, which is typically a few nanometers in diameter, and these QDs provide three-dimensional quantum confinement of carriers (electrons and holes).

Under appropriate conditions, strained semiconductors (with lattice misfit $> 2\%$ [39]) grow epitaxially on mismatched substrates in the Stranski-Krastanow growth mode, and QDs are formed after a few monolayers of layer-by-layer growth. Elastic relaxation on the facet edges, renormalization of the surface energy of the facets, and interaction between neighboring islands via the substrate are the driving forces for self-organized growth [38]. Dots with well defined size and size distribution can be obtained with this method even without the use of any patterning or targeted deposition.

Currently, self-organized QDs are grown by Molecular Beam Epitaxy (MBE) or Metal Organic Chemical Vapor Deposition (MOCVD). The use of strain to produce self-organized QDs is now a widely used approach for the group III-V semiconductors. The efforts have been focused on dot size, size distribution and dot density control, for applications on quantum dot lasers, detectors, and recently, saturable absorbers.

The TEM and AFM images of a 2.4ML InAs/GaAs self-organized dot and a layer of such dots are shown in reference [38]. The pyramidal-like dot shape embedded in its host material can be seen in the TEM cross-section image.

The base diameter and height of the QDs strongly depends on the growth parameters and strongly affect the properties of the QD material. The AFM image shows that the dot size is nonuniform, which can be disadvantageous for some applications. The dot size uniformity is also influenced by the growth conditions, and can be improved by using the proper parameters window. These proper windows are specific for a given material system, and also depend on the particular growth equipment used. The detailed parameters-tracking procedure will be presented in the design and fabrication section (Chapter 3) of this thesis.

2.3.1 Low dimensional materials

A detailed description of the low dimensional structures was presented by several authors [32, 40]. This subsection will mainly follow these two sources.

Different degrees of quantum confinement of carriers in semiconductors can be obtained with reduced-dimensional structures like Quantum Wells (2D structure with 1D confinement), Quantum Wires (1D structure structure with 2D confinement) and Quantum Dots (0-D structure with 3D confinement). When a low-dimension structure size is comparable to or smaller than the De Broglie wavelength of thermalized electrons (e.g., $\approx 50nm$ in GaAs), quantum confinement of carriers becomes important. Quantum confinement effects are especially useful for fundamental studies of materials or for photonic device applications.

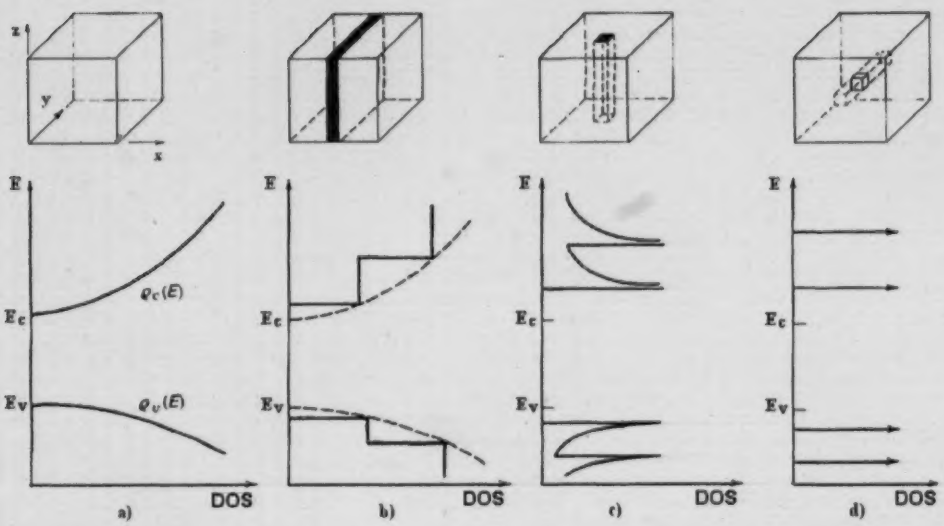

Figure 6: Density of states (DOS) as a function of confinement configuration: (a) bulk, (b) Quantum Well, (c) Quantum Wire, (d) Quantum Dot [32].

A Quantum Well (QW) is a thin layer of semiconductor material ($< 50nm$) with a smaller bandgap than the surrounding material. In the QW shown in the figure 6b the carriers confinement takes place within the well thickness in the x direction , and there is no confinement in the yz plane. In bulk material the density of states (DOS) is zero at the conduction and valence band edges, E_c and E_v. The DOS represents the number of electronic states in a band per unit energy per unit volume of the crystal. In a QW there is a substantial density of states at its lowest allowed conduction-band energy level and at its highest allowed valence-band energy level [32] (see figure 6b).

A Quantum Wire is a thin wire structure of semiconductor surrounded by a larger bandgap material. In a quantum wire the charge carriers are confined

in two directions, x and y. Comparing to a QW, the energy subbands in a quantum wire are narrower [32] (see figure 6c).

A Quantum Dot can be viewed as a 0-dimensional structure where the carriers are narrowly confined in all three directions within a box of volume $d_1 d_2 d_3$. The energy is quantized and given by the energy-momentum relations (Eqn. 22 below, for electrons in the conduction band of a QD, and Eqn. 24 for holes in the valence band of a QD) [32].

The energy-momentum relation for electrons in the conduction band is:

$$E = E_c + E_{q1} + E_{q2} + E_{q3}, \tag{22}$$

where E_c is the bottom of the conduction band, and $E_{q1,q2,q3}$ are given by:

$$E_{q1} = \frac{\hbar^2 (q_1 \pi / d_1)^2}{2m_c}, \qquad E_{q2} = \frac{\hbar^2 (q_2 \pi / d_2)^2}{2m_c}, \qquad E_{q3} = \frac{\hbar^2 (q_3 \pi / d_3)^2}{2m_c}, \tag{23}$$

with $q_1, q_2, q_3 = 1, 2, ..$ representing the quantum number of the energy subbands from the conduction band, $\hbar$ is the reduced Planck constant ($\hbar = h/2\pi$ and h is the Planck constant), m_c is the effective mass of the electron in the conduction band, and $d_{1,2,3}$ are the dot dimensions on x, y and z.

The energy-momentum relation for holes in the valence band is:

$$E = E_v - E_{q1} - E_{q2} - E_{q3}, \tag{24}$$

where E_v is the top of the valence band, and $E_{q1,q2,q3}$ are given by:

$$E_{q1} = \frac{\hbar^2 (q_1 \pi / d_1)^2}{2m_v}, \qquad E_{q2} = \frac{\hbar^2 (q_2 \pi / d_2)^2}{2m_v}, \qquad E_{q3} = \frac{\hbar^2 (q_3 \pi / d_3)^2}{2m_v}, \tag{25}$$

with $q_1, q_2, q_3 = 1, 2, ..$ representing the quantum number of the energy sub-bands from the valence band, and m_v is the effective mass of the hole in the valence band.

Equations 22, 23 and 24, 25 show that the allowed energy levels (for electrons and holes) are discrete and well separated for the QD structure, and so that the density of states is represented by a sequence of delta-like-functions at the allowed energies (see figure 6d) [40, 32]. The QD spectrum looks similar with the spectrum from an atomic system (e.g. hydrogen atom), but in reality a QD contains hundreds or thousands of atoms.

For the case of a bulk semiconductor, the bandgap energy E_{gBULK} is the difference between the lowest allowed conduction band energy level E_c and highest allowed valence band energy level E_v: $E_{gBULK} = E_c - E_v$. For a given bulk semiconductor the bandgap energy is a constant . For the case of a QD structure, the same definition of the bandgap leads to:

$$E_{gQD} = E_c + (E_{q1} + E_{q2} + E_{q3})_{electrons} - E_v - (-E_{q1} - E_{q2} - E_{q3})_{holes} = E_{gBULK} + E_{QDchange}, \tag{26}$$

for quantum numbers $q_1, q_2, q_3 = 1$, and where $E_{QDchange} = (E_{q1} + E_{q2} + E_{q3})_{electrons} + (E_{q1} + E_{q2} + E_{q3})_{holes}$ represents the bandgap energy change determined by the QD structure.

Equation 26 shows that $E_{gQD} > E_{gBULK}$, the bandgap energy of a QD is larger than the bandgap of its bulk material. Moreover, the bandgap energy change, $E_{QDchange}$, depends on the dimensions of the QD. Hence, the bandgap

Material	m_c/m_0	m_v/m_0	Source
Si	0.33	0.5	[32]
GaAs	0.07	0.5	[32]
InAs	0.02	0.4	[33]

Table 3: Averaged effective masses of electrons and holes in Si, GaAs and InAs; $m_0 = 9.1 \times 10^{-31} Kg$ is the mass of a free space electron.

of a QD material can be engineered for a desired value, by choosing proper materials and dot dimensions. For example, we have designed and fabricated InAs quantum dots on GaAs substrates with the ground state transition energy at ~1.17 eV (~1060 nm) even though the bandgap of InAs is 0.365 eV [44]. Detailed description of our QD material design and results are presented in the design and fabrication section (Chapter 3).

Typically, for semiconductor materials, the motion of electrons in the conduction band, and holes in the valence band has different dynamics. This leads to different effective mass for electrons and holes for the same given semiconductor material. Table 3 shows the values of the effective masses for three representative semiconductors [32, 33]. We can see that the effective mass for electrons is usually much smaller than the one for holes. Since the energy separation for electron levels in the conduction band is much larger than the energy separation of hole levels in the valence band (see equations 23, 25), in a first-order analysis it is commonly considered only one energy level for all

holes. The energy separation for electron levels is usually larger than 25 meV (room temperature thermal energy), which allows high-temperature stability and high defect and radiation tolerance of a device. For example, we have obtained ~46 meV energy separation for the first two electron levels [44] of our InAs/GaAs QD material.

The energy levels in QD materials have been calculated by several groups [41, 42, 43], but difficulties were encountered due to the pyramidal like shape of the structures. As the QD facets and the induced strain are dependent on growth conditions, a precise model that is applicable for all cases currently does not exist. In general, for each deposition system or material used it would require the growth of several test samples for parameter tracking before any QD final device is fabricated.

2.3.2 Molecular Beam Epitaxy growth technique

Many sources have presented in detail the Molecular Beam Epitaxy growth technique and the processes that take place during epitaxial growth. This subsection will mainly follow the three sources [47, 40, 48].

Thin layers of semiconductor can be epitaxially grown by techniques like Molecular Beam Epitaxy (MBE), Liquid Phase Epitaxy (LPE), and Vapor Phase Epitaxy (VPE) as well as the variant Metal-Organic Chemical Vapor Deposition (MOCVD). Each technique has its advantages and disadvantages for a given application.

For the fabrication of quantum structures like QWs and QDs, MBE and MOCVD techniques are mainly used. MBE equipment is expensive and low throughput, but this technique can grow high purity structures because its entire epitaxial process takes place in an Ultra-high Vacuum (UHV) chamber. In addition, sharp interfaces in atomic scale can be obtained due to the low growth rate and fast mechanical shutters that can close the effusion cells in a fraction of a second. On the other hand, the MOCVD technique has higher throughput and is less expensive to operate. For some particular applications where high-purity layers and sharp interfaces or doping profiles are critical issues, MOCVD would not be the best option.

The MBE growth process consists of atoms or clusters of atoms produced by heating up a solid source, which then migrate in the UHV environment and impinge on a hot substrate surface. The development of complex molecular beam epitaxy equipment made possible the fabrication of high purity, high uniformity and monolayer interface controlled hetero-structures. A general schematic of a MBE system is shown in Figure 7; its main components are [47]: vacuum system, pumping system and cryopanels, effusion cells, substrate holder/heater, and analysis tools.

Vacuum System. It usually consists of a stainless-steel growth chamber (see figure 7) connected under vacuum to a transfer chamber and a loading chamber (not shown on the MBE system schematic). The transfer chamber is used to degas the wafer prior to its transfer to the growth chamber. The

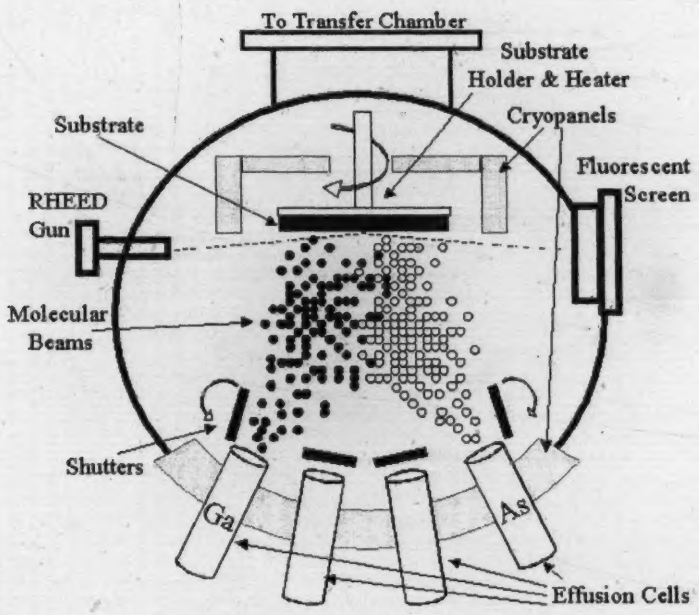

Figure 7: Schematic of MBE system.

loading chamber is used to load the wafers from the air. Each chamber can be independently pumped down and isolated from the other chambers through mechanical gates.

Pumping System. It is used to pump down the vacuum chambers, and to reduce the residual impurities. In practice, the highest vacuum is realized in the growth chamber, where the base pressure is in the 10^{-11} Torr range, with the residual gas being H_2. Usually oil-free pumps are used to avoid contamination. Ion pumps, Ti-sublimation pumps and cryopumps are most typically used.

Cryopanels. The interior of the growth chamber wall is usually surrounded by a liquid nitrogen blanket. The low temperature prevents reevaporation

from the chamber walls, isolates the effusion cells from heating each other, and acts as an additional cryopump of the residual gas.

Effusion Cells. They have a critical role in an MBE system by providing a high flux stability, uniformity and material purity. All the cells (typical four to ten) are pointing to the heated wafer. The flux stability should be better than 1% during a work day, with less than 5% variations from day to day. As the cell temperature determines the molecular beam flux, its temperature control should be $\pm 1^{o}C$ at $1000^{o}C$. The flux from each cell can independently turn on or off in a fraction of a second by a fast shutter placed in front of the cell.

Wafer Holder/Heater. The wafer is mounted on the holder by gluing or clamping with a ring. The holder can be continuously rotated to improve the deposition uniformity across the wafer. The wafer heater is located behind the wafer holder and it is optimized for temperature uniformity, low power consumption and low impurity outgassing.

Analysis Tools. Most MBE systems have a Reflection High Energy Electron Diffraction (RHEED) system and a quadrupole Residual Gas Analyzer (RGA). RHEED uses a high energy ($\sim 20KeV$) electron beam at grazing incidence to the wafer which creates a diffraction pattern on a fluorescent screen. This tool provides information about the geometry and chemistry of the substrate surface. RGA spectra provide information about the residual gasses from the growth chamber, which in turn gives information about possible air leaks and

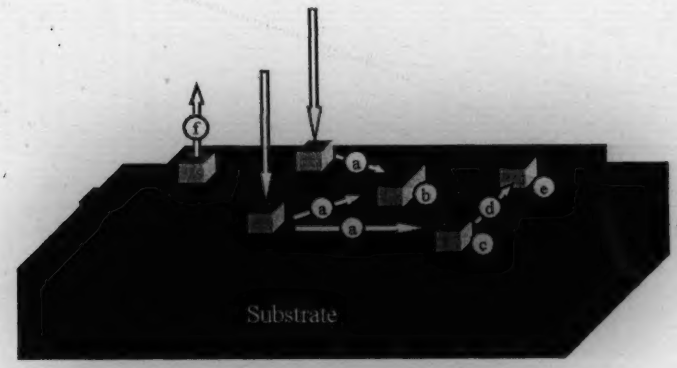

Figure 8: Surface processes in MBE.

system cleanliness.

In the MBE growth process three different phases can be identified [49, 47]: the crystalline phase represented by the substrate where both long and short range order exists, the disordered gas phase of the molecular beam, and an intermediary phase represented by a near surface transition layer. Because the MBE takes place in an UHV environment, the mean free path of the beam molecules is much larger than the distance from the source to the substrate, and no homogeneous reactions can occur in the gas phase.

The near surface transition layer is the phase most relevant to MBE growth technique. Here the atomic or molecular species are physisorbed or chemisorbed on the substrate surface and could go through different processes [47] (see figure 8: (a) diffusion of atoms on a flat surface, (b) formation of two dimensional clusters, (c) incorporation at a surface step, (d) migration along the step, (e) incorporation at a kink, or (f) reevaporation.

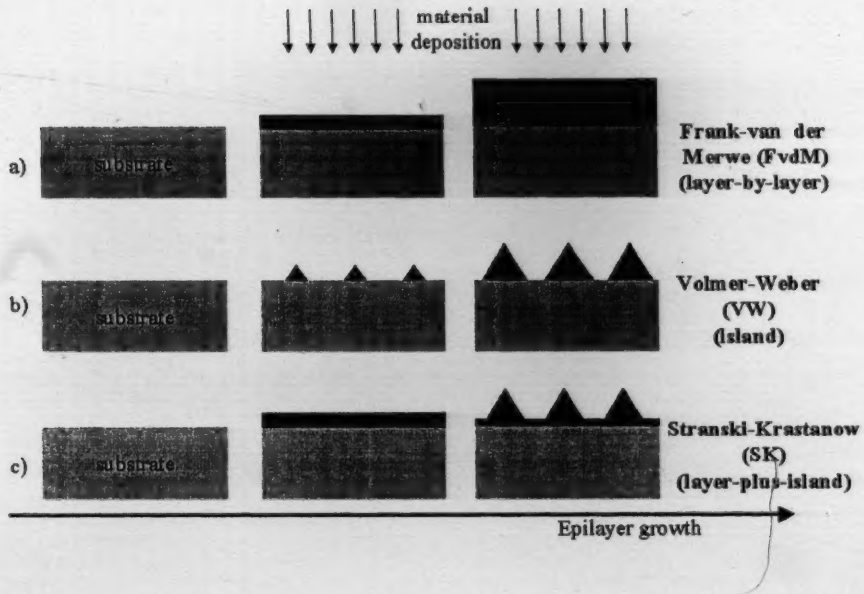

Figure 9: Schematic of the three possible growth modes: (a) FvdM, (b) VW, (c) SK.

When the deposited material is different than the substrate, their lattice constants can be mismatched and strain energy accumulates during the growth. The strain energy depends on the magnitude of the lattice misfit and growth thickness. Figure 9 shows the three possible heteroepitaxy growth modes that can occur as function of lattice mismatch and epitaxial layer thickness: (a) layer-by-layer growth (also called Frank-van der Merwe), (b) island growth (also called Volmer-Weber), and (c) layer-plus-island growth mode (also called Stranski-Krastanow).

The preferred growth mode is determined by the relation between the surface free energies of the substrate $\gamma_{substrate}$, of the interface $\gamma_{interface}$, and of the film γ_{film} [40]. Layer-by-layer growth takes place when: $\gamma_{film} + \gamma_{interface} <$

$\gamma_{substrate}$, the sum of the film and interface free energy is smaller than the substrate free energy. In this mode a complete monolayer is formed before a second layer starts to grow on top of the first. Island mode takes place when: $\gamma_{film} + \gamma_{interface} > \gamma_{substrate}$, the sum of the film and interface free energy is larger than the substrate free energy. In this mode 3-dimensional islands are formed instead of complete layers.

In the layer-plus-island mode (Stranski-Krastanow), the growth starts with the layer-by-layer mode (with $\gamma_{film} + \gamma_{interface} < \gamma_{substrate}$), and when a critical thickness is reached due to the strain induced increase of γ_{film}, the above relation changes and it becomes $\gamma_{film} + \gamma_{interface} > \gamma_{substrate}$ and the growth mode switch to island formation. This is the growth mode for the fabrication of the self-organized quantum dots for the SiGe/Si and In(Ga)As/GaAs materials systems.

The InAs QDs reported in this thesis were fabricated using a MBE equipment employing the Stranski-Krastanow growth mode. Chapter 3 presents our particular designs and fabrication using an "SemiTEq" ATC-EP3 MBE system.

2.3.3 InAs/GaAs material system

InAs/GaAs represents one of the most mature material system used for fabrication of self-assembled QDs through Stranski-Krastanow growth mode.

InAs/GaAs QDs are used in the active area of QD lasers, in detectors and

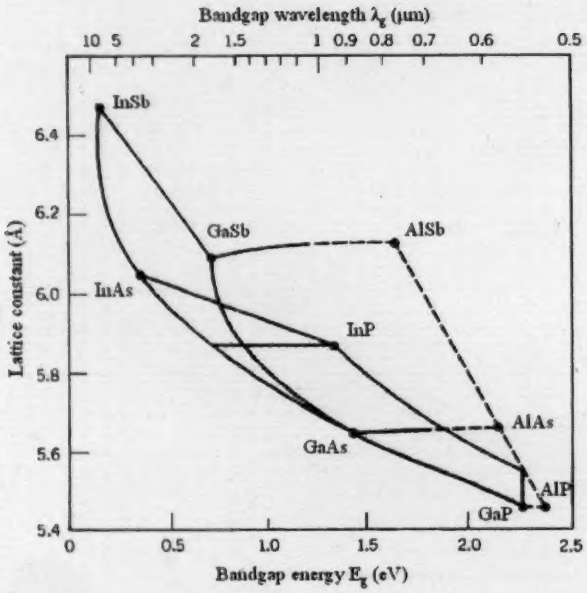

Figure 10: Lattice constants for nine III-IV binary compounds [32].

in saturable absorbers, for a wide range of wavelength from 1 μm to 1.35 μm, and the operation range has been predicted to extend to the 1.55 μm communications window [44] for the case of saturable absorbers.

In self-assembled InAs/GaAs QDs the lattice constant mismatch is 7% between the substrate GaAs (5.65$\AA$) and the InAs deposited material (6.05$\AA$) (see figure 10). This leads the Stranski-Krastanow growth mode to take place, and hence self-organization of InAs quantum dots on the GaAs substrate.

Figure 10 [32] shows the lattice constants for nine III-IV binary compounds. The lines represent the possible ternary compounds. The areas bounded by the lines represent the possible quaternary compounds. Solid and dashed lines represent direct-bandgap and respectively indirect-bandgap compounds .

For the case of saturable absorber mirrors, the InAs/GaAs QD material system makes use of the large refractive index-contrast of the lattice-matched AlAs/GaAs Distributed Bragg Reflector. This DBR material system gives high reflectivity for a broad spectrum with a reduced number of $\lambda/4n$ AlAs/GaAs layers [44, 15, 14]. As can be seen in Figure 10, the lattice constants of AlAs and GaAs are very similar. This makes possible the growth of dislocation-free successive AlAs and GaAs layers with very little limitation on their thickness and number, and prepare the surface for the growth process of QDs.

The operation of QD based devices depend on the QDs size, size uniformity and density. The dot size is controlled by the growth parameters, the most import factors being the quantity of the deposited material and substrate temperature. For the case of InAs QDs on GaAs substrate, the dots start to form after the critical thickness of ~1.5 ML [40] is reached. The optimum size for InAs quantum dots is between ~ 4 nm and ~30 nm.

The dot size uniformity is affected by the slight fluctuations of the parameters that may occur during growth. Dot size distribution of less than 10% is difficult to obtain consistently. A large dot density is required for a better confinement of the carriers in the QDs. The surface dot density can be increased by using low growth temperature and growth interruptions, and increasing the volume dot density by depositing multiple stack of QD layers. If a layer of InAs dots is covered with a thin layer of GaAs and another InAs growth cycle is initiated, the dots in the second layer are formed exactly on top of the dots in

the first layer, resulting in a three-dimensional array of vertically aligned and electronically coupled dots [38]. The use of multiple strain-coupled QD layers not only increases the volume density but also drives a better size uniformity than a single QD layer.

Chapter 3 presents our design and fabrication of several QD based test samples and a QD-SAM device using multiple strain-coupled QD layers made of InAs on GaAs material. For the DBR fabrication, the AlAs/GaAs material system has been used.

3 Quantum Dot Saturable Absorber Mirror design, fabrication and characterization

In this chapter the detailed design process, fabrication and characterization of a QD-SAM device is presented. This chapter reproduces information already presented in our publications [44, 45, 46] with additional details.

The design process and the fabrication process of any device are interdependent. The design requires a detailed knowledge of the fabrication technique (Molecular Beam Epitaxy in our case) that will be used for the physical implementation of the device. In addition, a designer has to know the configuration of the particular MBE machine (like availability of effusion cell materials, substrate size, substrate temperature, epitaxial growth rates and tolerances, etc) that will be used for fabrication. Once the device was designed, parameters like growth temperature of different materials, interruptions, temperature gradients and growth rates will be assigned a range of values. By growing several test samples, the optimum growth parameters are identified through a number of measurements including Scanning Electron Microscopy - SEM, Transmission Electron Microscopy - TEM, Atomic Force Microscopy - AFM, or Photoluminescence - PL. The optimum parameter values are then implemented in the fabrication of the final device. This parameter tracking process is often necessary when new structures and/or materials are implemented.

3.1 Device design

When designing a saturable absorber device, it is necessary that the saturable absorber material has: 1) a saturable absorption at the laser wavelength, 2) a linewidth greater than the gain curve of the laser, 3) a recovery time shorter than the round trip time constant of the laser cavity [24]. When a saturable absorber device is used as a laser cavity mirror, it is required to incorporate a distributed Bragg reflector that has 4) high reflectivity at the laser wavelength, and 5) the spectrum of the high reflectivity plateau broader than the absorption material linewidth. In the design of the QD-SAM we will address each of these criteria.

The design of the present saturable absorber mirror starts from a n-doped (100) GaAs substrate on which a 300 nm thick GaAs buffer layer is deposited first to improve the substrate planarity and to reduce its surface defect density. A distributed Bragg reflector (DBR) of alternative $\lambda/4$ thick layer of materials with high and low index of refraction is grown next. On top of the DBR a resonant micro-cavity in which the QD layers are embedded is deposited (see figure 11). This device is designed to be used as an end mirror of a laser cavity for passive mode-locking at $\lambda = 1064nm$. Hence, all the device components have to be designed for the same central wavelength $\lambda = 1064nm$.

GaAs was chosen as substrate for few reasons: firstly, it is because GaAs is the host material of the QDs and one of the materials that forms the DBR. Its bandgap wavelength $\lambda = 872nm$ (or bandgap energy $E_g = 1.42eV$ at

room temperature) makes it transparent for light with wavelength longer than $872nm$ (or photon energy smaller than $1.42eV$) and thus it is transparent for the laser wavelength at $\lambda = 1064nm$. Secondly, GaAs and AlAs materials have a very small lattice mismatch and a high index-contrast ($\Delta n = 0.54$, where $n_{GaAs} = 3.478$ and $n_{AlAs} = 2.936$ at $\lambda = 1064nm$) that allows to obtain a broad DBR high reflectivity plateau with a reduced number of layers. Thirdly, InAs and GaAs materials have a lattice mismatch of 7%; this leads to the Stranski-Krastanow growth mode to take place when a thin layer of InAs is deposited on the GaAs substrate, and results in a layer of self-assembled InAs quantum dots on top of the GaAs substrate. The substrates used are n-doped (100) GaAs wafers because of their availability. The DBR and QDs layers were not (intentionally) doped.

Our QD-SAM design consists of multiple layers (nine) of InAs/GaAs QD absorbers placed on top of a Distributed Bragg Reflector (25 pairs of $\lambda/4$ AlAs/GaAs layers). A schematic diagram and bandgap diagram of the QD-SAM design is shown in figure 11. For passive mode-locking, this device is used as an end mirror of a laser cavity. The laser light in the QD-SAM is selectively absorbed by the QDs, then reaches the DBR and is reflected back in the laser cavity passing again through the QD absorption section. Due to the intensity dependent saturation of absorption, the QD based absorber will preferentially transmit high intensity pulses in the laser cavity, which causes the laser to operate in a mode-locked regime. The operational wavelength

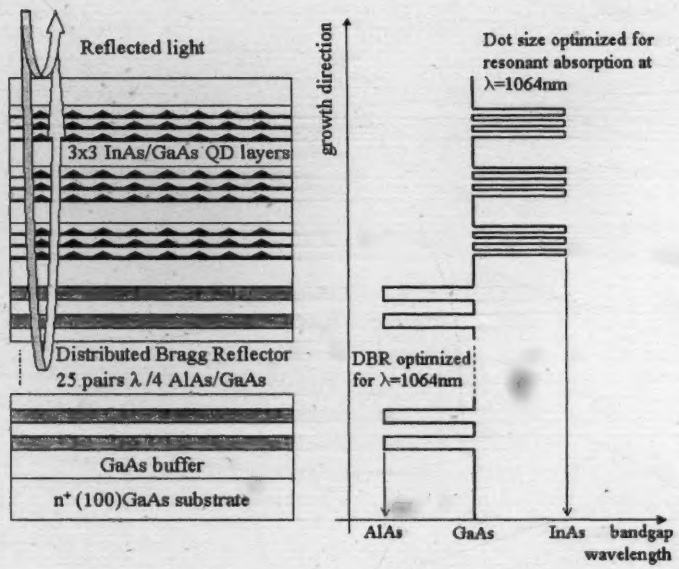

Figure 11: Quantum Dot Saturable Absorber Mirror design and bandgap diagram.

region of the QD-SAM is defined by the spectra of the absorption material, and by the high reflectivity plateau of the DBR. For the design presented here we have optimized both the QD size (which determines the QD absorption wavelength) and the bottom DBR for operation at a centre wavelength of 1064 nm. This was realized by supplying 1.9 monolayers of InAs to form each of the nine layers of QDs, and by depositing 90.6 nm of AlAs and 76.5 nm of GaAs to form each of the 25 pairs of the bottom DBR.

The next two subsections presents the details of the design of the DBR and QD absorber structures.

3.1.1 DBR design

The concept of Distributed Bragg Reflector is presented in numerous books [51, 52, 53]. A DBR is a structure formed from multiple layers of alternating materials with varying refractive indices. In our case the two materials that will form the DBR are AlAs (n=2.936) and GaAs (n=3.478). The thickness of each layer is equal to one quarter of the wavelength of light in the material. As the wavelength of interest is 1064 nm (in air) this means that the thickness of AlAs is 90.6 nm and of GaAs is 76.5 nm. Reflected waves from the interfaces interfere constructively and give rise to a substantial reflected light. Increasing the number of pairs in a DBR increases the mirror reflectivity. Increasing the index-contrast between the materials in the DBR increases both the reflectivity and the bandwidth.

Figure 12 shows the calculated reflectivity values and epitaxial growth time for different number of $\lambda/4$ AlAs/GaAs pairs DBR at the centre wavelength of 1064 nm (see Appendix A for sample calculation). On one hand, it can be observed that the required growth time increases linearly with the number of DBR pairs. On the other hand, the reflectivity increases rapidly to 99% when the number of pairs increases from few pairs to $\sim$ 15 pairs.

Since the fabrication cost is directly proportional to the MBE machine operation time, it is necessary to make a trade off between the reflectivity values of the bottom DBR and the time/cost necessary to produce it. In practice, the reflectivity of a DBR is expected to be smaller than the calculated

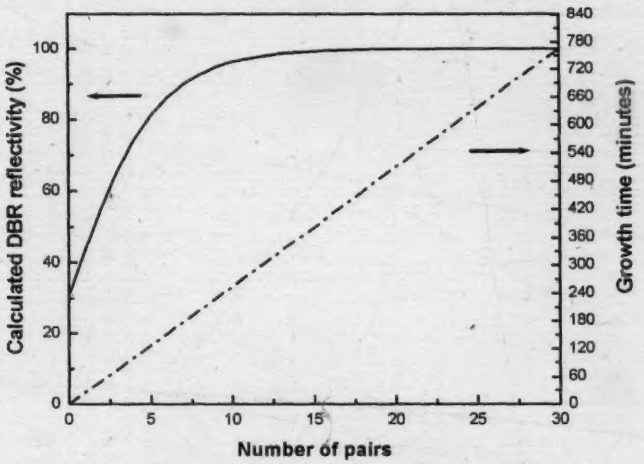

Figure 12: Calculated reflectivity and epitaxial growth time as function of the number of $\lambda/4$ AlAs/GaAs pairs of DBR.

value due to the finite step transition between the layers and due to the errors in the layers thickness.

At the time of our design (fall 2005), four QD and QW saturable absorbers containing high reflectivity DBR were reported. The references [7] and [6] used 25 pairs, respectively 20 pairs of AlAs/GaAs to form the bottom DBR of their QW-SAM. The groups from the references [17] and [16] used 25 pairs of $Al_{0.9}Ga_{0.1}As/GaAs$ to form the DBR of their QD-SAM devices. Based on our calculations and the reported reflectivity values, we decided to use 25 pairs of $\lambda/4$ AlAs/GaAs for the final QD-SAM device fabrication.

Figure 13 shows the calculated reflectivity spectrum [54] (see Appendix B

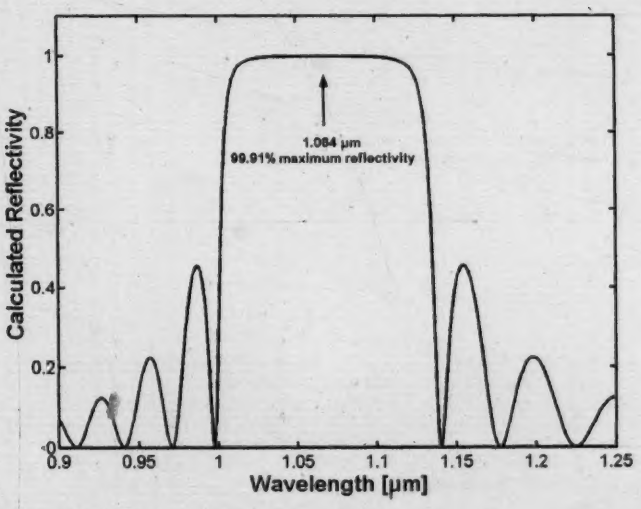

Figure 13: Calculated reflectivity spectrum of a 25 pair $\lambda/4$ AlAs/GaAs DBR.

for calculation method) for the case when 25 pairs of $\lambda/4$ AlAs/GaAs are used to form the DBR. This spectrum presents a high reflectivity plateau of more than 99.9%, $\sim 70nm$ wide, and centered on $\lambda = 1064nm$.

3.1.2 QD absorber design

QDs are the key component of this device, representing the saturable absorption material. It is necessary that the QDs have a bandgap at the laser line, $\lambda = 1064nm$, and its absorption saturated when exposed to the laser light at high intensity. In order to sustain the propagation of ultrashort laser pulses in the laser cavity, it is necessary that the QDs have a broad absorption linewidth. This broad QD absorption spectrum is naturally obtained during MBE fabrication due to the unavoidable dot size distribution. In addition,

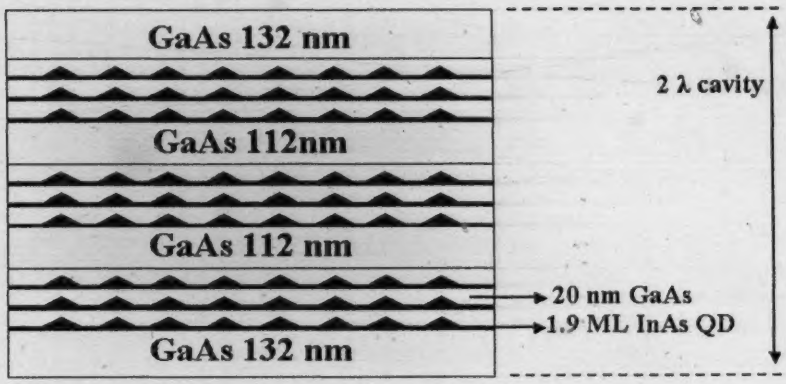

Figure 14: Schematic diagram of the QD absorbers within the resonant micro-cavity.

it was reported [23, 17] that QD materials naturally have ultrafast dynamic response.

As presented in the theory chapter (Chapter 2, section 2.3.1 Low dimensional materials), the bandgap of a QD material can be engineered for a desired value by selecting a proper design and dot size. Figure 14 shows the InAs QD layers embedded in the GaAs micro-cavity. This micro-cavity is located on top of the DBR described earlier. The entire micro-cavity has an optical length of 2λ (or a physical length of 612 nm, where $n_{GaAs} = 3.478$ at $\lambda = 1064nm$) and it is resonant with the incoming laser beam at $\lambda = 1064nm$. Inside the cavity 3 stacks of 3 QD layers are deposited. QDs are grown from 1.9 ML InAs at 480^0C and covered by 20nm of GaAs capping layer. Each stack is separated by 112nm of GaAs, and finally covered by 132 nm GaAs top layer. The center of each group of 3 QD layers is positioned at the intensity maximum of the

standing wave power distribution in the 2λ micro-cavity.

Two kinds of QD materials could have been used to produce dots in the desired bandgap range. These are InAs/GaAs and InGaAs/GaAs material systems. We choose InAs because of the high dot surface density that can be obtained when low growth temperature is used. The group from reference [55] has obtained $2 \cdot 10^{11} cm^{-2}$ InAs/GaAs QDs and only $4.4 \cdot 10^{10} cm^{-2}$ $In_{0.5}Ga_{0.5}As/GaAs$ QDs when conditions similar to ours have been used.

Similar amounts of InAs ($\sim 1.9ML$) and growth temperatures ($\sim 480^0C$) have been used by [40, 55, 56, 57, 58] in order to obtain QDs with bandgap in the range 1000nm-1100nm (at room temperature). QD photoluminescence spectra with bandwidth in the range of 50 nm have been reported.

The growth of the QDs in a given layer is affected by the underlying QD layer, resulting in a vertical alignment (stacking) of the dots. The thickness of the spacing layer determines the amount of strain that is coupled between the QD layers and hence influences the formation threshold and size of the dots. The influence of the spacing layers have been studied in detail and reported in [40] and [57]. For our design we use a 20 nm thick GaAs layer between the QD layers within each group of 3 QD layers. The 112 nm thick GaAs layer that separates each group of QDs is intended to release the strain induced by the bottom dot groups, and in this way the first QD layer from the following group will self-assembled on an unstrained surface.

3.2 Device fabrication

Molecular beam epitaxy was used to grow this monolithic structure. Together with the research team from the Centre for Advanced Nanotechnology at the University of Toronto we have developed the entire fabrication process, starting from single QD layer structures to the 20-hour run to produce the complete structure of the present QD-SAM device. All the growth experiments took four weeks, in the period November-December 2005.

In general, in quantum dot epitaxial growth, for a particular equipment and material system, it typically requires growth of several test samples for parameter tracking before any final device is fabricated. In the next section a brief summary for the MBE system used for fabrication will be presented. Then the fabrication of several QD test samples where we have identified the optimum parameters for stacked QD layers fabrication will be given. Next, the optimum growth parameters for DBR deposition will be discussed. The final QD-SAM device is fabricated based on the information obtained from the test samples.

3.2.1 Fabrication facility

A general overview of the MBE growth technique and MBE machine main components have been presented in Chapter 2, section 2.3.2. Here we discuss only the features of the particular MBE equipment we have used for our device fabrication.

Figure 15 shows the MBE system, model SemiTEq ATC-EP3, at the Centre for Advanced Nanotechnology that was used for the fabrication of the QD-SAM. Figure 16 shows the schematic of the same system.

The MBE machine model SemiTEq ATC-EP3 performs A_3B_5 material epitaxy, and this particular system was dedicated to GaAs based materials. It has eight ports for effusion cells loaded with solid materials as sources. The sources loaded during our experiments were: Arsenic, Gallium, Aluminium, Indium, Silicon, Beryllium. Each effusion cell axis is inclined by 20^0 relative to the substrate surface perpendicular, and the distance from effusion cell to substrate is 220 mm. The maximum temperature that a cell can be heated to is 1250^0C, and their temperature is kept constant with 0.5^0C precision by the use of water cooling and a thermocouple feedback system. Liquid Nitrogen cooled cryopanels surround the cells for thermal isolation. The cells have individual electromechanical shutters that open or close in 0.3 s.

The maximum substrate diameter is 40 mm, and the maximum substrate temperature in the growth position is 800^0C. During our experiments we have used quarters of 2 inch diameter GaAs wafers as substrates. A substrate is mounted on a holder and is transported through all the chambers together with its holder. In the growth position the wafer can be warmed up by a heating system which is water cooled for better thermal stability. Figure 17 shows the infrared image of the quarter GaAs wafer on a holder in the MBE growth chamber. The infrared photo was taken through an empty effusion cell

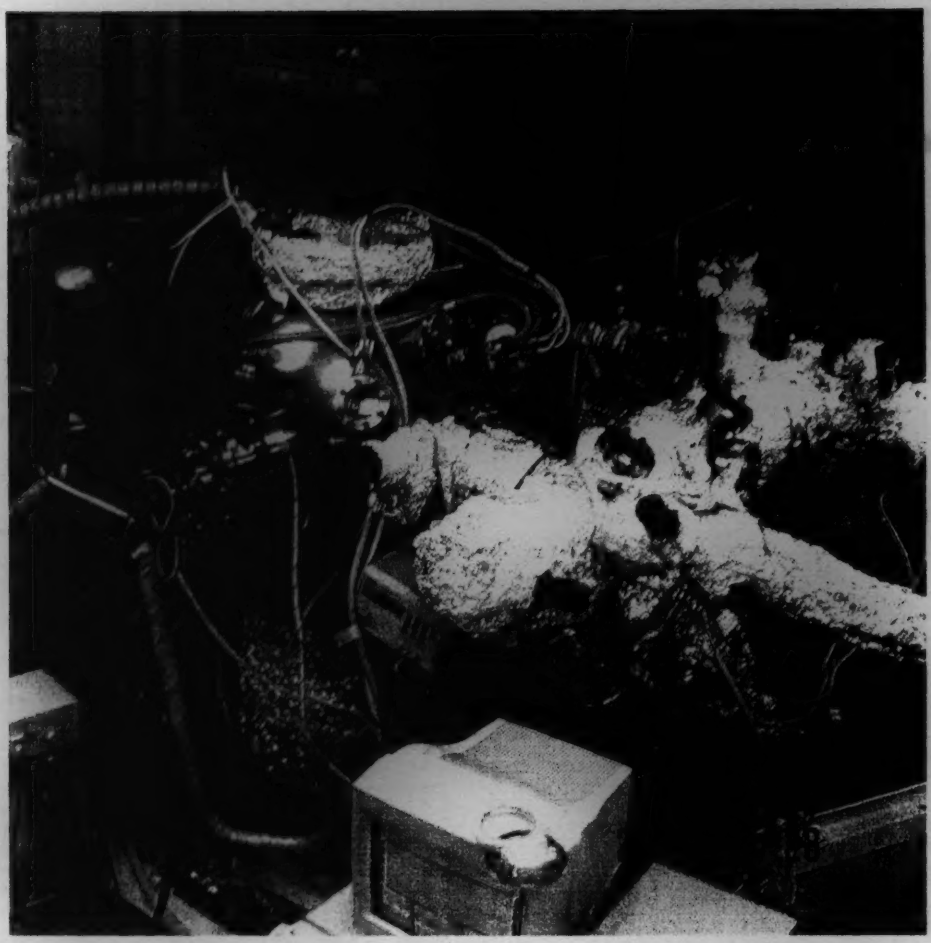

Figure 15: Molecular Beam Epitaxy machine from the Centre for Advanced Nanotechnology at the University of Toronto.

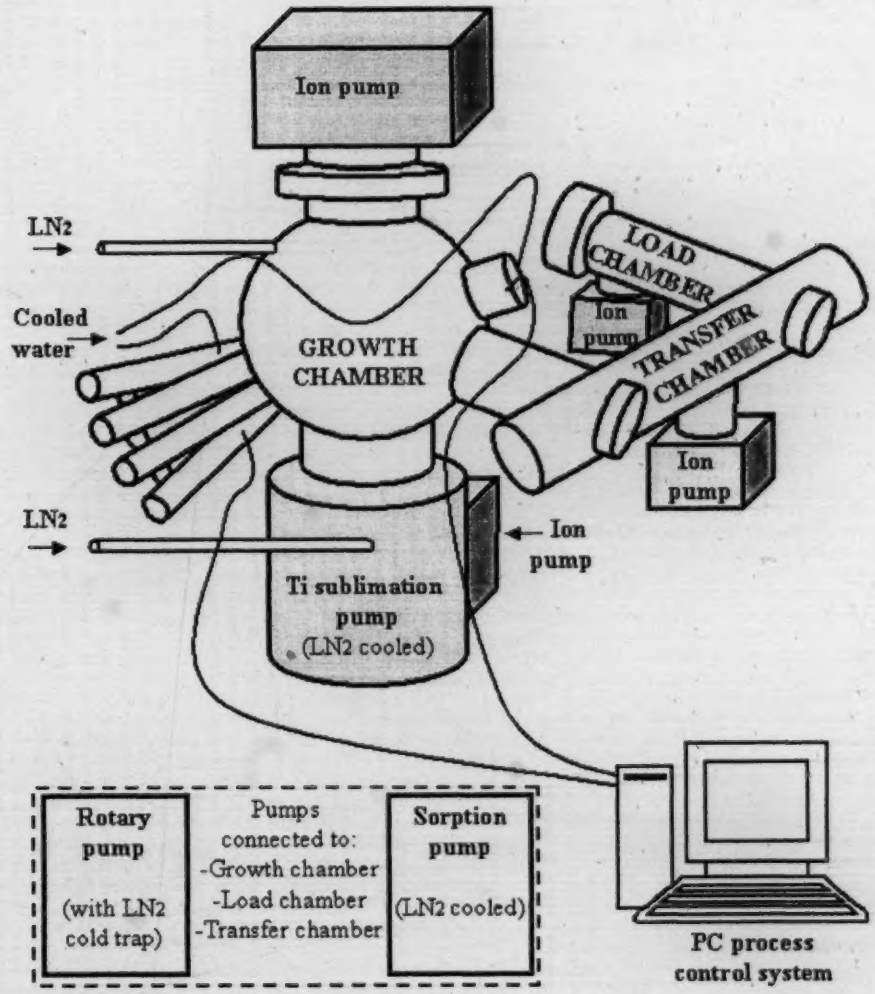

Figure 16: Schematic diagram of the Molecular Beam Epitaxy machine.

Figure 17: Infrared image of the GaAs substrate in the MBE growth chamber.

port and was used to monitor the substrate temperature.

The growth chamber is an UHV stainless steel chamber, ball-shaped and 600 mm in diameter. This is the chamber where the epitaxial growth takes place. It has 3 internal cryopanels (main, upper and effusion cell cryopanels) cooled with liquid nitrogen (LN_2). Two ion vacuum pumps (upper and lower, 400 l/s pumping speed each) and a Titanium sublimation pump (LN_2 cooled) are connected to the growth chamber. In the rare case when the UHV was lost, during maintenance or effusion cell replacement, the growth chamber is pumped down from atmospheric pressure first by the use of a rotary pump (5 l/s with LN_2 cold trap) followed by a sorption pump (LN_2 cooled), and then the ion and sublimation pumps are turned on. The working vacuum level in the growth chamber is $\simeq 1 \cdot 10^{-8}$Pa.

The transfer chamber is used to transport the sample from the load chamber to the growth chamber, to store the reserve samples (maximum 3 pieces) and to outgas the samples and their holders. It has its own ion pump (160 l/s), and can be connected to the rotary and sorption pumps if necessary. The working vacuum level in the transfer chamber is $\simeq 1 \cdot 10^{-8}$Pa.

The load chamber is used to load the samples from the atmosphere. A maximum of 3 samples can be loaded at once. It is physically placed on the ion vacuum pump (400 l/s). When pumped down from atmosphere, a cascade of rotary, sorption and ion pumps is used. The working vacuum level in the load chamber is $\simeq 5 \cdot 10^{-7}$Pa.

In general a rotary pump is used for pumping down from atmospheric pressure to 10^{2}Pa. Then the sorption pump reduce the pressure to 10^{-3}Pa enabling one to start the ion pumps, which reduce the pressure to 10^{-6}Pa. Final stage of UHV (for the growth chamber) is a Ti sublimation pump that reduces the pressure down to 10^{-8}Pa range.

There are a number of diagnostics tools: a quadrupole residual gas analyzer(RGA) to monitor the residual gases from the growth chamber, a reflection high energy electron difractometer (not functional during our experiments), a pyrometer and a digital camera to monitor the substrate temperature.

The entire system is designed for automatic control of epitaxial growth by the use of a computer.

3.2.2 DBR test sample fabrication

We fabricated a test sample in which we used three different growth parameters (substrate temperatures and interruptions) for each of three $\lambda/4$ AlAs/GaAs (90.6 nm/76.5 nm) pairs. The deposition rate and deposition duration was maintained constant for both AlAs and GaAs layers. The As pressure during growth was maintained at $\sim 2.1 \cdot 10^{-6} Pa$. The scope of this test sample was to determine the deposition rate to be used for a precise MBE machine calibration, to determine the deposition repeatability in each AlAs/GaAs pair, and to track the best combination of temperature and interruptions that would give us the sharpest interface between the layers. For the final QD-SAM device it is critical to obtain good repeatability and sharp interfaces of the DBR layers in order to get high reflectivity. Sharp interfaces between the layers can be achieved by allowing time for the added atoms to migrate on the crystal surface before the next layer of different material is deposited, but not too long to avoid contamination by residual oxygen from the chamber.

Table 4 shows the sequence of layers and parameters that were used during the test sample fabrication. First a GaAs buffer (layer no. 0) was deposited. Then the first set of three pairs of AlAs/GaAs was deposited at $580^0 C$ and using 40 s interruption after each AlAs layer (layer no. 1) and 60 s after each GaAs layer (layer no. 2). The second set of three pairs of AlAs/GaAs was deposited at $600^0 C$ and using 20 s interruption after each AlAs layer (layer no. 4) and 30 s after each GaAs layer (layer no. 5). The third set of three

No.	Layer	Designed thickness (nm)	Substrate temperature(^0C)	Stop after (seconds)	No. of pairs
0	GaAs	300	600	60	
1	AlAs	90.6	580	40	3
2	GaAs	76.5	580	60	
3	GaAs	76.5	600	30	
4	AlAs	90.6	600	20	3
5	GaAs	76.5	600	30	
6	GaAs	76.5	600	60	
7	AlAs	90.6	600	40	3
8	GaAs	76.5	600	60	
9	GaAs	66.5	580	end	

Table 4: Growth sequence of AlAs/GaAs multiple layers test sample.

pairs of AlAs/GaAs was deposited at 600^0C and using 40 s interruption after each AlAs layer (layer no. 7) and 60 s after each GaAs layer (layer no. 8).

The SEM cross-section image of the AlAs/GaAs multiple layer DBR test structures is shown in figure 18 (a). A good repeatability in each pair and sharp interfaces between the GaAs and AlAs layers are evident from the picture.

The grey scale profile [59] of the SEM cross-section of the DBR test sample was analyzed (see figure 18 (b)). From this profile plot we see that all of the parameter sets gave abrupt interfaces between the layers, with slightly sharper transitions for Group 1 and 3. This can be explained by the fact that longer interruptions have been used for those groups.

A good repeatability within each group was also obtained, but the measured thickness of all the AlAs and GaAs layers was smaller than the desired values of 90.6 nm and 76.5 nm. For Group 1, the AlAs layer was thinner by $\sim 15\%$ and the GaAs layer by $\sim 3\%$. For Group 2 and 3, the AlAs layer was thinner by $\sim 17\%$ and the GaAs layer by $\sim 8\%$. The difference in the layer thicknesses between the Group 1 on one side, and Groups 2 and 3 on the other side, when same deposition rates and growth durations were used is given by the different substrate temperatures. When the substrate temperature is higher, the evaporation rate of the deposited atoms is also higher leading to smaller growth rate in the presence of the same deposition rate. Because the error in deposition is smaller (hence smaller system adjustment it is necessary) and sharper layer interfaces are obtained for the Group 1, we have chosen to

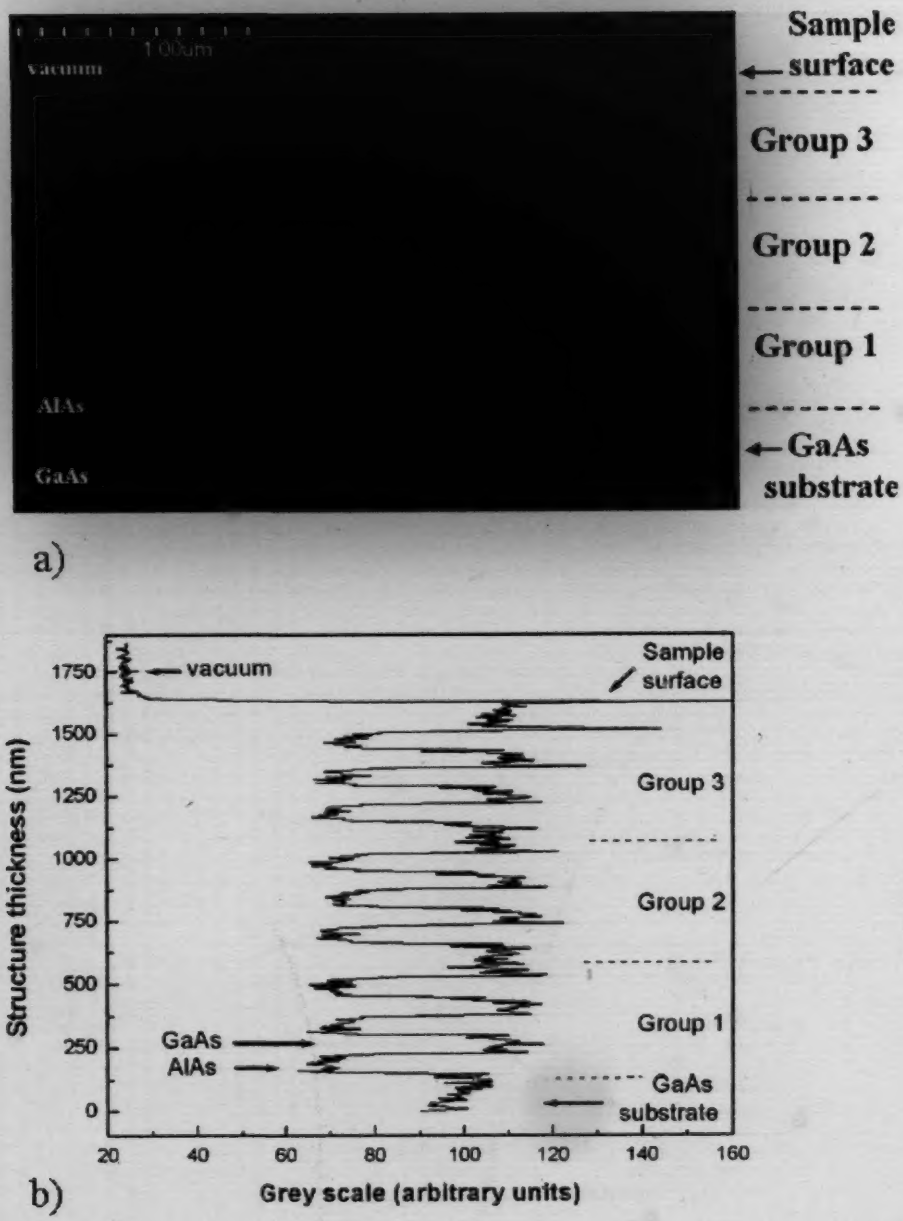

Figure 18: SEM cross-section image (a), and grey-scale profile (b) of the AlAs/GaAs multiple layer test structure.

use this parameter set for the future growths.

Therefore, the group 1 parameter set (580^0C growth temperature combined with 60 s growth interruption after each GaAs layer and 40 s after each AlAs layer growth) are chosen for the growth of the final device, with a deposition rate adjustment of +15% and +3% for AlAs and GaAs respectively.

3.2.3 QD test samples fabrication

Three QD test samples have been grown before the fabrication of the QD-SAM device. We started with the growth of a single QD layer structure, then a three stacked QD layer structure was fabricated. Lastly, a structure containing three groups of three QD layers has been grown, this being similar with the final QD-SAM device absorption section.

Photoluminescence (PL) measurements were performed to analyze the bandgap of the QD materials. For the measurements of test samples at low temperature (4K) we have used a closed-cycle He cryostat under the excitation of a 754 nm laser with variable average power from 5 mW to 75 mW. The PL spectrum from the quantum dot was recorded using an InGaAs photodetector, with the exception of the single QD sample, where a Si detector was available.

The scope of the first QD test structure was to determine the formation of InAs QDs on GaAs substrate and their bandgap, when we use our initial set of parameters. Figure 19 shows the sequence of layers and the parameters that have been used for the fabrication of the single QD layer structure. Arsenic

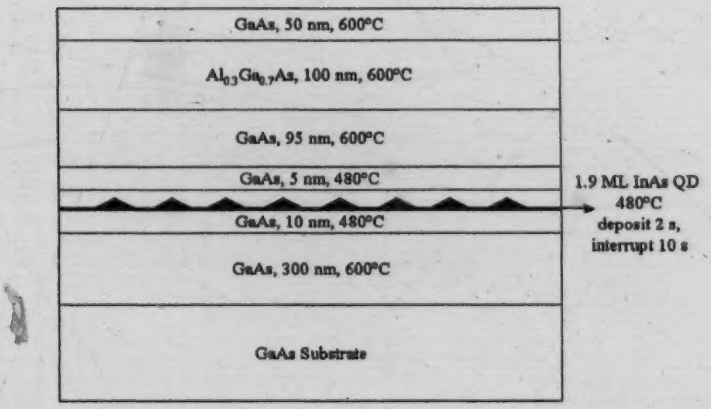

Figure 19: Growth sequence of a single InAs/GaAs QD layer structure.

pressure during growth was maintained at $\sim 3 \cdot 10^{-6} Pa$. The fabrication commenced with the growth of a 300nm GaAs buffer layer at $600^0 C$ on the GaAs substrate. Before the deposition of InAs QD material to start, the temperature of the substrate was rapidly reduced to $480^0 C$ followed by the deposition of a 10nm GaAs layer. In general, GaAs layers (tens of nm thick or more) are epitaxially grown on GaAs substrates at temperatures of $560 - 600^0 C$ in order to produce materials that are dislocation free. In our case we have decided to deposit a very thin GaAs layer (10nm) at the relatively low temperature of $480^0 C$. Because the GaAs layer is very thin, it is not expected to induce dislocations.

Next, 1.9 ML of InAs were deposited at $480^0 C$. A total deposition time of 48 s at the rate of 0.04 ML/s was used to deposit the InAs material. The

growth was performed in 24 periods, each of 2 s InAs deposition followed by 10 s interruption. The growth interruptions were used to allow time for In atoms to migrate on the surface and recombine with the As atoms, and to form the InAs self-assembled dot layer. After the InAs deposition is complete, a 5 nm of GaAs at 480^0C is grown immediately in order to stop the InAs material to perform further surface migration and self-assembling. Now, the QD layer is formed and sealed, and a protective layer of 95 nm GaAs is grown at 600^0C. Then a 100nm of $Al_{0.3}Ga_{0.7}As$ and a 50nm of GaAs both grown at 600^0C complete the test structure. The Al containing layer was used to enhance the carrier confinement in the QD layer when the PL measurements will be performed. The bandgap wavelength of the $Al_{0.3}Ga_{0.7}As$ material is around 645 nm (or bandgap energy of $\sim 1.92eV$) and hence it creates a deeper potential depression for the QD layer. The top 50nm GaAs layer is used to protect the Al containing layer from the atmospheric oxygen that could negatively affects its optical properties.

Figure 20 shows the PL spectrum at 4K and excitation power of 5mW, of the single QD test sample. For this particular sample a Si detector has been used. The use of Si detector in the $1\mu m$ region is disadvantageous due to its reduced quantum efficiency in that range, but in our case that was the only detector available at the time. In this spectrum several emissions can be observed. The high intensity peak from the wavelength of $\sim 820nm$ comes from the GaAs bandgap while the one from 920nm can be attributed most

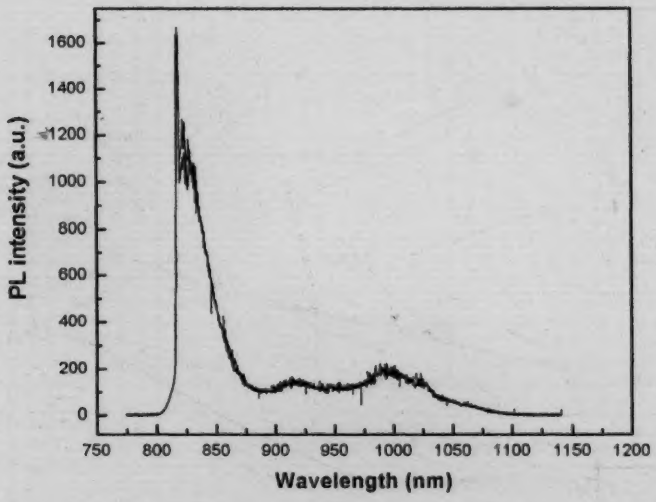

Figure 20: PL spectrum at 4K of the test sample including one QD layer.

probably to deep bandgap levels (crystal defects or residual dopants) from the same GaAs host material. Similar PL peaks at about 820nm and 920nm were detected from a bare GaAs wafer at 4K. The GaAs bandgap wavelength is 872nm at room temperature (RT) and it reduces with temperature down to approximatively 820nm at 4K. The peak from 990nm is attributed to QD ground state emission. For the case of QD material it is expected to see similar reduction in bandgap wavelength of around 55 nm from RT to 4K. This means that our QDs emit at $\sim$ 1045nm at RT, which is $\sim$ 20nm shorter than the desired wavelength of 1064nm. The weak QD-PL signal can be explained by the reduced number of dots and/or reduced radiative recombination in the existing dots.

From this first QD test sample we have concluded that the QD layer was present. For the next QD test sample we decided to increase the QD size by depositing more InAs material and hence increase the QD wavelength. We have also decided to set up and use the InGaAs photodetector from now on due to its better sensitivity at the $1\mu m$ range compared with the Si detector.

In the second QD test sample we wanted to increase the dot volume density by depositing multiple stack of QD layers. Three layers of QDs were stacked together in this test structure. If a layer of InAs dots is covered with a thin layer of GaAs and another InAs growth cycle is initiated, the dots in the second layer are formed exactly on top of the dots in the first layer, resulting in a three-dimensional array of vertically aligned and electronically coupled dots. By using multiple strain coupled QD layers we expect not only to increase the QD volume density but also to get better size uniformity than a single QD layer.

Figure 21 shows the sequence of layers and parameters that have been used during the fabrication of the three stacked QD layer test sample. Similar with the first test sample, the fabrication of the second QD test sample started with the deposition of a GaAs buffer layer, at 580^0C this time. The buffer layer growth temperature was decreased from 600^0C to 580^0C to reduce the time necessary for the substrate to reach 480C needed for InAs dot material deposition. Then, a 10nm GaAs layer was deposited at 480^0C. 2.1ML of InAs material was then deposited to form the first QD layer, at the temp of

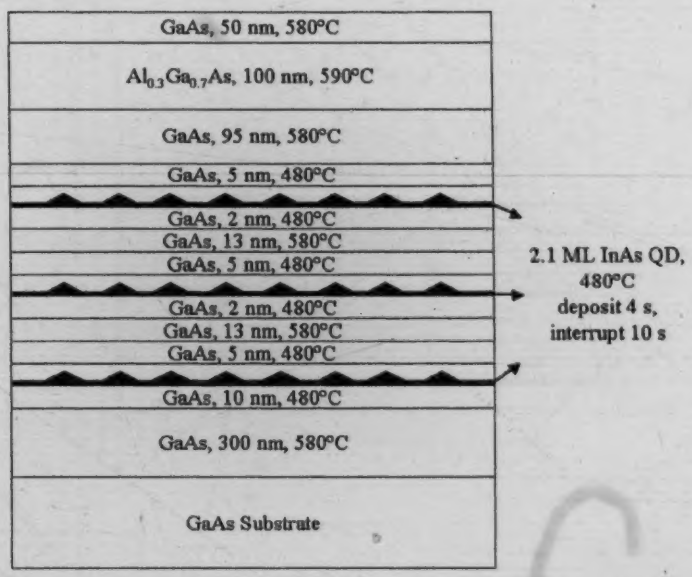
GaAs, 50 nm, 580°C
$Al_{0.3}Ga_{0.7}As$, 100 nm, 590°C
GaAs, 95 nm, 580°C
GaAs, 5 nm, 480°C
GaAs, 2 nm, 480°C
GaAs, 13 nm, 580°C
GaAs, 5 nm, 480°C
GaAs, 2 nm, 480°C
GaAs, 13 nm, 580°C
GaAs, 5 nm, 480°C
GaAs, 10 nm, 480°C
GaAs, 300 nm, 580°C
GaAs Substrate
2.1 ML InAs QD, 480°C deposit 4 s, interrupt 10 s

Figure 21: Growth sequence of a three stacked InAs/GaAs QD layer structure.

480^0C. For this we used a total deposition time of 52 s at the rate of about 0.04 ML/s. This time we have used 13 periods of 4 s InAs deposition and 10 s interruption. Immediately after the InAs deposition sequence ended, a 5 nm GaAs layer at 480^0C was deposited. Next, a 13nm GaAs layer was grown at 580^0C in order to get a dislocation free layer. After that, the temp of the substrate was reduced to 480^0C and a 2nm of GaAs was deposited. The second layer of InAs material was then grown in the same conditions with the first InAs layer. The total spacing layer between the QD layers is 20nm of GaAs. The structure fabrication continued using the same parameters for all the three QD layers and their GaAs spacers. The final three layers, GaAs (95nm at 580^0C), $Al_{0.3}Ga_{0.7}As$ (100nm thick at 590^0C) and GaAs (50nm at

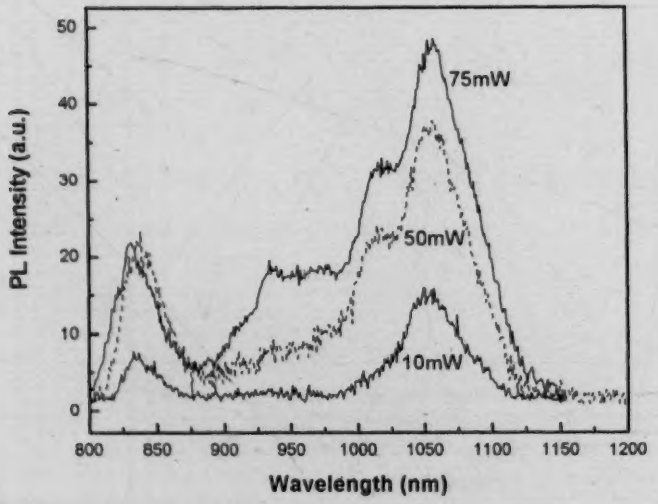

Figure 22: PL spectrum at 4K of the three QD layer test sample.

580^0C), have been deposited for the same reasons presented in test sample one, and the growth temperatures was slightly reduced in the actual sample to reduce the thermal effects that may affect the QD layers by inter-diffusion with the host material. This unintentional interdiffusion determined by the high substrate temperature is practically equivalent with a thermal annealing which may determine the reduction of dots dimension and hence a blue shift of their wavelength bandgap.

Figure 22 shows the PL spectrum at 4K of the three QD layer test sample. InGaAs photodetector was used for these measurements. Optical powers of 10mW, 50 mW and 75 mW were used for the excitation of this test structure. In figure 22, only two peaks were observed at 10mW excitation power. The

emission at around 1055 nm is from the ground state of the QD and the other at around 830 nm is from the emission of GaAs host material. As the excitation power is increased from 10 mW to 75 mW, third, fourth and fifth peaks appear around 1020nm, 970nm and 930nm respectively. The results indicate a state-filling effect with increasing excitation power with the new peaks originating from the first, second and third excited states of the QDs. This state filling behavior is a signature of the QD materials that have discrete allowed energy levels. For this sample, the PL intensity of ground state of QD is about 2 times stronger than that of GaAs host material. As the ground state emission of the QDs is around 1055nm at 4K, it is expected that the central QD bandgap at RT to be about 1110nm. This is approximatively 45nm longer wavelength than the desired 1064nm wavelength. The QD bandgap value from this second test sample made us believe that the increase of the InAs material quantity in each QD layer from 1.9ML in the first sample to 2.1ML in the present sample wasn't necessary. Most probably the detection of QD ground state emission of the first test sample shown in the figure 19 was affected by the use of the Si detector. We have decided to return to the initial 1.9ML of InAs to be supplied for each QD layer. We also concluded that the three QD stacked layers gave strong PL signal at 4K, stronger than the substrate signal.

Now that we have determined the parameters needed to grow the three stacked QD layers, we want to assemble three structures containing three stacked QD layers. This final test sample it is similar with the structure

that will form the QD-SAM device absorption section. Figure 23 shows the sequence of layers and parameters that have been used during the three groups of three stacked layer QD test sample fabrication. For this sample we will stop using the top Al containing layer, and we expect that this will cause a reduction in the carrier confinement within the dots and so a reduction in the QD PL intensity. On the other hand, by using nine layers of QDs the PL emission from the dots will be enhanced. By not using the Al containing top layer we have reduced the total time the structure is exposed to high temperature (higher than the dot growth temperature of 480^0C), and hence reduced the thermal annealing of the dots. The fabrication of the third QD test sample repeats the three stacked QD layer structure three times. Each QD layer was formed by supplying 1.9ML of InAs in 12 periods of 4s deposition and 10 s interruption. 20nm GaAs spacing layer was used to separate the QD layers within each group of three dot layers. Separation layers of 115 nm of GaAs at 580^0C was used between each group of three QD layers. Finally the structure is covered by 127 nm of GaAs at 580^0C.

Figure 24 shows the PL spectrum at 4K of the nine (three by three) QD layer test sample. InGaAs photodetector has been used for these measurements. Powers of 5mW, 50 mW and 75mW were used for the excitation of this test structure. In figure 22 only one obvious peak from the InAs QD was observed, with intensity much stronger than the GaAs host material. This result suggests that due to the increase of QD density and the strong strain

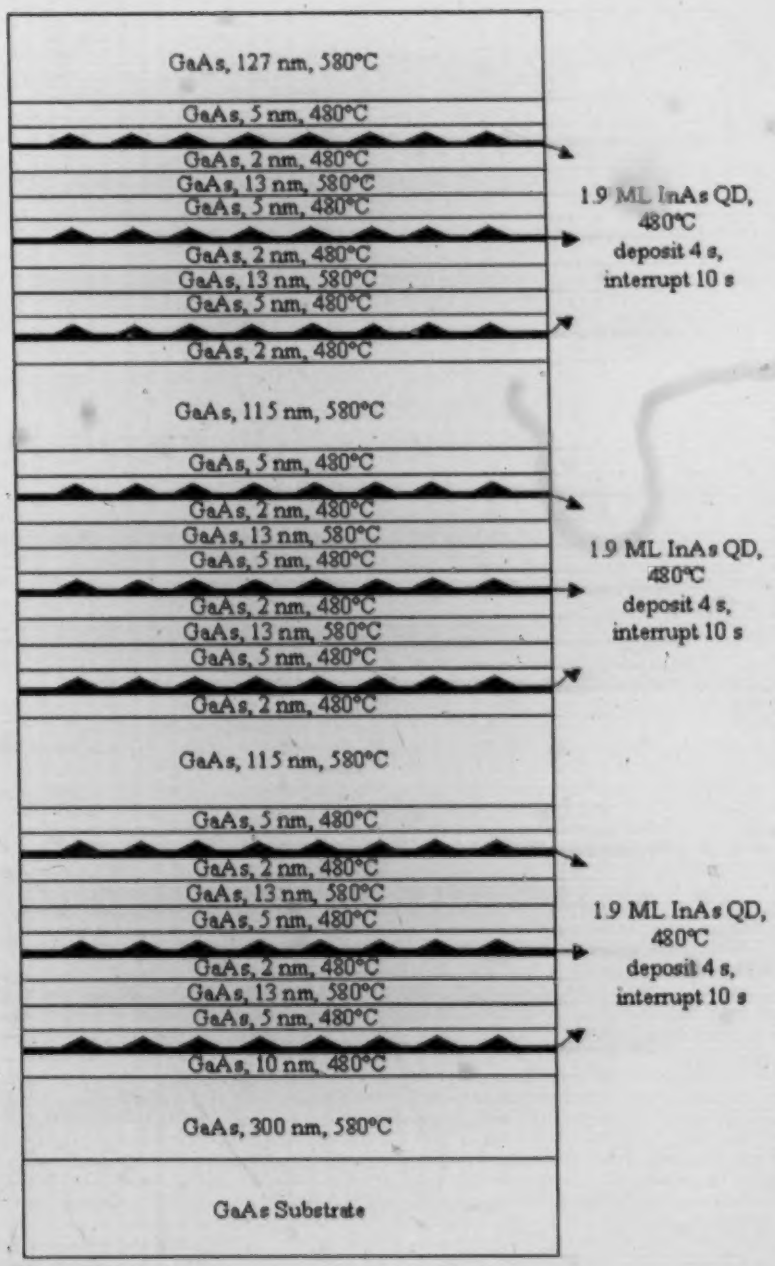
GaAs, 127 nm, 580°C
GaAs, 5 nm, 480°C
GaAs, 2 nm, 480°C
GaAs, 13 nm, 580°C
GaAs, 5 nm, 480°C
1.9 ML InAs QD, 480°C deposit 4 s, interrupt 10 s
GaAs, 2 nm, 480°C
GaAs, 13 nm, 580°C
GaAs, 5 nm, 480°C
GaAs, 2 nm, 480°C
GaAs, 115 nm, 580°C
GaAs, 5 nm, 480°C
GaAs, 2 nm, 480°C
GaAs, 13 nm, 580°C
GaAs, 5 nm, 480°C
1.9 ML InAs QD, 480°C deposit 4 s, interrupt 10 s
GaAs, 2 nm, 480°C
GaAs, 13 nm, 580°C
GaAs, 5 nm, 480°C
GaAs, 2 nm, 480°C
GaAs, 115 nm, 580°C
GaAs, 5 nm, 480°C
GaAs, 2 nm, 480°C
GaAs, 13 nm, 580°C
GaAs, 5 nm, 480°C
1.9 ML InAs QD, 480°C deposit 4 s, interrupt 10 s
GaAs, 2 nm, 480°C
GaAs, 13 nm, 580°C
GaAs, 5 nm, 480°C
GaAs, 10 nm, 480°C
GaAs, 300 nm, 580°C
GaAs Substrate

Figure 23: Growth sequence of a three by three stacked InAs/GaAs QD layers.

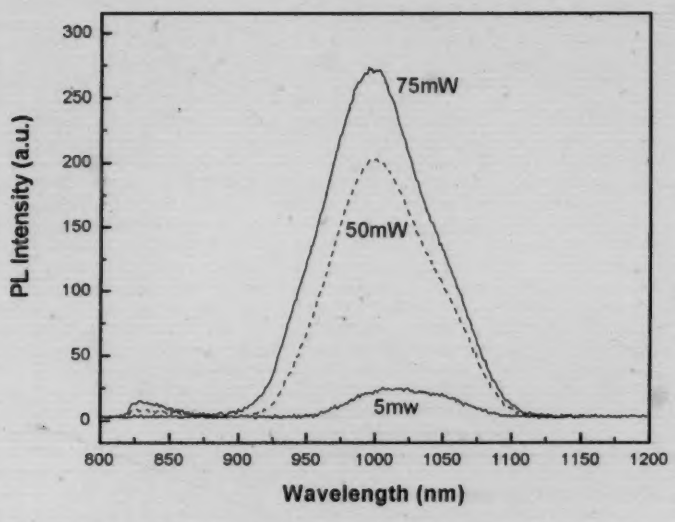

Figure 24: PL spectrum at 4K of the three by three QD layer test sample.

coupling between QD layers, the multiple three by three QD structure gives us the high intensity QD-PL signal at 4K. A small blue shift can be observed from 1020nm to 1000nm and to 990nm when the excitation power was increased from 5mW to 50mW and to 75mW. This can be explained by the different contributions of the QD ground state and first excited state emissions with excitation power increase. We believe that when the excitation power is increased the ground state emission saturates and the first excited state emission (which is located to shorter wavelength) increases and hence the total QD PL spectral contribution shifts to shorter wavelengths. We believe that the emission from about 1020nm (at 4K) for the 5mW excitation power is appropriate for the final device operation. It is expected that the central

QD bandgap to be about 1070nm at RT if this set of conditions will be used for the fabrication of the final QD-SAM device.

3.2.4 QD-SAM device fabrication

Finally, the QD-SAM device was fabricated. The best parameters that were determined for the fabrication of the QD material and DBR test sample were implemented in the final device growth. Figure 25 shows the sequence of layers and parameters that we used during the QD-SAM device fabrication.

The device fabrication starts with the 25 pair DBR growth. 90.6nm of AlAs and 76.5 GaAs were used to form each of the DBR pair. We used 580^0C growth temperature combined with 60 s growth interruption after each GaAs layer and 40 s after each AlAs layer growth. The deposition rate for both AlAs and GaAs was $0.42\mu m/h$. Following the growth of the DBR, three groups of three layers of self-assembled InAs/GaAs QDs were grown. A thickness of 1.9 ML of InAs at 480^0C and 0.04 ML/s growth rate were supplied in 12 periods of 4 s deposition and 10 s interruption in order form each of the nine QD layers. A 20 nm GaAs layer separated the InAs QD layers within each group of QDs. Finally the structure was covered with a 132 nm GaAs layer. The GaAs spacing layer of the QD individual groups was adjusted to 112nm in order to give the total thickness of the structure (starting from the last deposited AlAs DBR layer to the crystal surface) of 612 nm. The As pressure during growth was $\sim 2.4 \cdot 10^{-6}$Pa, sufficient to ensure an As-stabilized surface,

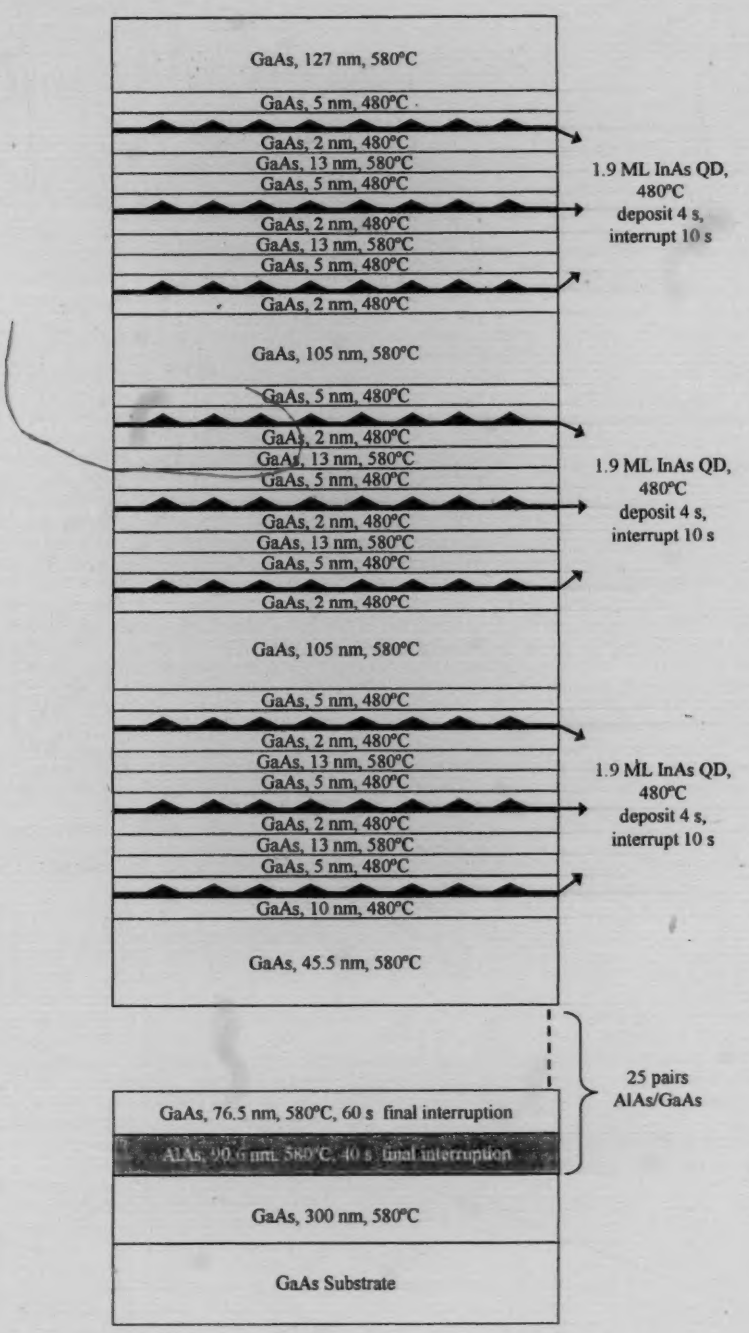
GaAs, 127 nm, 580°C
GaAs, 5 nm, 480°C
GaAs, 2 nm, 480°C
GaAs, 13 nm, 580°C
GaAs, 5 nm, 480°C
GaAs, 2 nm, 480°C
GaAs, 13 nm, 580°C
GaAs, 5 nm, 480°C
GaAs, 2 nm, 480°C
1.9 ML InAs QD, 480°C deposit 4 s, interrupt 10 s
GaAs, 105 nm, 580°C
GaAs, 5 nm, 480°C
GaAs, 2 nm, 480°C
GaAs, 13 nm, 580°C
GaAs, 5 nm, 480°C
GaAs, 2 nm, 480°C
GaAs, 13 nm, 580°C
GaAs, 5 nm, 480°C
GaAs, 2 nm, 480°C
1.9 ML InAs QD, 480°C deposit 4 s, interrupt 10 s
GaAs, 105 nm, 580°C
GaAs, 5 nm, 480°C
GaAs, 2 nm, 480°C
GaAs, 13 nm, 580°C
GaAs, 5 nm, 480°C
GaAs, 2 nm, 480°C
GaAs, 13 nm, 580°C
GaAs, 5 nm, 480°C
GaAs, 2 nm, 480°C
1.9 ML InAs QD, 480°C deposit 4 s, interrupt 10 s
GaAs, 10 nm, 480°C
GaAs, 45.5 nm, 580°C
25 pairs AlAs/GaAs
GaAs, 76.5 nm, 580°C, 60 s final interruption
AlAs, 90.5 nm, 580°C, 40 s final interruption
GaAs, 300 nm, 580°C
GaAs Substrate

Figure 25: Growth sequence of the QD-SAM device.

but low enough to allow good Indium atom surface-mobility before bonding with the As atoms. Similar As pressures have been reported in [60] to give high quality self-assembled InAs/GaAs QDs.

Generally, in MBE growth, the parameters are designed for the center of the substrate, which is then continually rotated during growth in order to produce a good uniformity of the structure across the entire surface. Therefore, the amounts and ratios of different materials deposited on various positions of the substrate, from the differently located MBE effusion cells, will be similar. For the fabrication of all our test samples the substrate was continually rotated during the growth process. For the fabrication of the QD-SAM we used no substrate rotation. In the case when the substrate is not rotated during the growth process, the different material layers will have different thicknesses and ratios across the wafer. For the case of the QD-SAM this translates to a variation in the reflectivity spectrum of the DBR and a variation in the QD size (which determines the QD photoluminescence/absorption spectra) across the wafer.

3.3 Device characterization

This section reproduces the information on QD-SAM characterization presented by our group in the articles [44, 45, 46].

After the final QD-SAM device is fabricated, a detailed analysis is necessary to be performed in order to determine the suitability of the device for

operation in a laser cavity as a saturable absorber mirror. Firstly, we are interested to analyze the Scanning Electron Microscope cross-section of our device. From this cross-section image we expect to determine the structural correlation between our design and its physical implementation. Any major structural errors or long range crystal defects are possible to be observed from the SEM images. Secondly, it is necessary to measure the low intensity reflectivity spectrum of the QD-SAM, where it is expected to observe an absorption dip in the DBR high reflectivity plateau caused by the QD absorption. Thirdly, we are interested in determining the photoluminescence spectrum of the QD-SAM structure. This would confirm the existence of the QDs and would indicate their bandgap and crystal quality. Both the reflectivity and luminescence spectra will be measured at room temperature.

Because of the fact that no wafer rotation was used during the QD-SAM epitaxial growth, we expect that various reflectivity and photoluminescence spectra have been obtained across the wafer. For this reason a mapping measurement process has to be performed. In the next three subsections we will present in details the QD-SAM characterization processes and the setups used for doing the characterizations.

3.3.1 Scanning Electron Microscope analysis

Figure 26 shows the Scanning Electron Microscope (SEM) cross-section of our QD-SAM device. We have used an SEM equipment model JEOL 6301F that

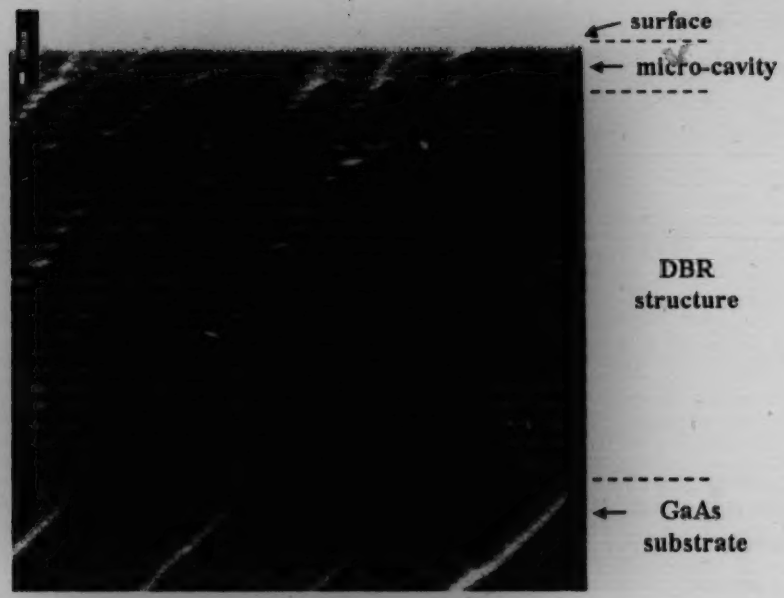

Figure 26: SEM cross-section of the QD-SAM device.

provides high-resolution digital images of microstructures at magnifications ranging from 20x to 250,000x. The SEM equipment was available in the Earth Science Department of our University. The sample was prepared by cleaving a corner of the wafer, from the wafer front facet. No coating was applied on the sample during the SEM analysis.

From this cross-section image we have observed good repeatability of the DBR structure and the sharp interfaces between its layers. Unfortunately, we have identified structural errors on the last five layers of AlAs from the distributed reflector structure. Thus, the bottom DBR of the QD-SAM device is formed by only 20 AlAs/GaAs pairs instead of the original designed number of 25 pairs, and the top GaAs micro-cavity is now thicker than the designed

value. We suspect this error was due to the emptying or malfunction of the Aluminium effusion cell source.

At this stage of the device characterization we have concluded that while this structure is not ideal, it should still allow it to operate as saturable absorber mirror. The lack of 5 pairs out of 25 of the bottom DBR it is expected to reduce the reflectivity with 0.1% theoretical (from 99.98% for 25 pairs to 99.87% for 20 pairs). Practically, by taking into account the non-ideal step transition between the layers and the unavoidable thickness variation of the DBR layers, this structural error it is expected to introduce maximum few percents reduction of the device reflection.

The white lines that wrinkle across the SEM image come from the preparation of the analyzed sample. We have observed that when the structure is cleaved from the wafer front facet, the crystal cleaving leads to this surface non-uniformities. The electrons accumulates on these prominent areas and appear brighter on the SEM image. This explanation is sustained by the fact that the white lines are also present on the bottom GaAs wafer. When similar structures were cleaved from the wafer back facet, these white lines were absent.

The nine InAs/GaAs QD layers located within the top GaAs micro-cavity are not visible on the SEM cross-section image due to the limited resolution of this microscopy method. For QD materials deposited using similar parameters the QDs are pyramidal in shape with a base of 15 - 20 nm and the height of

1.5 - 3 nm [55, 56].

3.3.2 QD-SAM low intensity reflectivity

The measurements of the QD-SAM low-intensity reflectivity spectra were realized in the NanoFab facility at our university (University of Alberta). These measurements were performed at room temperature by using a Perkin-Elmer Lambda 900 UV/Vis/NIR dual beam spectrophotometer. Figure 27 (a) shows the image of the optical setup that was used to measure the reflectivity spectra. Figure 27 (b) shows the schematic diagram of this setup. These measurements use two light beams, a reference beam and a sample beam, both provided by the spectrophotometer's internal lamp. The reference beam is directly supplied to the photodetector (represented by an integrating sphere), while the sample beam is reflected on the QD-SAM before being directed to the photodetector entrance. The wavelength of the both beams is scanned, and the photodetector reads the sum of the two beams intensity. An initial calibration is necessary to set the 100% reflectivity value for the spectral range of interest, in our case between 900 nm and 1200 nm. This reflectivity calibration was realized with a commercial Au mirror where the reflectivity of the Au mirror was taken as 98% at these wavelengths [61]. Because both beams supplied by the spectrophotometer were not collimated, we used concave and convex mirrors to realize the desired setup presented in figure 27 (b). The sample beam was focused on the QD-SAM surface with an elliptical spot size of approxi-

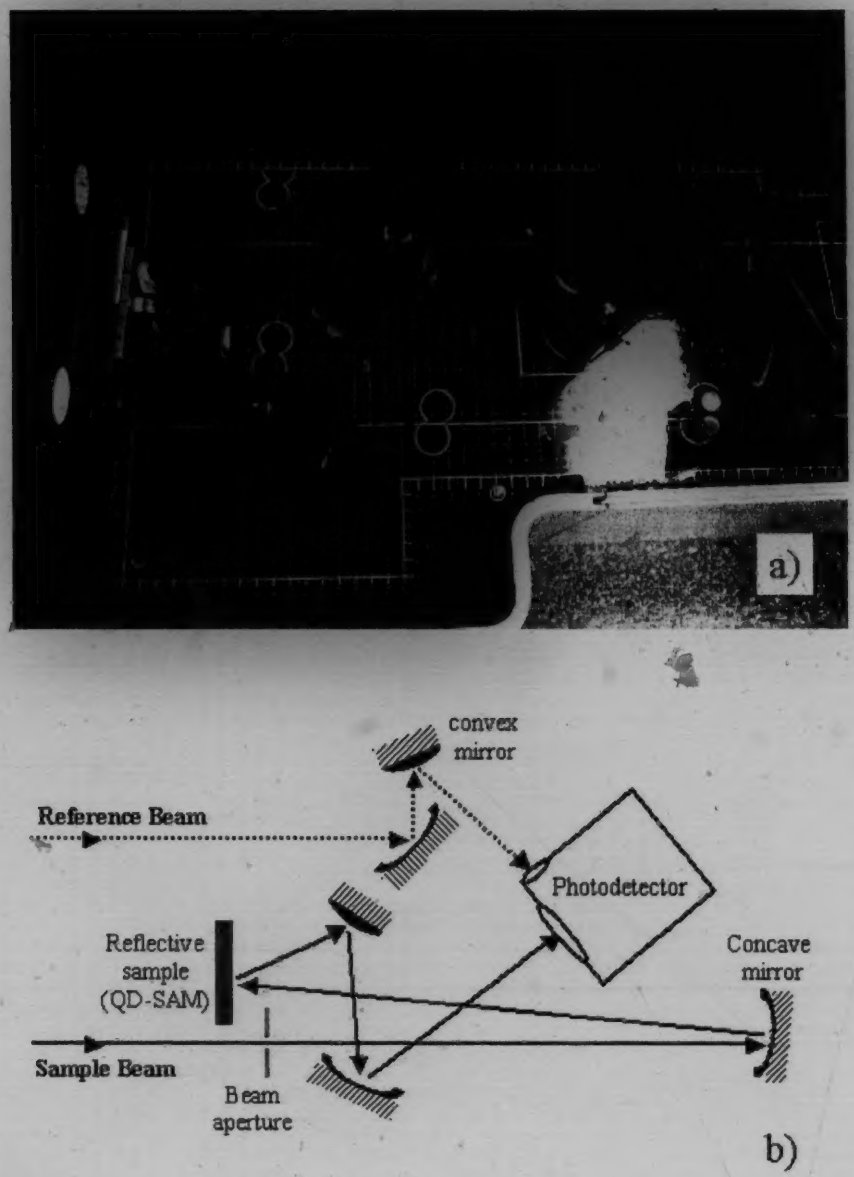

Figure 27: Photo (a), and schematic diagram (b) of the setup used to measure the QD-SAM low intensity reflectivity.

mately $1mm \times 1.5mm$. A variable aperture was used to control the sample beam spot size. The beam incidence angle on the sample was measured to be approximately 10^0. We estimate that the shift in the reflectivity spectrum introduced by the 10^0 angle compared with the normal incidence is about 1 nm shorter in wavelengths, which for our broad spectrum measurements can be neglected. For this reason, for these types of measurements, angles about 10^0 or smaller are considered here as "small-angle incidence".

Figure 28 shows the low-intensity reflectivity spectrum of the QD-SAM device measured at four different points on the wafer. Due to the fact that no rotation was used during the growth, various reflectivity spectra have been obtained across the wafer.

Figure 28 (a), (b), (c) and (d) corresponds to the spectra measured at positions A, B, C and D on the QD-SAM wafer presented in figure 28 (e). The position of the wafer relative to the effusion cells location it is also shown in figure 28 (e). In these spectra one can observe dips (26% at 984 nm for position D, 31% at 1048 nm for C, 27% at 1061 nm for B, and 22% at 1080 nm for A) in the high reflectivity plateaus that are attributed to QD absorption combined with a Fabry Perot resonance between entrance surface and DBR stack. By changing the position on the wafer we have obtained reflectivity spectra with the dip continuously varying from 984 nm to 1080 nm. This has been identified as the potential operating wavelength range for passive mode-locking of lasers using our QD-SAM device.

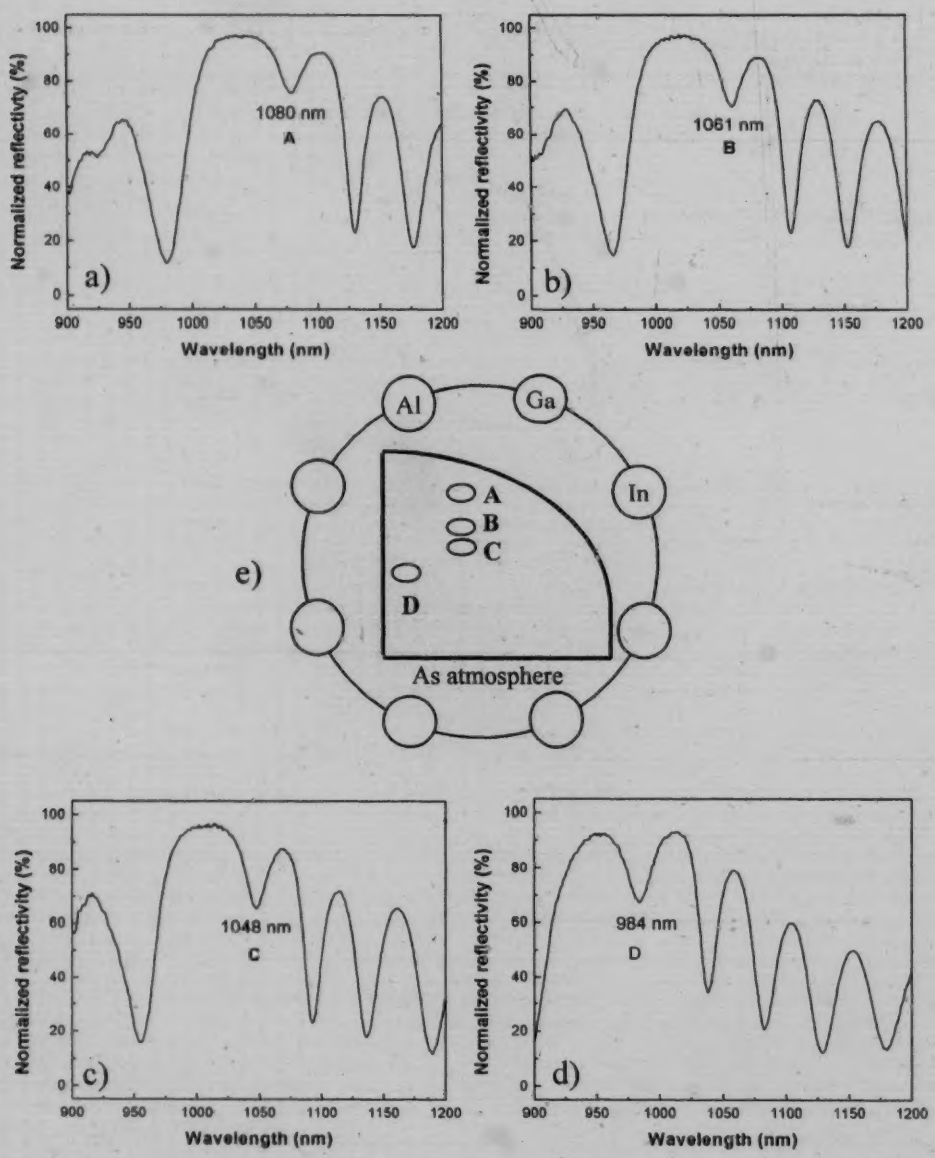

Figure 28: (a)-(d) Low-intensity reflectivity spectrum at position A to D on the QD-SAM; (e) Schematic figure of MBE sources and wafer position during QD-SAM growth.

Positions A, B and C were in a straight line, with a distance in the wafer plane of $\sim 6mm$ from A to C. Since the amount of Al and Ga materials deposited decreases from position A to C, the DBR spectrum shifts to shorter wavelength from A to C. Because of the amount of In material deposited varied slightly at different positions, the dips of 22%, 27% and 31% in reflectivity spectra, which were attributed to the QD absorption, appeared at 1080nm, 1061nm and 1048nm respectively for positions A to C. The position D was $\sim 7mm$ from position C, thus the distances from In, Ga and Al sources to position D are longer compared to that of the position C, so that the DBR high reflectivity plateau is further shifted to a shorter wavelength. Also the absorption from the QD absorber is shifted to around 984 nm with a 26% dip. It can be observed that the maximum reflectivity of the QD-SAM were $\sim 97\%$ for positions A, B and D, and $\sim 93\%$ for position D, but these values may have been reduced by the QD broad absorption spectrum associated with the dot size distribution.

From all these different areas on the wafer surface, we have identified the spectrum of area B (shown in figure 28 (b)) as being appropriate for mode-locked operation tests on the $Nd:YVO_4$ laser system that operates at 1064nm. At this location on the wafer, the DBR high reflectivity plateau shows a 27% dip at $\lambda = 1061nm$ (wavelength in the vicinity of the peak emission of $\lambda = 1064nm$ of the $Nd:YVO_4$ laser) and a high reflectivity plateau spectrum $> 70nm$ wide. Therefore area B will be used for the mode-locking tests

(performed on a $Nd:YVO_4$ laser at $\lambda = 1064nm$) which will be presented in detail in the next chapter (Chapter 5).

Moreover, the characterization of the device reveals the potential of our QD-SAM device to be used for mode-locking of different solid-state lasers in a $\sim 100nm$ wavelength operating range, from 984nm to 1080nm.

3.3.3 QD photoluminescence spectra

The examination of photoluminescence (PL) spectrum it is a widely used method for studying the various material properties. Specifically, light is directed onto a sample, where it is absorbed and delivers the excess energy into the material in a process called photo-excitation. One of the ways this excess energy can be dissipated by the sample is by emission of light, or luminescence. In the case of photo-excitation, this luminescence is called photoluminescence. The intensity and spectral content of this photoluminescence is a direct measure of different important material properties. The energy of the PL is related to the difference in energy levels between the two electron states involved in the transition (between the excited state and the equilibrium state), while the quantity of the PL is related to the relative contribution of the radiative process.

Band gap determination is particularly useful when working with new compound semiconductors like quantum dots. Radiative transitions in semiconductors also involve localized defect levels. The PL energy associated with

these levels can be used to identify specific defects, while the amount of PL can be used to determine the defect concentration. Analyzing the PL spectrum contributes to the understanding of the physics of recombination mechanisms. In general, non-radiative processes are associated with localized defect levels, whose presence is injurious to material quality and therefore to the device performance. Thus, material quality can be measured by quantifying the amount of radiative recombination.

We measured the room temperature photoluminescence (RT-PL) from the QD-SAM device and from a QD test sample. These measurements were performed in our laboratory, where an optical setup was built to perform this task. In general, the most common difficulties encountered when analyzing the RT-PL spectrum come from the weak intensity of the QD photoluminescence combined with the necessity of using a highly sensitive detection system. Figure 29 shows the image (a) and the schematic diagram (b) of the setup used to measure the RT-PL from the QDs. In this case a 20 mW CW diode laser at 790 nm was used to excite the QD structures. The laser was focused using a 20 cm focal length lens to a quasi-circular spot on the sample of 260μm FWHM. The focal spot measurements were based on the knife edge technique. The spectral emission from the QDs was recorded using an Acton Research Corporation (ARC) 500 Spectrometer [63] equipped with a near-infrared (NIR) Optical Multichannel Analyzer (OMA) detector [64]. The NIR detector is an $InGaAs/InP$ 256 pixel-CCD (Model 1452NIR, Princeton) operated at -5^0C.

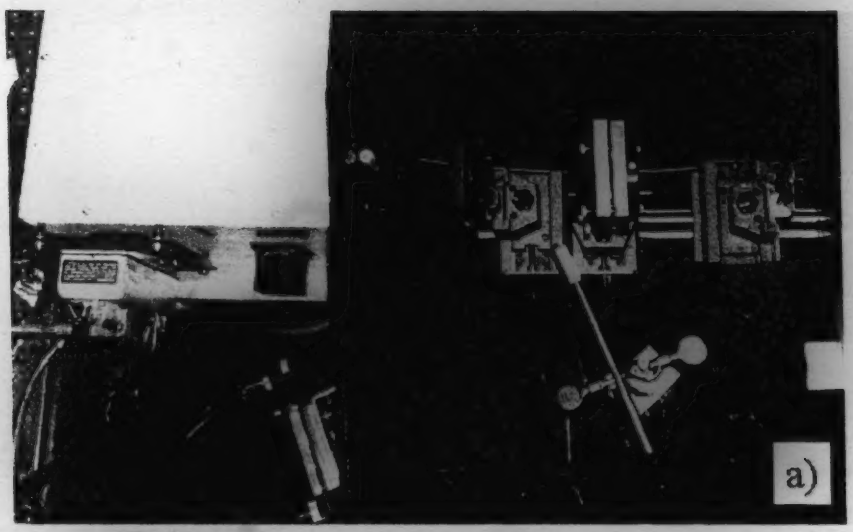

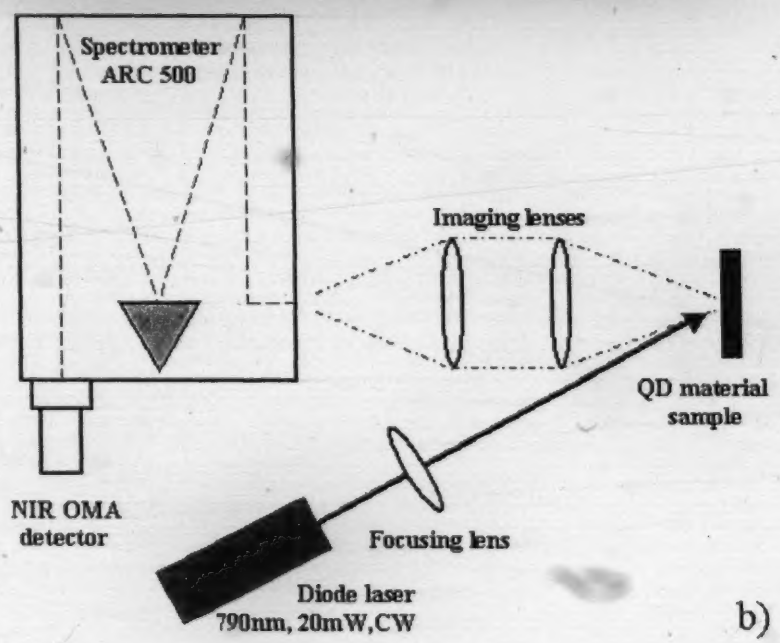

Figure 29: Photo (a), and schematic diagram (b) of the setup used to measure the room temperature photoluminescence from the QDs.

The emission from the QD was imaged 1:1 onto the entrance slit of the spectrometer, which was set to 1 mm for the experimental data presented here. A 600 lines/mm grating was used in the spectrometer giving a dispersion of 2.94 nm/mm at the detector.

Figure 30 shows the QD-SAM photoluminescence correlated with the low-intensity reflectivity spectrum at the same position B, and the photoluminescence of a QD test sample. All spectra are measured at room temperature. The QD-PL spectra are assembled from measurements over smaller spectral ranges of ~37.6 nm each.

The QD test sample contains twenty one QD-layers (seven groups of three QD-layers) grown in similar conditions as the QDs from the QD-SAM device, and the RT-PL measurements were performed in a similar area on the substrate with regard to the In source location. Comparing with the QD-SAM device, this QD test structure has no bottom DBR. Interestingly, we have detected PL signals from both the QD structures and GaAs host material. In figure 30, the emission from the test sample with the peak in the vicinity of 1055 nm and width of 60 nm FWHM corresponds to the QD photoluminescence, and the long wavelength range emission ascendent tail originates from the GaAs substrate luminescence due to the 790 nm pump laser. In order to confirm this hypotheses, we analyzed the RT-PL from bare GaAs samples, and similar emission in the long wavelength range were measured. Even though GaAs bandgap wavelength is 872nm (at RT), it may present deep energy levels within

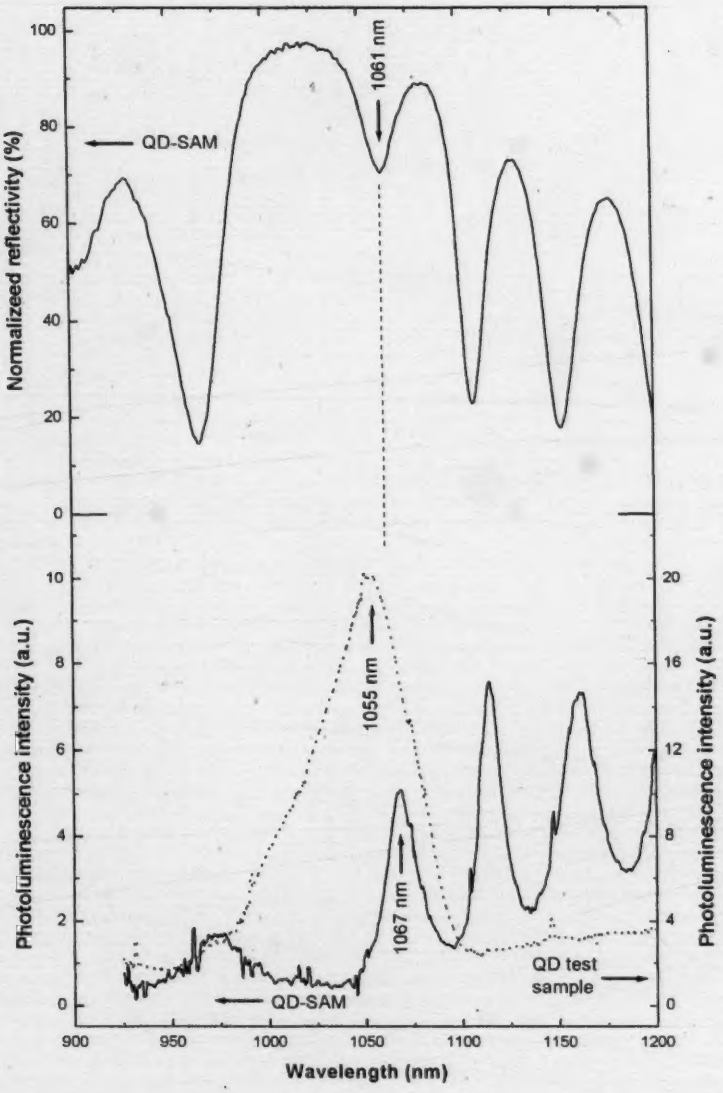

Figure 30: QD-SAM PL correlated with the low-intensity reflectivity spectrum at the same position B, and the PL of a QD test sample; all spectra are measured at room temperature.

the bandgap caused by residual impurities doping or crystal defects. These energy levels may have radiative recombination and hence PL emission can be observed at wavelengths (energies) longer (smaller) than the bandgap.

It can be observed that the maximum in the QD-PL spectrum of the test sample (λ = 1055 nm) is at similar wavelength as the dip in the QD-SAM device reflectivity spectrum (λ = 1061 nm). For this reason we expect that the maximum absorption from the QDs to happen at the wavelength similar with the dip in the reflectivity spectrum.

In contrast with the test sample, the RT-PL spectrum of the QD-SAM device at position B (presented in figure 30) shows multiple emission peaks in the entire measurement range (from 925 nm to 1200 nm). On one hand, we have identified PL emission peaks at 975 nm, 1067 nm, 1115 nm and 1160 nm. On the other hand, our InAs/GaAs quantum dots were designed and fabricated for a bandgap of about 1064 nm at RT (similar with the QD test sample previously discussed). Therefore the PL emission (ground state) from the QDs of the device is expected to be observed at about 1064 nm, and any emission at longer wavelength may come from the GaAs host material. When this PL signal is correlated with the low intensity reflectivity spectrum at the same position on the wafer, we can observe that the maxima in the PL signal correspond to the minima in the reflectivity spectrum. We have observed this correlation between the two spectra at all positions on the QD-SAM wafer. We explain this complex QD-SAM PL signal as being a combination of QD luminescence,

GaAs luminescence, modulation induced by the GaAs top micro-cavity, and modulation introduced by the bottom DBR.

We believe that the pure emission from the nine QD layers of the QD-SAM device is similar with the one from the QD test structure (which contains twenty one dot layers), but with a smaller intensity due to the reduced number of QD layers. This emission from the QD is than modulated by the top GaAs micro-cavity at its resonance wavelength of 1067 nm (for position B) and it allows only the emission observed at 1067 nm to propagate in the micro-cavity, the other wavelengths being attenuated (by destructive interference in the micro-cavity). The small difference between the 1061 nm dip in the reflectivity spectrum and the 1067 nm peak in the PL spectrum most likely came from the positioning error of the light beams on area B of the wafer. The other PL emission peaks from outside the high reflectivity stop band of the DBR probably came from the modulation induced by the stack mirror.

In order to rule out the possibility of the PL peaks to come from classical QD luminescence, we have analyzed the peaks width and spacing. Usually, good quality InAs/GaAs self-assembled QD material (not single dot material) have luminescence lines from ground state or excited states which are broader then 40 nm FWHM. The emission peaks in figure 30 have widths narrower than 25 nm and thus we suspect they are modulated at specific wavelengths by the DBR structure in which they are incorporated. Comparing the PL spectra from the QD test sample and QD-SAM we conclude that the two

peaks from long wavelengths emission (at 1115 nm and 1160 nm) correspond to luminescence induced by the 790 nm pump light absorbed by the GaAs host material. We explain the presence of the peak from 975nm as being part of the ground state QD luminescence caused by the dot size distribution and modulated by the bottom distributed reflector. This peak most probably does not come from the first excited state emission of the QDs because of the large spacing of 92 nm (or 109 meV) between this peak and the ground state emission. The analysis of the three QD-layer test sample used for the fabrication process development has shown that the spacing between the ground and excited energy levels for our QD structures is about 35 nm (see figure 22).

To our best knowledge, there is no reported data showing both low intensity reflectivity and photoluminescence spectra of a QD-SAM device, at any wavelength range. The only related information where both spectra were reported is on two studies of QW-SAM devices. In reference [62] similar emission from GaAs host material and correlation between the spectra were observed, and shortly discussed. In reference [6], one can observe complex PL signal and a correlation between the two spectra, but no analysis is presented on this issue.

At this stage of the project we concluded that our QD-SAM device can be used as a saturable absorber for passive laser mode-locking in the operation range of 984nm - 1080nm. Because of the availability of a $Nd : YVO_4$ laser operating at 1064 nm, we performed the mode-locked operation tests on this

system.

The next chapter will discuss the mode-locked operation tests using our QD-SAM device. In addition, a detailed description of the laser setup used for these tests will be presented.

4 Quantum Dot Saturable Absorber Mirror mode-locked operation

This chapter mainly reproduces the information on QD-SAM mode-locked operation presented by our group in the articles [45, 46].

The tests of the QD-SAM device for passive mode-locking of solid state lasers were carried out at the Institute for Microstructural Sciences, National Research Council of Canada, in collaboration with Dr. John Alcock. The experiments were performed in a two-week period in the month of July, 2006.

4.1 Experimental setup of the laser system

To investigate the QD-SAM device for passive mode-locking we have used the laser setup shown in figure 31. The laser system was previously developed for CW operation [65, 66] at $\lambda = 1064$ nm. The laser gain material consists of a $Nd : YVO_4$ slab with 1% Nd doping and dimensions of 20 mm × 5 mm × 2mm. The slab was optically side-pumped on the 20 mm × 2 mm face by a laser diode array [69] at $\lambda = 808nm$. The pump optical power is variable up to a maximum measured value of 44.5 W. The pump beam was focused on the laser crystal by using the cylindrical lens L3 with f=12.7 mm (the cylindrical axis is perpendicular on the plane of the figure). The crystal side facing the pump was AR coated for $\lambda = 808$ nm. The $Nd : YVO_4$ crystal has a trapezoidal shape in the plane of the figure, with the largest side facing away

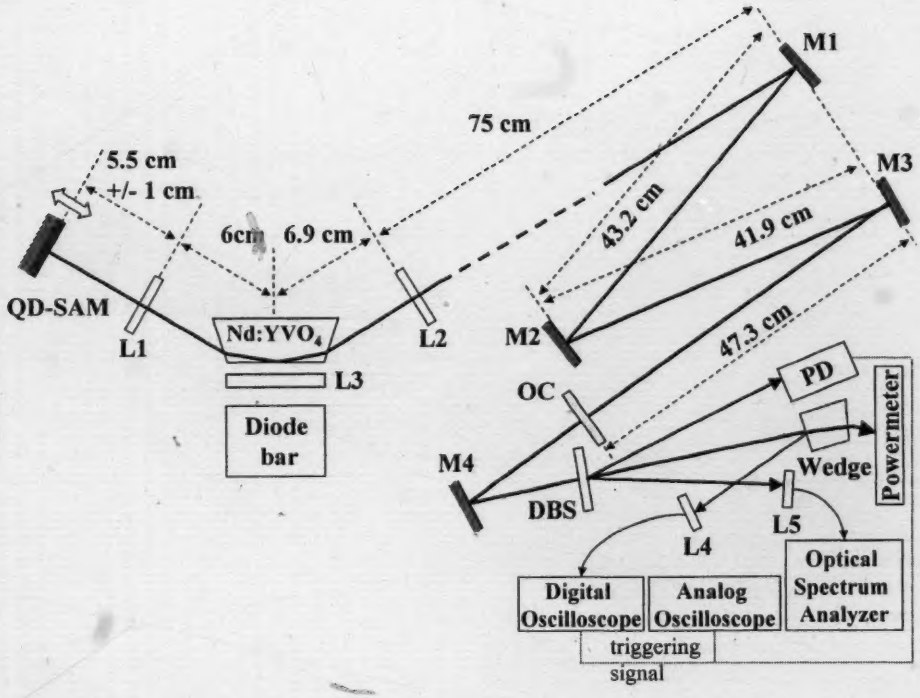

Figure 31: Schematic diagram of the mode-locked laser setup (L1-L5: lenses, M1-M4: dielectric mirrors, PD: photodiode, DBS: diffractive beam splitter, OC: output coupler).

from the pump laser diode array and with the end faces cut at 5° relative to normal. The exit and entrance faces (5 mm × 2 mm) of the laser crystal were AR coated for $\lambda = 1064$ nm for an angle of incidence between 0-20 degrees. The entire assembly, pump-diode-bar plus laser-crystal, was kept at a constant temperature of $14.5°C$ by the use of a water-cooling system, in order to control the pump wavelength and allow stable operation. Two cylindrical lenses L1 and L2 (both with f=5 cm) were used to confine the lasing mode to a narrow stripe within the slab (the cylindrical axes are in the plane of the figure). This geometry uses the total internal reflection on the pumped face of the slab in order to obtain a high degree of overlap between the lasing mode and absorbed pump radiation. The angle of incidence of the laser mode on the pumped face of the $Nd : YVO_4$ slab was approximatively 5.6 degrees. The $Nd : YVO_4$ crystal has an optimum absorption coefficient at ~ 808 nm, which is the wavelength of the pump diode array that we used. This configuration is known as a grazing incidence slab laser (GISL) [65, 66, 67, 68], and has the advantage in achieving a high conversion efficiency of the pump power into lasing power, and high average output power. The high reflectivity laser end mirror was initially a broadband dielectric mirror that was later replaced with our QD-SAM for pulsed operation tests. The position of the end mirror could be adjusted in all three directions over a range of 2 cm for fine-tuning during lasing operation. The laser cavity was folded using the concave mirrors (r=1 m) M1 and M3 and flat mirror M2. The output coupler (OC) defined

the laser cavity length of $226cm \pm 1cm$. Two output couplers of 53% and 15% (at $\lambda = 1064$ nm) were used during mode-locked operation tests. The laser output beam was supplied to the analysis section of the setup by the flat high reflectivity mirror M4. A diffractive beam splitter (DBS) was used to split the laser beam to a photodiode (PD), a power meter and an Optical Spectrum Analyzer. The zero order diffraction beam was directed to the power meter. One of the first order diffraction beams was directed to a photodiode (PD). The PD supplied the electrical signal to the analog oscilloscope and the triggering signal to the fast oscilloscope. The other first order diffraction beam was coupled into a fiber by the use of a focusing lens L5, and supplied the signal to the Optical Spectrum Analyzer. A wedge was used to supply a single surface reflection beam to the optical input of the fast oscilloscope, using a coupling lens L4 to focus onto the fiber. The Optical Spectrum Analyzer was an Advantest model Q8384 with the measurement range 600 nm - 1700 nm. The Spectrum Analyzer calibration was checked with a helium - neon laser that operates at 1152.59 nm and the wavelength measurement accuracy is estimated to be 0.1 nm. The analog oscilloscope used was a Tektronix 7104, and was supplied with the electrical signal from the New Focus 1611 model InGaAs 1 GHz Photodiode. The same photodiode was used to supply the triggering signal to the fast oscilloscope, an Agilent 86100A model. The Agilent oscilloscope was equipped with the optical module 86109A that allows optical input and has a 30 GHz bandwidth, with a measurement range of 1000

nm - 1600 nm.

4.2 Experimental results

Firstly, the laser setup was optimized for CW operation at $\lambda = 1064.6$ nm. It should be noted that the exact peak emission wavelength of the $Nd : YVO_4$ is 1064.6 nm [70], even though commonly the less precise value of 1064 nm is cited for this kind of materials. We have obtained 11 W output average power when a 53% OC was used, and when 42 W of pump power was supplied. This corresponds to a 26.2% laser system optical to optical efficiency.

When the laser mirror was replaced with our QD-SAM, the laser switched from CW operation to self-starting stable CW mode-locked operation. The beam waist occurring at the position of the QD-SAM was slightly elliptical with horizontal diameter $d_h = 671\mu m$ FWHM and vertical diameter $d_v = 749\mu m$ FWHM. The spot size measurements were based on the knife-edge technique, where a partially reflecting mirror was placed in the position of the QD-SAM and the spot size was measured on the back of the mirror. During mode-locked laser operation the analogue oscilloscope was used to monitor the stable CW mode-locked pulse train, while the fast oscilloscope monitored the pulse width and shape.

Figure 32 (a) (~43ns/div time scale) and (b) (~4.3ns/div time scale) shows the analog oscilloscope traces for the CW mode-locked laser operation, when a 53% OC was used. In figure 32 (a) it can be observed the constant amplitude

of the pulses, which proves the continuous-wave (CW) characteristic of the mode-locked operation. In addition, it can be seen that the pulse period is in agreement with the cavity round trip time, and hence the mode-locked operation corresponds to only a single pulse in the resonator cavity (laser operates in single-pulse regime). In figure 32 (b), oscillations in the pulse tail are electrical in origin due to the detection system. These oscillations may indicate that the measured pulse width is close to the detection limit.

The pulse width and pulse bandwidth were simultaneously analyzed and recorded by the use of the fast oscilloscope and optical spectrum analyzer. The accurate determination of the pulse repetition rate was made with the fast oscilloscope. For the case when a 53% OC was used, mode-locked pulses measured on the oscilloscope were as short as $\Delta t = 36$ ps (figure 33) and had a spectral width of $\Delta\lambda = 0.06$ nm (figure 34) at the center wavelength of 1064.6 nm. The resultant time-bandwidth product $\Delta f \Delta t$ was 0.58, and represents 1.3 times the transform limit for Gaussian pulses [24]. The average output power was 7.1 W at a repetition rate of 65 MHz, which gives a pulse peak power of 3 kW. The optical pump power supplied was 40.9 W, and the optical to optical efficiency was 17.2%. From these measurements, the fluence incident on the QD-SAM was estimated to be $42\mu J/cm^2$ (see Appendix C for sample calculation of the operation fluence on the QD-SAM). The reduced efficiency from 26.2% in CW operation to 17.2% in mode-locked operation can be caused by the nonsaturable losses introduced by the QD-SAM, or by

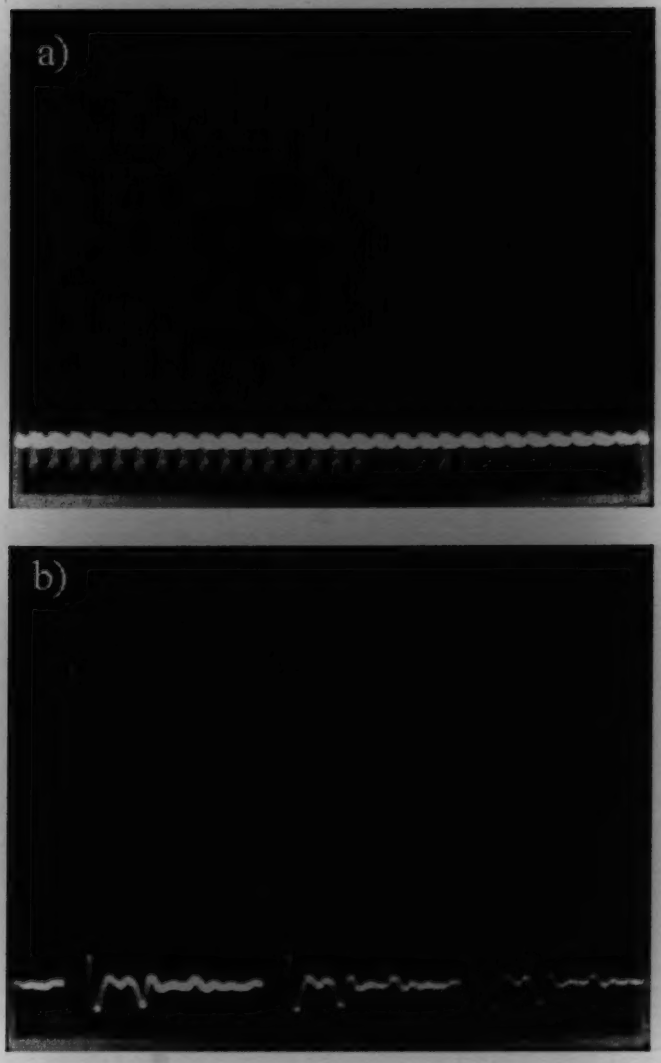

Figure 32: Analogue oscilloscope trace of the CW mode-locked pulse sequence: (a) $\sim$ 43 ns/div time scale, (b) $\sim$ 4.3 ns/div time scale.

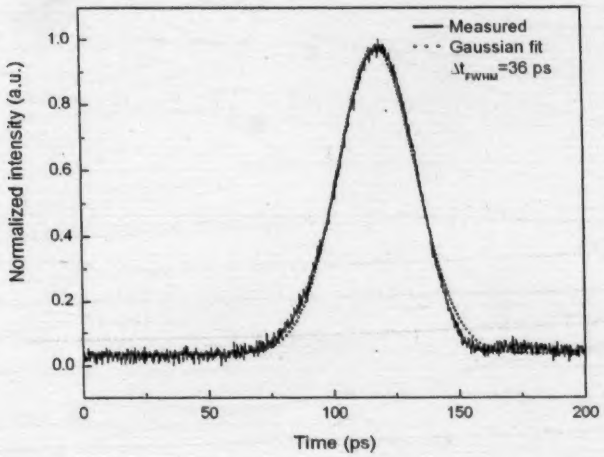

Figure 33: Measured pulse shape when the $Nd : YVO_4$ laser was operated with the 53% output coupler and the QD saturable absorber.

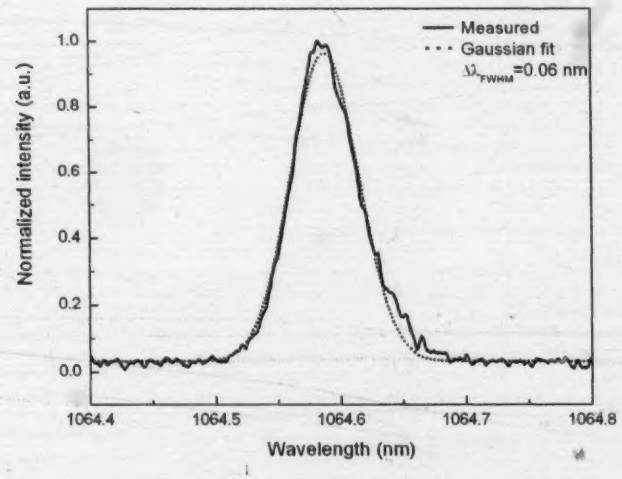

Figure 34: Optical spectrum of the pulses from the $Nd : YVO_4$ laser with the 53% output coupler, when passively mode-locked by using the QD-SAM.

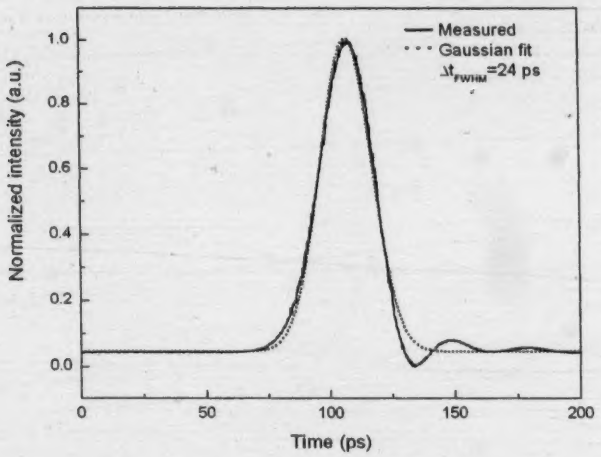

Figure 35: Measured pulse shape when the $Nd : YVO_4$ laser was operated with the 15% output coupler and the QD saturable absorber.

insufficient saturation of the QD structures. For the case when a 15% OC was used, pulses as short as $\Delta t = 24$ ps, as measured on the oscilloscope (figure 35), with a spectral width of $\Delta\lambda = 0.11$ nm (figure 36) at the center wavelength of 1064.6 nm were obtained. In this case the time-bandwidth product was 0.70, or 1.6 times a transform limited Gaussian pulse. We expect that this measurement is somewhat limited by the oscilloscope bandwidth (30 GHz) and the real pulse width would be of the order of 20 ps if a simple deconvolution of the oscilloscope bandwidth would be applied. At the time of our experiments no experimental data was available regarding the minimum pulse width (at the wavelength of 1064.6 nm) that can be measured by the Agilent oscilloscope optical module. As the pulse bandwidth is 0.11 nm, and

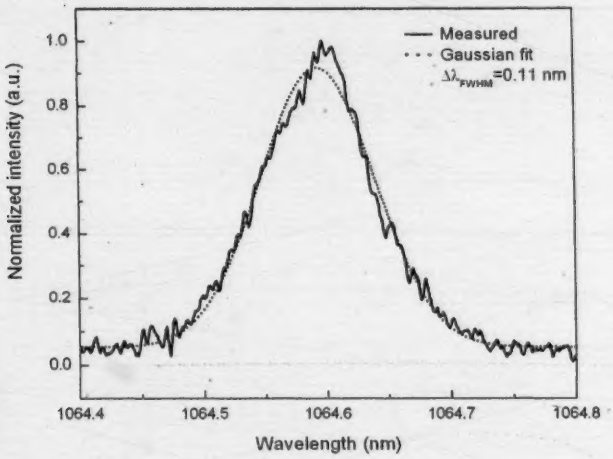

Figure 36: Optical spectrum of the pulses from the $Nd:YVO_4$ laser with the 15% output coupler, when passively mode-locked by using the QD-SAM.

assuming transform limited Gaussian pulses, the minimum pulse width that could be obtained would be 15ps. The average output power was 1.94 W at a repetition rate of 65 MHz, which translates into a peak pulse power of 1.23 kW. The optical pump power supplied was 41.7 W, and the optical to optical efficiency was 4.6%. From these measurements, the fluence incident on the QD-SAM was estimated to be $55\mu J/cm^2$ (see Appendix C for sample calculation).

The mode-locked pulse width Δt is proportional to $\sim 1/N$, where N is the number of laser cavity longitudinal modes that participate in the mode-locked operation (the modes that are phase-locked). As expected, when the transmission of the output coupler was reduced, the cavity losses were reduced

leading to a reduction of the lasing threshold, and in this way more longitudinal modes from the gain spectrum participated in the lasing operation. This leads to the generation of shorter pulses (24 ps) when the 15% OC was used, comparing with the 36 ps pulse width when the 53% OC was used. Analyzing the pulse bandwidth for the 15% OC it can be seen that $\Delta\lambda = 0.11$ nm, which is almost double the pulse bandwidth of $\Delta\lambda = 0.06$ nm obtained for the 53% OC. This broadening in the pulse bandwidth with reduction in the output coupling is consistent with the results observed.

An additional mechanism that could have contributed to the pulse shortening from 36 ps to 24 ps when the OC was reduced from 53% to 15%, is the increase of the operation fluence on the absorber from $42\mu J/cm^2$ to $55\mu J/cm^2$. The increase in the operation fluence could have caused a better saturation of the QDs absorption, and drove to the generation of shorter mode-locked pulses. Commonly, QD-SAM were operated by other groups at much higher fluences relative to their saturation fluence level. At the time of our experiments we had no setup available to perform the saturation fluence measurements on our QD-SAM device, and we estimated this parameter using the literature values for the most similar devices available. The QD-SAM from the reference [14] has a saturation fluence of $20\mu J/cm^2$, the one from reference [15] has a saturation fluence of $25\mu J/cm^2$ and the reference [13] measured a saturation fluence of $14.8\mu J/cm^2$. We believe that our QD-SAM has similar saturation fluence in the range of $15 - 25\mu J/cm^2$.

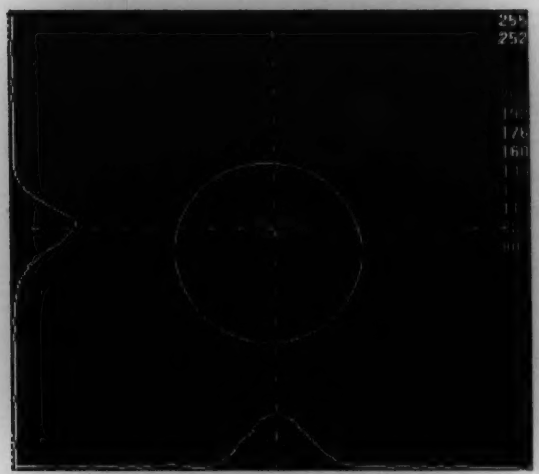

Figure 37: The laser output transverse mode..

On the other hand, the operation fluence on the QD absorber was about $0.7mJ/cm^2$ in the reference [14] (this value was calculated by us using the reported parameters value; see Appendix C for sample calculation), $0.3 - 0.5mJ/cm^2$ in the reference [17] and $2.3mJ/cm^2$ in the reference [12]. Analyzing the fluences value of similar QD-SAM devices it can be observed that the operation fluence is commonly several tens of times larger than the saturation fluence. For our QD-SAM devices the operation fluence during mode-locked operation was only two to four times larger than the estimated saturation fluence. This makes us believe that further analysis and tests are necessary to be performed in order to determine the optimum operation conditions of our QD-SAM device for passive mode-locking.

The laser output transverse mode was analyzed by using a CCD camera. Figure 37 indicates a slightly elliptical spot with a beam diameters ratio of 1.2

and near Gaussian profiles in the two transverse directions. The near Gaussian output mode, combined with the short pulses and the multi-kW peak power make this type of system a good candidate for material processing applications.

When we used the 53% OC we have been able to repeatedly obtain pulses in the range of 36 - 39 ps, and we were able to obtain stable operation for periods of several hours during the two days of experiments. When we used the 15% OC we have been able to obtain pulses of 28 - 30 ps relatively easily, and the laser was stable for another two days of experiments. After fine tuning the optical components of the laser cavity, the positioning of the laser spot on the QD-SAM, and the pump power, we were able to obtain pulses as short as 24 ps.

In summary we have successfully used our InAs/GaAs QD-SAM to mode-lock a $Nd : YVO_4$ laser at 1064.6 nm. To our best knowledge, there is no reported result on mode-locking a $Nd : YVO_4$ laser at $\lambda = 1064$ nm using self-assembled QD saturable absorbers. The only available result in the literature was the work on mode-locking of a $Nd : YVO_4$ laser using QD saturable absorbers at $\lambda = 1342$ nm, using a 0.3% Nd doped crystal, and a 26 ps pulse width was obtained [14].

This page was intentionally left empty.

5 Conclusions and Future Work

In this Master of Science thesis the research and development cycle of a Quantum Dot Saturable Absorber Mirror to be used for ultrashort laser pulses generation via the passive mode-locking mechanism has been reported. Several of the significant findings will now be summarized in the paragraphs below.

A study of the potential use of quantum dots as saturable absorbers for passive mode-locking of laser systems has been carried out, and a device design was proposed for fabrication using Molecular Beam Epitaxy. The design consisted of 9 layers of InAs/GaAs QDs deposited on top of a 25 pairs $\lambda/4$ AlAs/GaAs DBR grown on a GaAs substrate, and optimized for operation at the central wavelength of 1064 nm.

Several test samples have been fabricated and the parameters for QD and DBR fabrication have been identified through SEM and PL measurements. It was found that the deposition of 1.9ML of InAs at the growth rate of 0.04ML/sec, at $480°C$, provided the QD material with the bandgap centered on the desired wavelength of about 1064nm. In addition it was found that the use of multiple stack QD layers gave a better carrier confinement in the dots, as indicated by the strong QD PL signal. The issue of interface sharpness of the DBR layers has been studied. It was found that the use of growth interruption of 60s and 40s after each GaAs and AlAs layer respectively, gave the sharpest interfaces.

The SEM cross-section of the QD-SAM device showed the sharp interfaces of the bottom stack mirror has been achieved. The low intensity reflectivity and PL measurements on the QD-SAM revealed that different absorption wavelengths from 984 nm to 1080 nm were successfully realized on one wafer growth by not rotating the sample during the MBE growth. The 22% to 31% dip in the reflectivity spectrum, which was attributed to quantum dot absorption, indicates the potential for the generation of ultrashort laser pulses through mode-locking of laser systems.

Our QD-SAM device was used for mode-locking operation of a grazing incidence slab $Nd:YVO_4$ laser at λ=1064.6 nm. When the laser end mirror was replaced with the QD-SAM, the laser switched from CW operation to self-starting stable CW mode-locked operation. When an output coupler of 15% was used, mode-locked pulses as short as 24 ps with a repetition rate of 65 MHz were obtained with 1.94 W laser output average power.

Our present work indicated that the InAs/GaAs QD-based structures can be used as saturable absorbers for passive mode-locking Nd doped lasers at 1064 nm. Moreover, the characterization of the device revealed the potential of such a QD-based structure to be used for mode-locking of different solid-state lasers in a $\sim$100 nm wavelengths operating range from 984 nm to 1080 nm.

There are several areas that should be investigated in order to further improve this QD-SAM device. These include further samples and QD-SAM device characterization, additional mode-locked tests, and the development of

a theoretical model for the QD-based device.

An examination of the QDs using Transmission Electron Microscopy would be useful and may provide insight into the atomic structure of the dots.

The measurement of the QD-SAM saturation fluence and modulation depth would allow the optimization of the device design and operation. The measurement of the QD saturation absorption recovery time would offer further information about the QD dynamics. Moreover, a numerical model of the QD-SAM and QD dynamics may provide insight into phenomena occurring during operation and help improving future designs and fabrication.

In addition, it would be of interest to test the QD-SAM device with lasers systems at different wavelengths within the operating range of 984 nm to 1080 nm and with lasers having broader gain bandwidth to generate pulses down to femtosecond pulse duration.

This page was intentionally left empty.

References

[1] K. Smith, N. Langford, W. Sibbett and J. R. Taylor, "A passively mode-locked c.w. rhodamine 700 dye laser", Optica Acta 33, 4 (1986).

[2] W. Sibbett and J. R. Taylor, "Passively Mode-Locking in the Green-Yellow Using the Saturable Absorber DASBTI", IEEE J. of Quantum Electronics 18, 12 (1982).

[3] Y. Pang, F. Wise, "Use of saturable absorber dyes for self-starting operation of a self-mode-locked $Ti : Al_2O_3$ laser", Optical and Quantum Electronics 24, 841(1992).

[4] R. Fluck, R. Haring, R. Pascotta, E. Gini, H. Melchior, U. Keler, "Eyesafe pulsed microchip laser using semiconductor saturable absorber mirrors", Appl. Phy. Lett. 72, 25(1998).

[5] R. Fluck, B. Braun, E. Gini, H. Melchior, and U. Keler, "Passively Q-switched $1.34\mu m$ $Nd : YVO_4$ microchip laser with semiconductor saturable absorber mirrors", Opt. Lett. 22, 13(1997).

[6] O. Okhotnikov, A. Grudinin and M. Pessa, "Ultra-fast fibre laser systems based on SESAM technology: new horizons and applications", New Journal of Physics 6, 177 (2004).

[7] M. J. Lederer, V. Kolev, B. Luther-Davies, H. H. Tan and C. Jagadish "Ion-implanted InGaAs single quantum well semiconductor saturable ab-

sorber mirrors for passive mode-locking", J. Phys. D: Appl. Phys. 34 2455-2464(2001).

[8] D. H. Sutter, G. Steinmeyer, L. Gallmann, N. Matuschek, F. Morier-Genoud, U. Keller,V. Scheuer, G. Angelow, and T. Tschudi, "Semiconductor saturable absorber mirror assisted Kerr-lens mode-locked Ti:sapphire laser producing pulses in the two-cycle regime", Optics Lett. 24, 9 (1999).

[9] G.J. Spuhler, R. Paschotta, M.P. Kullberg, M. Graf, M. Moser, E. Mix, G. Huber, C. Harder, U. Keller, "A passively Q-switched Yb:YAG microchip laser", Appl. Phys. B 72, 285-287 (2001).

[10] B. Braun, F. X. Kartner, G. Zhang, M. Moser, and U. Keller, "56-ps passively Q-switched diode-pumped microchip laser", Opt. Lett. 22,6 (1997).

[11] B. Braun, F. X. Kartner, U. Keller, J.-P. Meyn and G. Huber, "Passively Q-switched 180ps $Nd : LaSc_3(BO_3)_4$ microchip laser", Opt.Lett. 21, 6 (1996).

[12] A. McWilliam, A. A. Lagatsky, C. T. A. Brown, W. Sibbett,A. E. Zhukov, V. M. Ustinov, and A. P. Vasil'ev, E. U. Rafailov "Quantum-dot-based saturable absorber for femtosecond mode-locked operation of a solid-state laser", Opt.Lett.31, 10(2006).

[13] R. Herda, O. G. Okhotnikov, E. U. Rafailov, W. Sibbett, P. Crittenden, and A. Starodumov, "Semiconductor Quantum-Dot Saturable Absorber Mode-Locked Fiber Laser", IEEE Phot. Techn. Lett.18, 1(2006).

[14] K. W. Su, H. C. Lai, A. Li, Y. F. Chen, and K. F. Huang, "InAs/GaAs quantum-dot saturable absorber for a diode-pumped passively mode-locked $Nd:YVO_4$ laser at 1342 nm", Opt.Lett.30, 12(2005).

[15] H. C. Lai, A. Li, K. W. Su, M. L. Ku, Y. F. Chen, and K. F. Huang, "InAs/GaAs quantum-dot saturable absorbers for diode-pumped passively Q-switched Nd-doped $1.3\mu m$ lasers", Opt.Lett.30, 5(2005).

[16] A. A. Lagatsky, E. U. Rafailov, W. Sibbett, D. A. Livshits, A. E. Zhukov, and V. M. Ustinov, "Quantum-Dot-Based Saturable Absorber With p-n Junction for Mode-Locking of Solid-State Lasers", IEEE Phot.Techn.Lett.17, 2 (2005).

[17] E. U. Rafailov, S. J. White, A. A. Lagatsky, A. Miller, W. Sibbett, D. A. Livshits, A. E. Zhukov, and V. M. Ustinov, "Fast Quantum-Dot Saturable Absorber for Passive Mode-Locking of Solid-State Lasers", IEEE Phot. Techn. Lett 16, 11 (2004).

[18] A. M. Malyarevich, V. G. Savitski, P. V. Prokoshin, N. N. Posnov, K. V. Yumashev, E. Raaben, and A. A. Zhilin , "Glass doped with PbS quantum dots as a saturable absorber for $1-\mu m$ neodymium lasers", JOSA B 19, 1, pp. 28-32(2002).

[19] A. M. Malyarevich, P. V. Prokoshin, M. I. Demchuk, K. V. Yumashev, A. A. Lipovskii "Passively Q-switched $Ho^{+3} : Y_3Al_5O_{12}$ laser using a PbSe-doped glass", Appl. Phys. Lett. 78, 5, pp. 572-573(2001).

[20] K. Wundke, S. Pötting, J. Auxier, A. Schülzgen, N. Peyghambarian, N. F. Borrelli,"PbS quantum-dot-doped glasses for ultrashort-pulse generation", Appl. Phys. Lett. 76, 1, pp. 10-12(2000).

[21] H. Y. Liu, I. R. Sellers, T. J. Badcock, D. J. Mowbray,a) and M. S. Skolnick, K. M. Groom, M. Gutiérrez, M. Hopkinson, J. S. Ng, and J. P. R. David, R. Beanland,"Improved performance of 1.3μm multilayer InAs quantum-dot lasers using a high-growth-temperature GaAs spacer layer", Appl. Phys. Lett. 85, 5(2004).

[22] K. Mukai, Y. Nakata, K. Otsubo, M. Sugawara, N. Yokoyama, and H. Ishikawa,"1.3μm CW Lasing of InGaAs-GaAs Quantum Dots at Room Temperature with a Threshold Current of 8 mA", IEEE Phot. Techn. Lett. 11, 10(1999).

[23] L. Zhang and Thomas F. Boggess, D. G. Deppe, D. L. Huffaker, O. B. Shchekin, and C. Cao, "Dynamic response of 1.3-μm-wavelength InGaAs/GaAs quantum dots", Appl. Phys. Lett. 76, 10 (2000).

[24] Kelin J.Kuhn, "Laser Engineering", Prentice Hall 1997, Chapter 6.

[25] William T. Silfvast, "Laser Fundamentals", Cambridge University Press 2004, Chapter 13.

[26] "Encyclopedia of Laser Physics and Technology", online website source: www.rp-photonics.com.

[27] I. F. L. Dias, B. Nabet, A. Kohl, J. L. Benchimol, and J. C. Harmand, "Electrical and Optical Characteristics of n-Type-Doped Distributed Bragg Mirrors on InP", IEEE Photon. Technol. Lett. 10, 6 (1998).

[28] N. Nishiyama, C. Caneau, B. Hall, G. Guryanov, M. H. Hu, X. S. Liu, M.-J. Li, R. Bhat, and C. E. Zah, "Long-Wavelength Vertical-Cavity Surface-Emitting Lasers on InP With Lattice Matched AlGaInAs-InP DBR Grown by MOCVD", IEEE J Selected Topics in Quantum Electronics 11, 5 (2005).

[29] C. Honninger, R. Paschotta, F. Morier-Genoud, M. Moser, and U. Keller, "Q-switching stability limits of continuous-wave passive mode locking", J. Opt. Soc. Am. B, 16, 1 (1999).

[30] U. Keller, K. J. Weingarten, F. X. Kartner, D. Kopf, B. Braun, I. D. Jung, R. Fluck, C. Honninger, N. Matuschek, and J. Aus der Au, "Semiconductor Saturable Absorber Mirrors (SESAM's) for Femtosecond to Nanosecond Pulse Generation in Solid-State Lasers", IEEE J Selected Topics in Quantum Electronics 2, 3 (1996).

[31] Richard L. Sutherland, with contributions by Daniel G. McLean, S. Kirkpatrick, "Handbook of nonlinear optics", electronic resource or published : Marcel Dekker, New York, chapter 9, (2003).

[32] B. E. A. Saleh, M. C. Teich, "Fundamentals of Photonics", Wiley-Interscience, chapter 15 (1991).

[33] Sadao Adachi, "Physical Properties of III-V Semiconductor Compounds: InP, InAs, GaAs, GaP, InGaAs, and InGaAsP", Wiley-Interscience (1992).

[34] Robert W. Boyd, "Nonlinear Optics-second edition", Academic Press 2003, Chapter 1.

[35] U. Keller, "Recent developments in compact ultrafast lasers", Nature 424, 14 (2003).

[36] N. Xiang, 0. Okhotnikov, A. Vainionpaa, M. Guina and M. Pessa, "Broadband semiconductor saturable absorber mirror at $1.55\mu m$ using Burstein-Moss shifted $Ga_{0.47}In_{0.53}As/InP$ distributed Bragg reflector", Electron.Lett.37, 374(2001).

[37] A. R. Kovsh, N. A. Maleev, A. E. Zhukov, S. S. Mikhrin, A. P. Vasil'ev, Yu. M. Shernyakov, M. V. Maximov, D. A. Livshits, V. M. Ustinov, Zh. I. Alferov, N. N. Ledentsov, and D. Bimberg, "InAs/InGaAs/GaAs

quantum dot lasers of 1.3μm range with high (88%) differential efficiency", Electron. Lett. 38, 1104-1106 (2002).

[38] P. Bhattaharya, S. Ghosh, and A.D. Stiff-Roberts, "Quantum Dot Opto-Electronic Devices", Annual Review of Materials Research 34, 1-40 (2004).

[39] P. R. Berger, K. Chang, P. Bhattacharya and J. Singh, "Role of strain and growth conditions on the growth front profile of $In_xGa_{1-x}As$ on $GaAs$ during the pseudomorphic growth regime", Appl. Phys. Lett.53, 684-86(1988).

[40] Dieter Bimberg, Marius Grundmann, Nikolai N.Ledentsov, "Quantum Dot Heterostructures", John Wiley & Sons 1999.

[41] M. Grundmann, N. N. Ledentsov, O. Stier, D. Bimberg, V. M. Ustinov, P. S. Kop'ev, and Zh. I. Alferov, "Excited states in self-organized InAs/GaAs quantum dots: Theory and experiment", Appl. Phys. Lett.68, 979-81(1996).

[42] R. Leon, S. Fafard, D. Leonard, J. L. Merz, and P. M. Petroff, "Visible luminescence from semiconductor quantum dots in large ensembles", Appl. Phys. Lett.67, 521-23(1995).

[43] J. Y. Marzin, G. Bastard "Calculation of the energy levels in InAs/GaAs quantum dots", Solid State Commun. 92.437-42(1994).

[44] Z. Y. Zhang, C. Scurtescu, M. T. Taschuk, Y. Y. Tsui, R. Fedosejevs, M. Blumin, I. Saveliev, S. Yang, H. E. Ruda, "GaAs based semiconductor quantum dot saturable absorber mirror grown by molecular beam epitaxy", Proc. SPIE 6343, 6343N (2006).

[45] C. Scurtescu, Z. Y. Zhang, J. Alcock, R. Fedosejevs, M. Blumin, I. Saveliev, S. Yang, H. E. Ruda, Y. Y. Tsui, "Quantum Dot Saturable Absorber for passive mode-locking of $Nd : YVO_4$ lasers at 1064 nm." Applied Physics B (19 manuscript pages, accepted with minor revisions on February 16, 2007).

[46] C. Scurtescu, Z. Y. Zhang, J. Alcock, R. Fedosejevs, M. Blumin, I. Saveliev, S. Yang, H. E. Ruda, Y. Y. Tsui, "Quantum Dot Based Saturable Absorber for Passive Mode-Locking of Solid State Lasers at 1064 nm," Photons Technical Review, vol. 4, 25-27 (2007).

[47] G. Biasiol and L.Sorba, "Molecular beam epitaxy: Principles and Applications", Edizioni ETS, Pisa, 2001.

[48] Robin F. Farrow, "Molecular Beam Epitaxy-Applications to Key Materials", William Andrew Publishing, 1995, Chapter 1.

[49] M.A. Herman and H. Sitter, "Molecular Beam Epitaxy", Springer, 1997.

[50] L. Krainer, R. Paschotta, S. Lecomte, M. Moser, K. J. Weingarten and U. Keller "Compact $Nd:YVO_4$ Lasers With Pulse Repetition Rates up to 160 GHz", IEEE J.Quantum Electron. 38, 10 (2002).

[51] S. O. Kasap, Chapter 1, "Optoelectronics and Photonics: Principles and Practices", Prentice Hall 2001.

[52] Pochi Yeh, "Optical Waves in Layered Media", John Wiley & Sons 2005.

[53] Max Born, Emil Wolf, Chapter 1.6, "Principles of Optics: Electromagnetic Theory of Propagation, Interference, and Diffraction of Light 7 Rev. ed.", Cambridge University Press 1999.

[54] The Matlab code used to calculate the distributed Bragg reflector spectrum represents a modified version of a code available for the Course on Photonic Devices for Communications, fall 2004, instructor Dr. Ray DeCorby, Electrical and Computer Engineering Department, University of Alberta, Canada.

[55] A. Polimeni, A. Patane, M. Henini, L. Eaves, P.C. Main, S. Sanguinetti, M. Guzzi, "Influence of high-index GaAs substrates on the growth of highly strained (InGa)As/GaAs heterostructures", J. of Crystal Growth 201/202, 276-279(1999).

[56] Z. Y. Zhang, Z. G. Wang, B. Xu, P. Jin, Z. Z. Sun, and F. Q. Liu, "High-Performance Quantum-Dot Superluminescent Diodes", IEEE Phot. Tech. Lett. 16, 1(2004).

[57] J. Ibanez, A. Patane, M. Henini, and L. Eaves, S. Hernandez, R. Cusco, and L. Artus, Yu. G. Musikhin and P. N. Brounkov, "Strain relaxation in stacked InAs/GaAs quantum dots studied by Raman scattering", Appl. Phys. Lett. 83, 15(2003).

[58] R. Heitz, F. Guffarth, K. Pötschke, A. Schliwa, and D. Bimberg, N. D. Zakharov and P. Werner, "Shell-like formation of self-organized InAs/GaAs quantum dots", Phys. Rev. B 71, 045325(2005).

[59] Rasband, W.S., ImageJ, U. S. National Institutes of Health, Bethesda, Maryland, USA, http://rsb.info.nih.gov/ij/, 1997-2006.

[60] M. Blumin, H. E. Ruda, I. G. Savaliev, A. Shik, and H. Wang, "Self-assembled InAs quantum dots and wires grown on a cleaved-edge GaAs (110) surface", J. of Appl. Phys. 99, 093518 (2006).

[61] J. Bass, J. S. Dugdale, C. L. Foiles, A. Myers, "Landolt-Bornstein", Vol. 15b, Springer, Berlin, Heidelberg (1985).

[62] H. D. Sun, G. J. Valentine, R. Macaluso, S. Calvez, D. Burns, and M.D. Dawson, T. Jouhti and M. Pessa, "Low-loss $1.3-\mu m$ GaInNAs saturable

Bragg reflector for high-power picosecond neodimium lasers", Opt. Lett. 27, 23 (2002).

[63] Acton Research Corporation, 0.5 Meter Triple Grating Monochromator/Spectrograph Operating Instructions Manual.

[64] EG&G Instruments Corporation, Silicon Photodiode Detectors Instruction Manual, 1452 NIR Detector Specifications.

[65] A. J. Alcock and J. E. Bernard, "Diode-Pumped Grazing Incidence Slab Lasers", IEEE J. Selected. Topics in Quantum Electron. 3, 3 (1997).

[66] J. E. Bernard and A. J. Alcock, "High-efficiency diode-pumped $Nd:YVO_4$ slab laser", Opt. Lett. 18, 968 (1993).

[67] M. J. Damzen, M. Trew, E. Rosas, G. J. Crofts, "Continuous-wave $Nd:YVO_4$ grazing-incidence laser with 22.5 W output power and 64% conversion efficeincy", Opt. Commun. 196, 237-241 (2001).

[68] A. Minassian, B. Thompson, M. J. Damzen, "Ultrahigh-efficiency TEM_{00} diode-side-pumped $Nd:YVO_4$ laser", Appl. Phys. B 76, 341-343 (2003).

[69] Cutting Edge Optronics, 808 nm 40 W CW Laser Diode Array Technical Specifications Sheet, website www.ceolaser.com

[70] T. Jensen, V. G. Ostroumov, J.-P. Meyn, G. Huber, A. I. Zagumennyi, I. A. Shcherbakov, "Spectroscopic Characterization and Laser Performance of Diode-Laser-Pumped $Nd:GdVO_4$", App. Phys. B 58, 373-379 (1994).

This page was intentionally left empty.

Appendix A

DBR reflectivity and epitaxial growth time - sample calculations

The maximum reflectivity of a DBR structure is given by the relation [52, 53]:

$$R = \left(\frac{1 - (n_s/n_1)(n_2/n_3)^{2N}}{1 + (n_s/n_1)(n_2/n_3)^{2N}} \right)^2, \tag{27}$$

where n_1, n_2, n_3 and n_s are the refractive index of the air, GaAs, AlAs and substrate (GaAs wafer) respectively, and N represents the number of $\lambda/4$ AlAs/GaAs pairs of the stack mirror. The indexes' values are: $n_1 = 1$, $n_2 = n_s = 3.478$ and $n_3 = 2.936$. Using the relation 27, the maximum reflectivity of a 25 pairs AlAs/GaAs DBR is R=99.98%.

As the wavelength of interest is 1064 nm (in air), the thickness of the $\lambda/4$ AlAs layers is 90.6 nm and of GaAs is 76.5 nm. These give the period of the DBR to be 167.1 nm. The growth rate used during the MBE growth of the DBR of the QD-SAM device was 420nm/h, which translates into about 24 minutes per period. If we take into account the growth interruptions (60 s after each GaAs layer and 40 s after each AlAs layer) the total time required to deposit one full period of DBR is about 25.5 minutes. Therefore the time required to deposit 25 pairs is 637.5 minutes (about 10 and a half hours).

This page was intentionally left empty.

Appendix B

DBR reflectivity spectrum

This is the Matlab code used to calculate the distributed Bragg reflector spectrum. It is modified from a code provided by the instructor Dr. DeCorby to the students taking the Graduate Course ECE684 Photonic Devices for Communications, in fall 2004.

On the next page is the copy of the code used for calculation and plotting.

```
% This m-file calculates the reflectivity of a distributed bragg reflector structure, using a transfer-matrix approach.
% The file solves for a square index profile.

% Input parameters:
% nGaAs= refractive index of GaAs
% nAlAs= refractive index of AlAs
% ngrat= number of periods in the structure.
% delgV= grating period in each section.
% dngV= peak-to-peak amplitude of the index modulation in the structure.
% lambda= input vector of free-space wavelengths; it represents the wavelength points we want to simulate the structure.

% initialize data space
nGaAs=3.478;
nAlAs=2.936;
ngrat=25;
delgV=167.1e-9;
dngV=0.542;
lambda=900e-9:1e-10:1250e-9;
lambdaE=1064e-9;
% generate vector of free-space propagation constants
k0=2.*pi./lambda;
% generate vector of frequencies
frequency=3e8./lambda;
% generate the index profile n(z) in the form of a vector of numbers at specific points along z
Ltot=sum(ngrat.*delgV);
Ltg(1)=ngrat(1)*delgV(1);
% generate vector of indices based on input index function
```

```
zn(1)=ngrat(1)*2;
% generate vector of coordinates
Z(1:zn(1))=0:delgV(1)/2:Ltg(1)-delgV(1)/2;
delzV(1:zn(1))=delgV(1)/2;
ZL=length(Z);
Zmax=Z(ZL);
Zmid=Zmax/2;
ZQ=1:1:ZL;
%calculate the background effective index of ↙
the structure no
dGaAs=lambdaE/(4*nGaAs);
dAlAs=lambdaE/(4*nAlAs);
c1=dGaAs/delgV;
c2=dAlAs/delgV;
n0=(c1*nGaAs)+(c2*nAlAs);
% This file assumes a square grating profile.
ngb=n0;
nz(1:zn(1))=ngb-exp(((Z(1:zn(1))-Zmid)./Zmax)↙
.^2).*(dngV(1)/2).*(-1).^ZQ(1:zn(1));
Nz=nz;
% This part of the file performs the transfer↙
-matrix calculation on the structure n(z) at ↙
each wavelength of interest.
% create for-loop to run simulation at each p↙
oint in vector of wavelengths
Q=length(k0);
%tstart=clock;
for q=1:Q
% calculate transfer matrix for the last laye↙
r and interface
QZ=length(Z);
mgrating=[exp(i*k0(q)*Nz(QZ)*delzV(QZ)) 0; 0 ↙
exp(-i*k0(q)*Nz(QZ)*delzV(QZ))]*(1/(2*Nz(QZ))↙
)*[Nz(QZ)+n0 Nz(QZ)-n0; Nz(QZ)-n0 Nz(QZ)+n0];
mp11(QZ)=mgrating(1,1);
mp21(QZ)=mgrating(2,1);
```

```
% calculate transfer matrix for DBR structure
for qz=QZ-1:-1:2
mgrating=[exp(i*k0(q)*Nz(qz)*delzV(qz)) 0; 0 ↙
exp(-i*k0(q)*Nz(qz)*delzV(qz))]*(1/(2*Nz(qz))↙
)*[Nz(qz)+Nz(qz+1) Nz(qz)-Nz(qz+1); Nz(qz)-Nz↙
(qz+1) Nz(qz)+Nz(qz+1)]*mgrating;
mp11(qz)=mgrating(1,1);
mp21(qz)=mgrating(2,1);
end
% calculate transfer matrix for the first int↙
erface and layer and interface
mgrating=(1/(2*n0))*[n0+Nz(1) n0-Nz(1); n0-Nz↙
(1) n0+Nz(1)]*[exp(i*k0(q)*Nz(1)*delzV(1)) 0;↙
 0 exp(-i*k0(q)*Nz(1)*delzV(1))]*(1/(2*Nz(1))↙
)*[Nz(1)+Nz(2) Nz(1)-Nz(2); Nz(1)-Nz(2) Nz(1)↙
+Nz(2)]*mgrating;
mp11(1)=mgrating(1,1);
mp21(1)=mgrating(2,1);
% calculate the overall amplitude reflection
r(q)=mgrating(2,1)/mgrating(1,1);
% calculate the power reflectivity
R(q)=r(q)*conj(r(q));
end

plot(lambda,R)
```

Appendix C

QD-SAM Operation Fluence - sample calculation

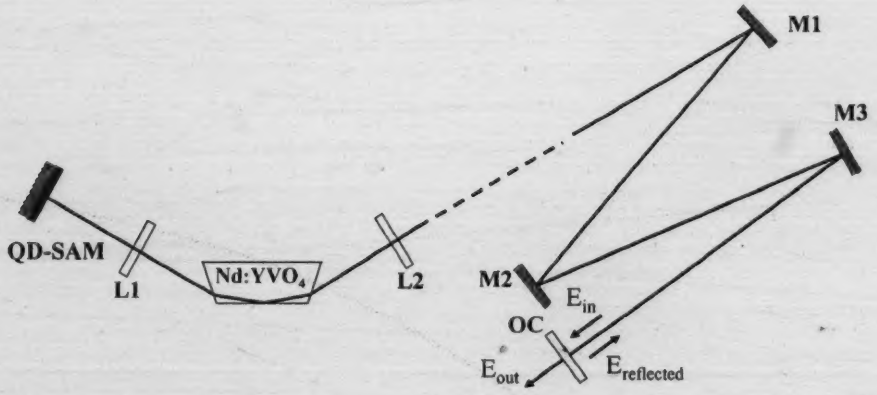

Figure 38: Schematic diagram of the laser setup used to calculate the laser operation fluence on the QD-SAM

We need to calculate the fluence incident on the QD-SAM device during mode-locked laser operation. For this example we will analyze the case of our laser system when mode-locked using the QD-SAM (see figure 38).

We know the output average power of the laser $P_{avg-out} = 7.1$ W, the repetition rate $rep.rate = 65$ MHz, the QD-SAM reflectivity value $R_{QD-SAM} = 72\%$ at the laser operation wavelength (see figure 28 (b)), the OC value (for this case $T_{OC} = 53\%$ transmission), and the reflectivities of all the cavity mirrors (M1, M2, M3 mirrors). The mirrors M1, M2, M3 are high reflectivity

(> 99%) commercial dielectric mirrors, and their loss will be neglected in these calculations. We also know the spot size on the QD-SAM as being an ellipse with the horizontal diameter $d_h = 671\mu m$ FWHM and the vertical diameter $d_v = 749\mu m$ FWHM, giving the area $S = 3.947 \cdot 10^{-3}$ cm^2.

The output energy E_{out} is:

$$E_{out} = \frac{P_{avg-out}}{rep.rate} = 109.23nJ/pulse, \tag{28}$$

and represents 53% of the incident energy on the OC. Therefore the incident energy is $E_{in} = 206nJ/pulse$. The portion of the incident energy that is reflected back in the resonator represents 47% of E_{in} and it was calculated to be $E_{reflected} = 96.9nJ/pulse$.

The net reflectivity of the laser resonator represents the product of all the reflectivities,

$$R_{net} = R_{QD-SAM} \times (1 - T_{OC}) = 0.338 \tag{29}$$

The net gain of the laser per round trip is $A_{round-trip} = 1/R_{net} = 2.955$, and the net gain per single pass through the $Nd : YVO_4$ crystal is $A_{single-pass} = 1.719$

Finally, the fluence on the QD-SAM is given by

$$F_{QD-SAM} = \frac{A_{single-pass} \times E_{reflected}}{S} \simeq 42\mu J/cm^2. \tag{30}$$